



HAL
open science

OPTO-MECHA-SPIM: Dynamic and interactive imaging of mechanobiological phenomena in tissues

Javier Morgado Brajones

► **To cite this version:**

Javier Morgado Brajones. OPTO-MECHA-SPIM: Dynamic and interactive imaging of mechanobiological phenomena in tissues. Bioinformatics [q-bio.QM]. Université Paul Sabatier - Toulouse III, 2019. English. NNT: 2019TOU30252 . tel-02965916

HAL Id: tel-02965916

<https://theses.hal.science/tel-02965916>

Submitted on 13 Oct 2020

HAL is a multi-disciplinary open access archive for the deposit and dissemination of scientific research documents, whether they are published or not. The documents may come from teaching and research institutions in France or abroad, or from public or private research centers.

L'archive ouverte pluridisciplinaire **HAL**, est destinée au dépôt et à la diffusion de documents scientifiques de niveau recherche, publiés ou non, émanant des établissements d'enseignement et de recherche français ou étrangers, des laboratoires publics ou privés.



THÈSE

En vue de l'obtention du **DOCTORAT DE L'UNIVERSITÉ DE TOULOUSE**

Délivré par l'Université Toulouse 3 - Paul Sabatier

Présentée et soutenue par
Javier MORGADO BRAJONES

Le 9 décembre 2019

**OPTO-MECA-SPIM: Imagerie dynamique et interactive de
phénomènes mécanobiologiques dans les tissus**

Ecole doctorale : **BSB - Biologie, Santé, Biotechnologies**

Spécialité : **BIO-INFORMATIQUE, GENOMIQUE ET BIOLOGIE DES SYSTEMES**

Unité de recherche :

ITAV - Institut des Technologies Avancées en sciences du Vivant

Thèse dirigée par

Corinne LORENZO et Christophe COUDRET

Jury

Mme Alexandra Fragola, Rapporteur

M. David Rousseau, Rapporteur

Mme Kerstin Bystricky, Examinatrice

M. Rémi Galland, Examineur

Mme Corinne LORENZO, Directrice de thèse

M. Christophe Coudret, Co-directeur de thèse

Abstract

In recent years, tissue mimics (TMs) such as microtissues, spheroids, and organoid cultures have become increasingly important in life-science research, as they provide a physiologically relevant environment for cell growth, tissue morphogenesis, and stem cell differentiation. Selective Plane Illumination Microscopy (SPIM) is one of the most prominent microscopy modalities for three-dimensional tissue imaging, and a sine qua non tool to understand cell biology in TMs. However, while SPIM is regarded as a very powerful tool for TM imaging, optical microscopy suffers from certain limitations when imaging 3D samples. Indeed, scattering, absorption and optical aberrations limit the depth at which useful imaging can be done, typically no more than 100 μm . Adaptive Optics (AO) is a technique capable of improving image quality at depth by correcting the optical aberrations introduced by the sample which is seeing increasing use in fluorescence microscopes.

For this thesis, I have incorporated a wavefront sensor AO scheme to SPIM, able to correct aberrations in optically thick TMs such as multi-cellular tumor spheroids (MCTS). Due to the low amount of light produced by non-linear guide stars such as the one used in our system, a custom high-sensitivity Shack-Hartmann wavefront sensor (SHWFS) was developed for our needs. In this work, I characterize the performance of this SHWFS and the ability of our system to correct aberration in various conditions, including inside TMs.

I show unprecedented image quality improvements for in-depth imaging of MCTS, in regard of high-frequency detail and resolution. This allowed us to identify biologically relevant features at depths inaccessible to conventional SPIM.

Up-converting nanoparticles (UCNP) are rare-earth based particles that are able to undergo photon up-conversion when illuminated, emitting light of a shorter wavelength than that of the illumination. Guide stars made from UCNP are especially attractive due to the possibility of them being excited in the near-infrared while emitting visible light, reducing photodamage produced by the illumination light. The viability of using UCNP as guide stars in biological samples is explored in this thesis.

Résumé

Les modèles en 3D occupent une place de plus en plus importante en biologie cellulaire car ils offrent de nombreux avantages pour la compréhension des processus physiopathologiques. La microscopie à feuille de lumière et plus particulièrement, le Selective Plane Illumination Microscope (SPIM), un de ses variants, représente un outil de choix pour observer et imager avec une haute résolution spatio-temporelle ces structures assimilées à des tissus (TM). Bien que le SPIM est un outil puissant, il souffre de phénomènes tels que la diffusion, l'absorption et les aberrations optiques qui limitent la profondeur à laquelle une imagerie utile peut être réalisée. L'optique adaptative (AO), de plus en plus utilisée dans le domaine de la microscopie, est une technique capable d'améliorer la qualité d'imagerie en profondeur en corrigeant les aberrations optiques introduites par l'échantillon.

Pour ce travail de thèse, j'ai implémenté dans un SPIM un système d'AO capable de corriger les aberrations dans les TMs optiquement épais tels que les sphéroïdes tumoraux multicellulaires (MCTS). Un capteur de front d'onde de type Shack-Hartmann (SHWFS) à haute sensibilité a été développé à façon afin de permettre la reconstruction du front d'onde à partir de la faible quantité de lumière produite par l'étoile guide non linéaire utilisé dans notre système. Au cours de ce travail, j'ai tout d'abord caractérisé les performances de ce SHWFS et évalué la capacité du système à corriger les aberrations dans diverses conditions, y compris à l'intérieur de TMs.

J'ai observé des améliorations sans précédent de la qualité d'image en profondeur des MCTS, en termes de détails et de résolution haute-fréquence. Grâce à ces corrections, j'ai pu mettre en évidence des événements biologiques tels que des mitoses non visibles sans corrections.

Les « up converting » nanoparticules (UCNP) sont des particules de terres rares capables d'émettre une lumière d'une longueur d'onde plus courte que celle de l'éclairage lorsqu'elles sont illuminées. Les étoiles guides en UCNP sont particulièrement intéressantes en raison de la possibilité qu'elles soient excitées dans l'infrarouge proche tout en émettant de la lumière visible, ce qui réduit le photodommage produit par l'éclairage. La possibilité d'utiliser des UCNP comme étoiles guides dans des échantillons biologiques a été explorée dans cette thèse.

Acknowledgements

First and foremost, I would like to thank my thesis supervisor, Corinne Lorenzo, for her guidance and support through these three years. Were it not for her, this thesis would have certainly not been possible. Many thanks also to my co-supervisor, Christophe Coudret, as well as the whole IDeAS team, who, even though my visits to the enigmatic world of chemistry were few and sparse, made me feel right at home.

I would like to also thank the former members of our team, especially Martine Cazales and Théo Liu, whose assistance during the early stages of my stay was invaluable. I wish you the best in your new adventures.

Special thanks to my dear friend Rosa Guadalupe López Reyes, faithful drinking partner with whom I have complained about the hardships of the life a PhD student more times than I can count.

Finally, there are no words to express my gratitude to my parents, Francisco Javier and María José, and my sister Paula, who have put up with me being away during a long and hard time without so much as a word of objection. *Esta tesis está dedicada a vosotros.*

Contents

Abstract	i
Acknowledgements	iii
1. Introduction	1
2. Background and State of the Art	5
2.1. Principles of Image Formation	5
2.1.1. Nature of light	6
2.1.2. Kirchhoff's diffraction theory	7
2.1.3. Imaging with aberrations	9
2.1.4. The Maréchal approximation	11
2.1.5. Modal representation of the wavefront	13
2.2. Tissue mimics	16
2.2.1. Optical properties of tissue mimics	17
2.2.2. Multi-Cellular Tumor Spheroids	20
2.3. Light sheet Fluorescence Microscopy	24
2.3.1. Tissue mimics and microscopy	24
2.3.2. Basics of LSFM	25
2.3.3. Resolution and speed in LSFM	27
2.3.4. The light sheet	31
2.3.5. Illumination modalities	34
2.3.6. The penetration problem	38
2.4. Adaptive Optics	40
2.4.1. Introduction	40
2.4.2. Wavefront sensing	43
2.4.3. Wavefront correction	54

3. System Implementation and Characterization.....	61
3.1. Introduction	61
3.2. Description of the system.....	62
3.2.1. General view	62
3.2.2. The non-linear guide star.....	67
3.2.3. High-sensitivity Shack-Hartmann wavefront sensor	70
3.3. System set-up.....	74
3.4. Adaptive optics performance.....	76
3.4.1. Methods	76
3.4.2. Performance results.....	78
3.5. Conclusion.....	82
4. Multi-cellular Tumor Spheroid Imaging	83
4.1. Introduction	83
4.2. Methods	84
4.3. Results.....	85
4.4. Discussion.....	92
5. Up-Converting Nanoparticles as Guide Stars	95
5.1. Introduction	95
5.2. Methods	97
5.3. Results.....	98
5.3.1. Toxicity	98
5.3.2. Distribution inside MCTS.....	100
5.4. Discussion.....	102
6. Conclusion	105
References.....	111
Appendix 1: Detailed list of the optical elements of $w_{AO}SPIM$	123

Appendix 2: *Methods and Protocols* publication125

Figures

Figure 2-1: Wave propagating through an aperture.....	8
Figure 2-2: Aberrated wavefront propagating through an aperture.	9
Figure 2-4: Spatial shape of the first 28 Zernike polynomials.	14
Figure 2-5: Beam propagating through a TM.	18
Figure 2-6: Structure of an MCTS.....	21
Figure 2-7: SPIM setup.....	26
Figure 2-8: Detail of the RLSM illumination scheme.....	28
Figure 2-9: OPM setup.	29
Figure 2-10: APOM microscope.....	30
Figure 2-11: Main properties of a light sheet.	33
Figure 2-12: Stripe artifact created by the blocking of the light by an obstacle.	34
Figure 2-13: Self-healing nature of a Bessel beam.....	36
Figure 2-14: Properties of Gaussian and Bessel beams, and square and hexagonal lattices..	37
Figure 2-15: Working of a SHWFS.....	45
Figure 2-16: Comparison between detected and actual intensity distribution over a sensor.....	46
Figure 2-17: Calculation of wavefront slope over a subaperture from the displacement of the displacement of the Shack-Hartmann spot.	49
Figure 2-18: Comparison between Hudgin and Fried geometries.	50
Figure 2-19: Wavefront correction by phase conjugation.....	55
Figure 2-20: Example of open and closed loop configurations.....	56
Figure 2-21: Electrostatic deformable mirror.	58
Figure 2-22: Electromagnetic deformable mirror.....	59
Figure 2-23: Bimorph piezoelectric wafer deformable mirror.	60

Figure 3-1: Schematic image of $w_{AO}SPIM$.	63
Figure 3-2: Detail of the illumination path.	64
Figure 3-3: Detail of the two-photon excitation arm.	65
Figure 3-4: Detail of the detection path.	66
Figure 3-5: Mounting scheme of our system.	67
Figure 3-6: Guide star observed at different depths within an MCTS.	68
Figure 3-7: NGS observed maximum intensity as a function of depth inside an MCTS.	69
Figure 3-8: Simulated wavefront error as a function of the total number of photons reaching the SHWFS.	71
Figure 3-9: Simulated dynamic range of wavefront reconstruction.	72
Figure 3-10: Alternative position of the SHWFS used for the correction of system-induced aberrations.	74
Figure 3-11: Wavefronts measured at the two different SHWFS positions with the mirror in the “AO off” shape.	75
Figure 3-12: Schematic of the experiment for the determination of AO performance	77
Figure 3-13: Maximum intensity projection and wavefront of green fluorescent beads imaged through a capillary glass before and after AO correction	79
Figure 3-14: RMS and Strehl ratio values of wavefronts before and after AO correction as a function of photon flux and number of closed loop iterations	81
Figure 4-1: Maximum intensity projection of an MCTS expressing H2B-GFP before and after correction at different depths.	86
Figure 4-2: Measured wavefronts after AO corrections of an MCTS at different depths.	87
Figure 4-3: Maximum intensity projection of an HCT116 nucleus expressing H2B-GFP before and after AO correction at different depths	88

Figure 4-4: Maximum intensity projections of an MCTS expressing the fluorescent histone ArrestRed before and after AO corrections were performed at different depths	89
Figure 4-5: Maximum intensity projection of three regions of an MCTS before and after AO correction.....	90
Figure 4-6: Quantitative analysis of AO correction in MCTS.....	91
Figure 5-1: CR3936-69P1 up-conversion spectrum.....	97
Figure 5-2: Widefield image of MCTS after 4 days of growth in presence of different concentrations of CR3936-69P1.	99
Figure 5-3: Three-dimensional distribution of nanoparticles on MCTS as seen from different angles over the Y axis.	101
Figure 5-4: Effect of BSA on the three-dimensional distribution of nanoparticles on an MCTS.....	102

Tables

Table 1: Scattering coefficients for healthy tissue, tumoral tissue and MCTS for visible and near-infrared wavelengths.	23
Table 2: Waist thickness and Rayleigh range of the light sheet for all the possible illumination modes of the system.....	65
Table 3: Observed lateral FWHM of the NGS at different depths inside an MCTS.....	69
Table 4: Specifications of our Shack-Hartmann wavefront sensor for a 555 nm guide star.....	73
Table 5: Mean full width at half maximum, RMS aberration and Strehl ratio values for beads imaged through a glass capillary before and after correction.....	79
Table 6: Mean correction results for images of beads through a glass capillary for different emission intensities.....	80
Table 7: RMS aberration before and after AO correction at different depths.....	87
Table 8: Size of MCTS grown in the presence of CR3936-69P1 after 4 days.....	100
Table 9: Size of MCTS grown in the presence of CR3936-69P1 after 8 days.....	100

Chapter 1

INTRODUCTION

Fluorescence microscopy is one of the most powerful and versatile tools for the observation and quantification of biological processes in a wide range of spatial and temporal scales: from single molecules to whole organisms, from microseconds to weeks. Its wide range of applications, combined with the ease of use of most instruments, has made fluorescence microscopes ubiquitous across biology laboratories.

The widefield fluorescence microscope is perhaps the most common of such instruments. While it is enormously valuable for imaging of thin samples such as monolayered cultures or thin slices of tissue, most three-dimensional information about the sample is lost due to its lack of optical sectioning.

This inability to extract three-dimensional information from living samples has for a long time relegated the study of biological phenomena to their observation in monolayered cells cultures. Two-dimensional cultures allow the study of many

biological processes, but they do not fully take into account the effects of the three-dimensional organization of cells and extracellular matrix within tissues.

During the last decades, three-dimensional model systems of a large number of human organs and tissues have been developed to allow the study of processes sensitive to the three-dimensional structure of the tissue, such as organogenesis or disease spread. These tissue mimics provide a more physiologically relevant microenvironment for the study of tissue and organ development, presenting similar differentiation patterns as their in-vivo counterpart as well as a similar 3D network of cell-cell and cell-matrix interactions.

Still, adequate optical instruments are required to visualize three-dimensional processes in tissue mimics. Over the last decade, light sheet fluorescence microscopy (LSFM) has established itself as the tool of choice for three-dimensional imaging of tissue mimics. In the simplest LSFM variant, the selective plane illumination microscope (SPIM), a thin plane of the sample is illuminated by means of a light sheet placed in the focal plane of the detection objective. This way, three-dimensional imaging of the sample is possible by simply moving it through the light sheet. Since only a single plane is illuminated and all the emitted light is collected, photodamage and photobleaching are kept to a minimum, whereas acquisition frequency can be as high as tens of volumes per second.

However, in-depth imaging of biological tissue is limited by absorption, scattering and optical aberrations arising from the interaction of light and the sample. These issues typically limit the maximum depth of subcellular-resolution imaging of tissue mimics to no more than a few dozen microns. Traditional methods aiming to improve in-depth imaging of such optically thick samples, such as sample clearing, are typically focused on changing the optical properties of the sample, which often involves the killing of the specimen and therefore have limited convenience for in-vivo studies.

Adaptive optics (AO) is a technique, first developed for astronomy, able to correct the aberrations induced by the sample and the optical system by modulating the wavefront of the acquired optical signal. In recent years, AO has seen increased use in different microscopy modalities. AO is a natural fit for LSFM, as it can substantially increase the maximum useful imaging depth, while providing improved resolution and contrast. Still, the use of AO in optically thick samples remains challenging, due to the low signal-to-noise ratio caused by the limited amount of ballistic light and the high background noise produced by scattered photons.

This thesis is concerned with the improvement of three-dimensional imaging of TMs. For this, I have implemented an adaptive SPIM, able to correct the aberrations produced by both the sample and the optical system. I have fully characterized the microscope and the performance of the AO system, and demonstrated its use on TM imaging. Finally, I have explored the possibility of using up-converting nanoparticles, capable of producing anti-Stokes emission, as guide stars for AO correction.

Synopsis

The thesis is structured as follows:

- Chapter 2 presents the theoretical background behind tissue mimic imaging and adaptive optics, as well as the state-of-the-art of relevant topics. It starts with the fundamentals of image formation and the theoretical treatment of aberrations, followed by an introduction to tissue mimics and their optical properties. Next, I provide the basics of LSFM and its use on TMs. The last section offers a detailed explanation of adaptive optics, as well as the state-of-the-art of its use on microscopy.
- Chapter 3 refers to the implementation and characterization of our adaptive SPIM. A detailed description of the different subsystems and their

implementation is provided. The performance of the AO corrections is determined, with focus on low photon flux conditions.

- Chapter 4 is devoted to TM imaging. Using multi-cellular tumor spheroids, I show improvements in image quality after AO correction. A detailed analysis of these improvements is provided.
- Chapter 5 discusses the use of up-converting nanoparticles (UCNP) as guide stars in TMs. First, I study the toxicity of UCNP and their effects in TM development. Then, the viability of UCNP for wavefront measurement is determined.
- Chapter 6 presents the conclusions of this thesis, as well as the perspectives for our research.

Chapter 2

THEORETICAL BACKGROUND AND STATE OF THE ART

2.1. Principles of Image Formation

The optical imaging of thick tissue presents some unavoidable problems that arise from their inhomogeneity. Absorption, scattering and aberrations severely limit the maximum depth at which useful imaging can be performed. In order to understand how these issues affect imaging, a basic knowledge of the theory behind light propagation is required.

This chapter briefly presents the theoretical basis that governs image formation, as well as the mathematical tools that allow us to describe optical aberrations and system performance.

2.1.1. Nature of light

It is universally accepted that light behaves both as a particle, the photon, and as a wave. Since light is an electromagnetic wave, its behaviour can be directly derived from Maxwell's equations [1]. The value of the electromagnetic field U at any point \mathbf{r} may be represented as:

$$U(\mathbf{r}) = Ae^{i(kr-\omega t)}, \quad (2-1)$$

where A is the amplitude of the wave, k is its wave number, and ω is its angular frequency. k and ω are related to the wavelength λ and frequency ν as follows:

$$k = \frac{2\pi}{\lambda}, \quad \omega = 2\pi\nu.$$

In addition, the speed of light in vacuum c is given by

$$c = \lambda\nu, \quad (2-2)$$

and takes value $c = 2.998 \times 10^8 \text{ m/s}$. The refractive index n is the ratio between c and the speed of light in a medium v :

$$n = \frac{c}{v}. \quad (2-3)$$

The term

$$\Phi = kr - \omega t \quad (2-4)$$

is the phase of the wave. A surface of constant phase is called a wavefront. The waves in which the wavefront takes the form of a sphere (such as those produced by a point emitter) are said to be spherical, and can be approximated to a plane wave after a long enough propagation.

When light forms an image, the magnitude of the signal is directly correlated to the intensity (power per unit area) of the electromagnetic wave at that point. The

intensity or irradiance I of a monochromatic wave propagating through a non-magnetic medium is given by:

$$I = \frac{cn\varepsilon_0}{2} |U(\mathbf{r})|^2, \quad (2-5)$$

where ε_0 is the vacuum permittivity. In calculations, the term $cn\varepsilon_0/2$ is usually omitted for simplicity.

2.1.2. Kirchhoff's diffraction theory

Image formation cannot be considered without taking into account the diffracting nature of the light. One of the firsts attempts to explain the propagation of light as a wave was made by Christiaan Huygens. According to Huygens, every element of the wavefront acts as the centre of secondary disturbances that give way to spherical wavelets, in such a way that the wavefront at a later time is the envelope of those secondary wavelets [2]. This principle, commonly referred as Huygens' construction, can explain propagation, refraction and reflection of light. However, diffraction phenomena cannot be adequately explained by it.

Fresnel later complemented Huygens' construction with the introduction of mutual interference between the secondary wavelets. This interference accounts for Huygens' postulate that the secondary wavelets only travel forward and can adequately explain diffraction. This combination of Huygens' construction with Fresnel's ideas of interference receives the name of the Huygens-Fresnel principle, and is the foundation of physical optics.

A sound mathematical basis for this principle would have to wait for half a decade. From the wave equation and Green's second identity, Kirchhoff's derived the Fresnel-Kirchhoff integral theorem, of which the Huygens-Fresnel principle is a particular case.

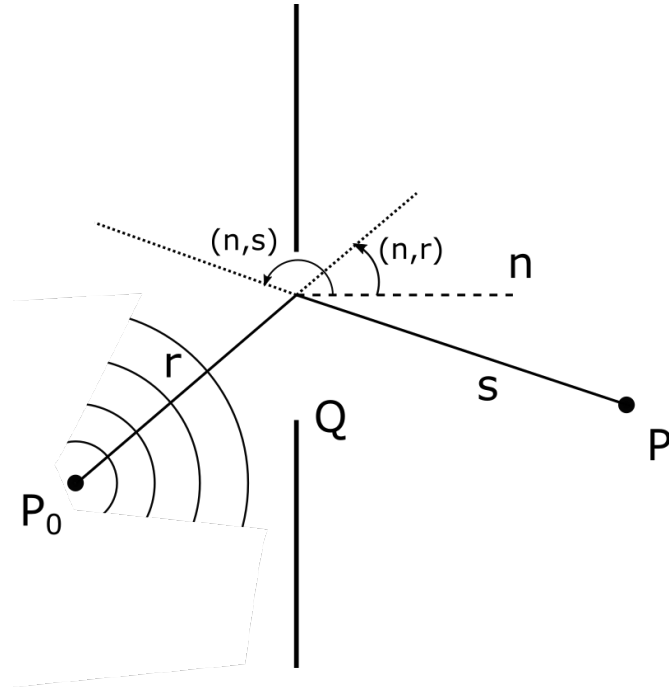


Figure 2-1: Wave propagating through an aperture.

Let us consider a monochromatic wave originating from a point source P_0 propagating through an aperture in a plane screen, and let P be the point at which the electromagnetic field is to be evaluated. The main result of the Fresnel-Kirchhoff integral theorem states that:

$$U(P) = -\frac{iA}{2\lambda} \iint_Q \frac{e^{ik(r+s)}}{rs} [\cos(n, r) - \cos(n, s)] dS, \quad (2-6)$$

where Q is the aperture, r and s are, respectively, the distances from P_0 and P to a surface element the aperture, and (n, r) and (n, s) are the angles of r and s with the normal of the surface.

If P sufficiently far away, the distance to the aperture can be approximated as a constant $r \approx r_0$, and the previous expression can be simplified as:

$$U(P) = -\frac{i}{2\lambda} \frac{Ae^{ikr_0}}{r_0} \iint_Q \frac{e^{iks}}{s} (1 + \cos \chi) dS, \quad (2-7)$$

where $\chi = \pi - (r_0, s)$.

2.1.3. Imaging with aberrations

Let us consider a rotationally symmetrical optical system with a point source of monochromatic light at P_0 , and let us assume that P_0 forms an image at P_1^* . We can take a cartesian system of axes, with origin at P_1^* , z-axis along CP_1^* , where C is the centre of the exit pupil, and y-axis along the meridional plane. Let W be any wavefront that goes through C , and let Q and Q' be the points in which a given ray intersects the gaussian reference sphere and the wavefront W , respectively. The aberration function $\Phi(Q)$ represents the optical distance along the ray between the points Q and Q' and we define it positive as shown in Figure 2-2.

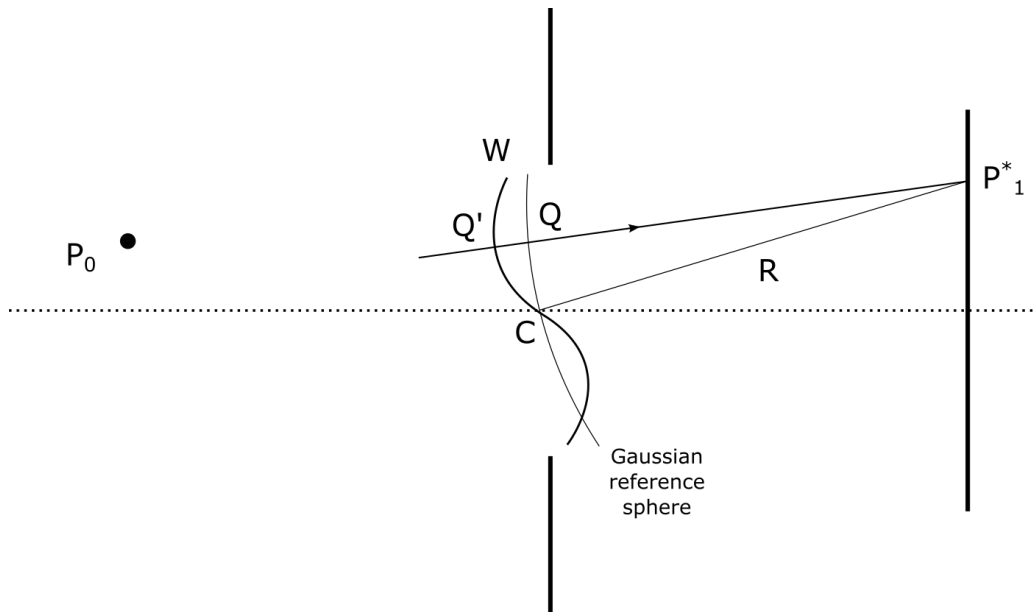


Figure 2-2: Aberrated wavefront propagating through an aperture.

Let s be the distance between Q and an arbitrary point P , and let R be the radius of the gaussian reference sphere. According to (2-7) and assuming small angles ($\cos \chi \approx 1$):

$$U(P) = -\frac{i A e^{-ikR}}{\lambda R} \iint_{\mathcal{C}} \frac{e^{ik(\Phi+s)}}{s} dS, \quad (2-8)$$

where \mathcal{C} is the region of the reference sphere that approximately fills the exit pupil. In polar coordinates, this equation becomes:

$$U(P) = -\frac{i A a^2}{\lambda R^2} e^{i\left(\frac{R}{a}\right)^2 u} \int_0^1 \int_0^{2\pi} e^{i[k\Phi - vp \cos(\theta-\varphi) - \frac{1}{2}u\rho^2]} \rho d\rho d\theta, \quad (2-9)$$

where the circular pupil has radius a and polar coordinates ρ and θ , the image plane has polar coordinates r and φ , and

$$u = \frac{2\pi}{\lambda} \left(\frac{a}{R}\right)^2 z, \quad v = \frac{2\pi}{\lambda} \left(\frac{a}{R}\right) \sqrt{x^2 + y^2} \quad (2-10)$$

are normalized coordinates in the focal plane. According to (2-5) and ignoring the constant factor, the intensity at P is:

$$I(P) = |U(P)|^2 = \left(\frac{Aa^2}{\lambda R^2}\right)^2 \left| \int_0^1 \int_0^{2\pi} e^{i[k\Phi - vp \cos(\theta-\varphi) - \frac{1}{2}u\rho^2]} \rho d\rho d\theta \right|^2. \quad (2-11)$$

If no aberrations are present, the intensity is then a maximum at the Gaussian image point (P_1^* ; $r = 0$):

$$I^* = I_{\Phi=0}(P_1^*) = \pi^2 \left(\frac{Aa^2}{\lambda R^2}\right)^2. \quad (2-12)$$

The ratio between the intensity at the Gaussian image point of an aberrated and an unaberrated beam is called the Strehl Ratio (SR):

$$SR = \frac{I(P_1^*)}{I^*} = \frac{1}{\pi^2} \left| \int_0^1 \int_0^{2\pi} e^{i[k\Phi - vp \cos(\theta-\varphi) - \frac{1}{2}u\rho^2]} \rho d\rho d\theta \right|^2. \quad (2-13)$$

Let Φ' be a wavefront defined as:

$$\Phi' = \Phi + c_3\rho^2 + c_2\rho \cos \theta + c_1\rho \sin \theta + c_0,$$

where c_0, \dots, c_3 are constants. It can be shown (ref) that there exists a point P where:

$$SR = \frac{I(P_1^*)}{I^*} = \frac{I(P)}{I^*}. \quad (2-14)$$

That is, the addition of an aberration in the form $c_3\rho^2 + c_2\rho \cos \theta + c_1\rho \sin \theta + c_0$ does not change the three-dimensional intensity distribution near focus, but causes the displacement of the distribution as a whole. This is equivalent to a shift of the Gaussian image point, i.e. by displacing our reference point, we can remove the quadratic and linear terms of the aberration. It will later be shown that an aberration of this form is a linear combination of piston, tilt and defocus aberrations. Therefore, no intensity improvements can be obtained from correcting these modes of aberration. If the remaining aberrations at the new Gaussian image point are represented by Φ_p , the Strehl Ratio can be written as:

$$SR = \frac{1}{\pi^2} \left| \int_0^1 \int_0^{2\pi} e^{ik\Phi_p} \rho d\rho d\theta \right|^2. \quad (2-15)$$

This important result shows how aberrations affect the degradation of the propagation. If the beam is unaberrated, $\Phi_p = 0$ and $SR = 1$, and thus the intensity at focus will be diffraction limited. In the presence of any aberration at all, $\Phi_p > 0$ and the Strehl Ratio will be less than unity [1], [3].

2.1.4. The Maréchal approximation

When the aberrations are small, it is possible to express the intensity in terms of the mean square value of the beam aberration. Let Φ_p be the aberration referred to a reference sphere centred on a point P in the image region. The exponential function in (2-15) can be expanded as a Taylor series:

$$SR = \frac{1}{\pi^2} \left| \int_0^1 \int_0^{2\pi} e^{ik\Phi_p} \rho d\rho d\theta \right|^2 = \frac{1}{\pi^2} \left| \int_0^1 \int_0^{2\pi} (1 + ik\Phi_p + \frac{1}{2}(ik\Phi_p)^2 + \dots) \rho d\rho d\theta \right|^2. \quad (2-16)$$

Let \bar{x} denote the average value of any variable x over the pupil:

$$\bar{x} = \frac{\int_0^1 \int_0^{2\pi} x \rho d\rho d\theta}{\int_0^1 \int_0^{2\pi} \rho d\rho d\theta} = \frac{1}{\pi} \int_0^1 \int_0^{2\pi} x \rho d\rho d\theta. \quad (2-17)$$

If we assume that the aberrations are small, we can truncate the Taylor series expansion at the second order term. Using identity (2-17) in the truncated series:

$$SR \approx \left| 1 + ik\bar{\Phi}_p - \frac{1}{2}k^2\bar{\Phi}_p^2 \right|^2 = 1 - \left(\frac{2\pi}{\lambda} \right)^2 \left[\bar{\Phi}_p^2 - (\bar{\Phi}_p)^2 \right]. \quad (2-18)$$

The term in brackets corresponds to the variance of the wavefront:

$$(\Delta\Phi_p)^2 = \frac{\int_0^1 \int_0^{2\pi} (\Phi_p - \bar{\Phi}_p)^2 \rho d\rho d\theta}{\int_0^1 \int_0^{2\pi} \rho d\rho d\theta} = \bar{\Phi}_p^2 - (\bar{\Phi}_p)^2, \quad (2-19)$$

and, thus, we can express the Strehl Ratio as:

$$SR \approx 1 - \left(\frac{2\pi}{\lambda} \right)^2 (\Delta\Phi_p)^2 \approx e^{-\left(\frac{2\pi}{\lambda} \right)^2 (\Delta\Phi_p)^2} \quad (2-20)$$

This formula was first derived by Maréchal and provides a simple but powerful method of evaluating the quality of the beam for small aberrations by taking into account only the variance of the wavefront. The standard deviation of the wavefront $\Delta\Phi_p$ is often called the root mean square (RMS) wavefront error, phase error or simply wavefront error and it is usually the main magnitude to be evaluated when assessing the quality of an aberrated instrument.

The Maréchal criterion establishes that an image is diffraction-limited when $\Delta\Phi_p < \lambda/14$, which roughly corresponds to $SR > 0.8$. This is one of the most

commonly used performance criteria, and will be the one employed throughout this thesis.

2.1.5. Modal representation of the wavefront

The function Φ has been historically represented in many different ways. Of special importance are the representations as a complete set of orthogonal polynomials over the unit circle. These representations are denominated modal representations, of which the most prominent representatives are the Zernike and Lukosz polynomials. Since most contemporary works employ Zernike polynomials, the explanation about the Lukosz representation will be omitted.

2.1.5.1. The Zernike polynomials

This set of polynomials was first introduced by Frits Zernike in 1934¹ [4]. They are polynomials in two variables that are usually expressed in polar coordinates. In their real form they are defined as [6]:

$$\begin{cases} Z_n^l(\rho, \theta) = \sqrt{2(n+1)}R_n^l \cos l\theta & m \neq 0 \\ Z_n^{-l}(\rho, \theta) = \sqrt{2(n+1)}R_n^l \sin l\theta & m \neq 0 \\ Z_n^0(\rho, \theta) = \sqrt{n+1}R_n^0 & m = 0 \end{cases} \quad (2-21)$$

where $n \geq l$, $n - l = \text{even}$, and n and l are non-negative integers. Let $l = |m|$, the radial polynomials R_n^m are defined as:

$$R_n^m(\rho) = \sum_{s=0}^{\frac{n-|m|}{2}} (-1)^s \frac{(n-s)!}{s! \left(\frac{n+|m|}{2} - s\right)! \left(\frac{n+|m|}{2} - 2\right)!} \rho^{n-2s}, \quad (2-22)$$

and they are normalized so that for all n and m :

¹ The derivation of the Zernike polynomials involves a lengthy and rather abstract departure into the world of group theory, and it is not considered of interest for this dissertation. The original derivation can be found in [4] (in German), while an alternative approach can be found in [5].

$$R_n^m(1) = 1. \quad (2-23)$$

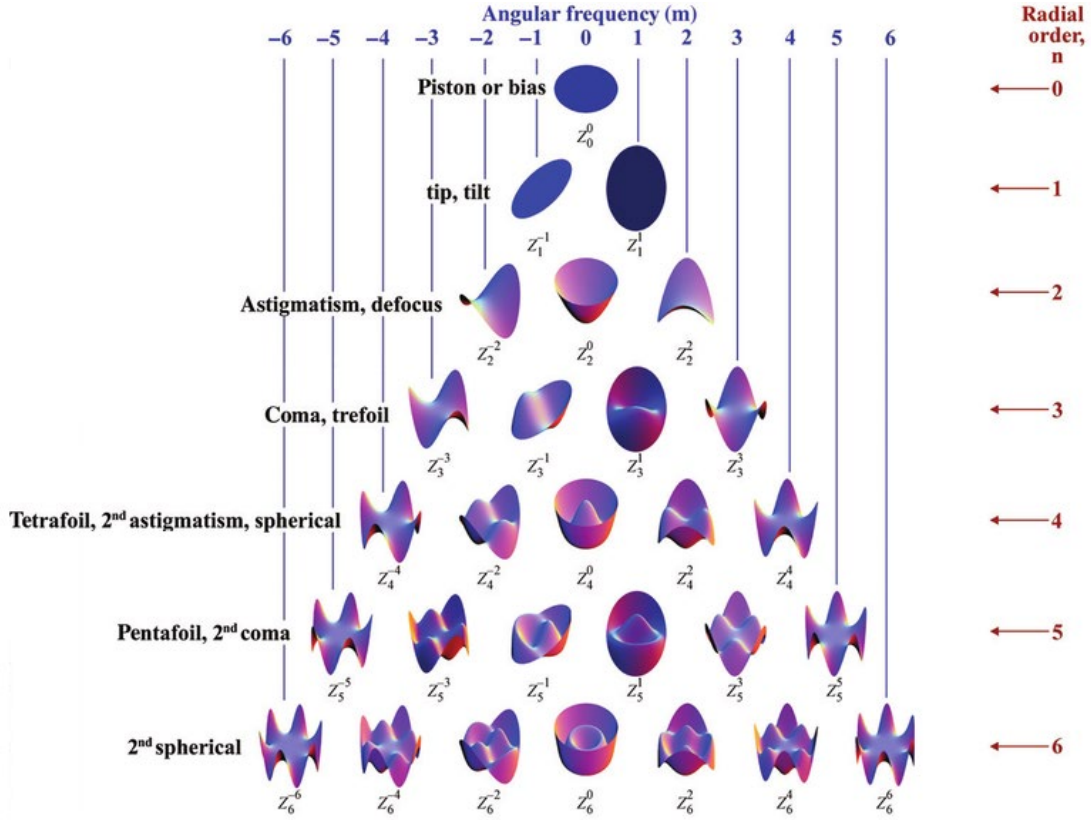


Figure 2-3: Spatial shape of the first 28 Zernike polynomials. Modified from [7].

The polynomials $Z_n^m(\rho, \theta)$ are said to be even when $m \geq 0$ and odd when $m < 0$. The Zernike polynomials form an orthonormal basis over the unit circle [7], i.e. any circular wavefront can be expressed as a linear combination of Zernike polynomials that is unique. The orthogonality in the radial part reads:

$$\int_0^1 R_n^m(\rho) R_{n'}^{m'}(\rho) \rho d\rho = \frac{1}{2(n+1)} \delta_{nn'}, \quad (2-24)$$

where δ_{ij} is the Kronecker delta. The orthogonality in the angular part can be proven by examining the four possible products:

$$\begin{aligned}
 \int_0^{2\pi} \cos(|m|\theta) \cos(|m'|\theta) d\theta &= \pi(1 + \delta_{m0})\delta_{|m||m'|}, \\
 \int_0^{2\pi} \sin(|m|\theta) \sin(|m'|\theta) d\theta &= \pi\delta_{|m||m'|}, \\
 \int_0^{2\pi} \cos(|m|\theta) \sin(|m'|\theta) d\theta &= 0, \\
 \int_0^{2\pi} \sin(|m|\theta) \cos(|m'|\theta) d\theta &= 0.
 \end{aligned} \tag{2-25}$$

The fulfilment of the condition for orthonormality follows from (2-24) and (2-25):

$$\frac{\int_0^1 \int_0^{2\pi} Z_n^m(\rho, \theta) Z_{n'}^{m'}(\rho, \theta) \rho d\rho d\theta}{\int_0^1 \int_0^{2\pi} \rho d\rho d\theta} = \delta_{nn'} \delta_{mm'}. \tag{2-26}$$

The aberration function Φ can be expressed as [8]:

$$\Phi(\rho, \theta) = \sum_{n=0}^{\infty} \sum_{m=-n}^n A_{nm} Z_n^m(\rho, \theta). \tag{2-27}$$

The coefficients A_{nm} are called the Zernike coefficients and constitute a simple way to evaluate the contribution of each type of aberration to the total phase of the wavefront, as well as a way to calculate the total wavefront variance. If all the A_{nm} are known, the wavefront error can be easily calculated from the orthonormality relations (2-24) and (2-25):

$$(\Delta\Phi)^2 = \sum_{n=1}^{\infty} \sum_{m=-n}^n \frac{A_{nm}^2}{2(n+1)}. \tag{2-28}$$

With this, we conclude the introduction of the mathematical tools required to work with aberrations. Since the mathematical derivations have been purposely kept to a minimum, this evidently does not provide a complete view of aberrations from a physical optics point of view. The interested reader is suggested to consult [1] and [3]

for further context. In the next section, the properties of a kind of highly aberrating biological samples, the tissue mimics, are discussed.

2.2. Tissue mimics

Cell cultures are one of the most powerful tools biologist have at their disposition to study issues such as cell growth or differentiation. Although two-dimensional monolayered cultures allow the study of many biological processes, they do not fully take into account the effects of the three-dimensional organization of cells and extracellular matrix within tissues. Since mammalian tissue is often inaccessible to in-vivo observation, the study of processes sensitive to the three-dimensional structure of the tissue such as organogenesis or tumour development has historically relied on model systems.

Tissue mimics (TMs) are 3D models of biological tissue that provide a more physiologically relevant microenvironment for the study of tissue and organ development. They typically consist of roughly spherical clusters of cells with a size of a few hundred microns that present similar differentiation patterns as their in-vivo counterpart, as well as a similar 3D network of cell-cell and cell-matrix interactions [9].

Over the last decades there has been a steady development of the TM field, and TMs of most tissues and organs (presenting partial or total function of the mimicked tissues) have been developed [10].

2.2.1. Optical properties of tissue mimics

The optical properties of a TM are crucial when attempting to image it, as they govern the behaviour of the optical signal entering and leaving the tissue. For this reason, samples that interact heavily with light must be regarded as yet another element of the optical system, and must be taken into account when designing an experiment.

In summary, the optical properties of a tissue can be described in terms of the refractive index of the tissue n , the absorption coefficient μ_a , the scattering coefficient μ_s and the scattering function $p(\theta, \psi)$, where θ is the deflection angle of scatter and ψ is the azimuthal angle of scatter [11].

Photons in a turbid medium such as a TM may be scattered or absorbed, in such a way that, when a photon propagates over an infinitesimal distance ds , the probability of scattering and absorption are $\mu_s ds$ and $\mu_a ds$, respectively. We can define another useful property of tissues: the mean free path (MFP) of a photon between scattering or absorption events. It is defined as:

$$\begin{aligned} MFP_s &= \frac{1}{\mu_s}, \\ MFP_a &= \frac{1}{\mu_a}. \end{aligned} \tag{2-29}$$

Hence, the probability that a photon is scattered (similar for absorption) in some distance $x < s$ is given by the probability distribution function [12]:

$$F_s(s) = 1 - e^{-\mu_s s}. \tag{2-30}$$

Since both absorption and scattering affect imaging, sometimes the total attenuation (or extinction) coefficient μ_r is used to account for their combined effect. It is defined as

$$\mu_r = \mu_s + \mu_a. \tag{2-31}$$

and it determines the possibility of a photon undergoing any of a scattering or absorption event. In most tissues $\mu_s \gg \mu_a$ so one may approximate $\mu_r \approx \mu_s$ [13].

When the tissue is illuminated by a collimated beam with intensity I_0 , the amount of light entering the tissue is reduced by several different mechanisms: a portion of the light is reflected at its surface, while another portion is scattered and absorbed by the tissue. If μ_r is uniform, the total intensity at any point x inside the tissue along the path of the beam is then given by Beer-Lambert's law:

$$I(z) = I_0(1 - R)e^{-\mu_r x}, \quad (2-32)$$

where I_0 is the intensity of the incoming beam, R is the reflectance of the surface, and μ_r is the attenuation coefficient.

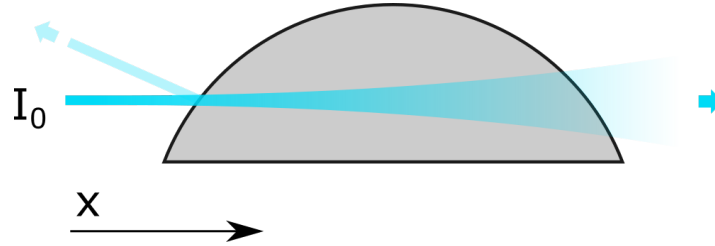


Figure 2-4: Beam propagating through a TM.

As seen above, the attenuation of a beam inside a tissue depends as much on the depth inside the tissue as it depends on the attenuation coefficient. For this reason, the thickness of a tissue d is not a good metric to evaluate ease of imaging. Instead, the optical thickness or optical depth (τ) is usually preferred, and is defined as:

$$\tau = \mu_r d. \quad (2-33)$$

Single scattering is a complex problem, and many different scattering functions $p(\theta, \psi)$ have been proposed to describe it. When many scattering events are present, like in TMs, the random orientation of scattering structures causes the contribution of the azimuthal angle of scatter ψ to average out and, thus, the dependence of ψ can

be ignored. Multiple scattering also means that the contribution of θ can be described by an average parameter:

$$g = \langle \cos \theta \rangle, \quad (2-34)$$

called the anisotropy of scatter. g accounts for the relative forward versus backward direction of scattering.

The situation in which scattering is much more probable than absorption ($\mu_a \ll \mu_s$) is called the diffusion regime. In this case, it usually is useful to use the reduced scattering coefficient and the transport mean free path, defined as:

$$\mu'_s = \mu_s(1 - g), \quad (2-35)$$

$$TMFP = \frac{1}{\mu'_s} = \frac{MFP}{1 - g}. \quad (2-36)$$

The propagation of a beam between 0 and 1 MFP inside a tissue is largely ballistic. Scattering increases photon diffusion up to 1 TMFP, after which almost no ballistic light is present [13].

In mammalian tissue, microstructures include organelles (0.2 – 0.5 μm), mitochondria (1 – 4 μm), nuclei (3 – 10 μm) and whole cells (10 – 30 μm). Most structures have a size comparable or greater than the wavelength of the light used, which situates TM imaging in both the Rayleigh and Mie scattering regime.

Scattering and absorption depend on the wavelength of the signal. Notably, scattering diminishes with increasing wavelength, while the absorption profile depends on the medium. For water, there is a near-infrared optical imaging window, from 700 nm to 1400 nm, in which absorption is minimal and scattering is significantly reduced. This window is commonly exploited for optimal imaging of thick samples [14].

Soft tissues present refractive indexes around $n = 1.35$, with variations of about 0.04 – 0.10 within the tissue [15]. Since TMs are commonly immersed in water for

imaging ($n = 1.33$), the refractive index difference between the tissue and the surrounding medium, as well as its variance within the tissue, produces optical aberrations.

Aberrations are a major cause of image degradation on thick biological samples. Typically, low order aberrations such as astigmatism, coma and spherical are the most prevalent [16]. Since refractive index vary irregularly across the specimen, sample-induced aberrations are not constant across the field of view (FOV). The regions in which the aberrations can be considered as constant for a given purpose are said to be isoplanatic. The mean isoplanatic patch size of a sample depends on its heterogeneity, being smaller for highly heterogeneous tissue. One of such highly heterogeneous TMs of particular interest are the multi-cellular tumor spheroids, widely used to study cancer development, which present significant challenges for modern optical imaging.

2.2.2. Multi-Cellular Tumor Spheroids

Multi-cellular tumour spheroids (MCTS) are three-dimensional cultures of tumour cells grown in a roughly spherical shape. This kind of TM has proven invaluable in the study of cancer progression and treatment as they present many of the features of in-vivo tumours. Spheroids can be grown from established tumour cell lines or even directly from primary tumours

The outer layers of an MCTS are rapidly dividing, while the proportion of quiescent cells increases in the inner regions. Due to the lack of vascularization, metabolite gradients are significant between the inner and the outer layers of an MCTS, and given enough growth it will eventually develop a necrotic core as a consequence of hypoxia and build-up of metabolic waste [17].

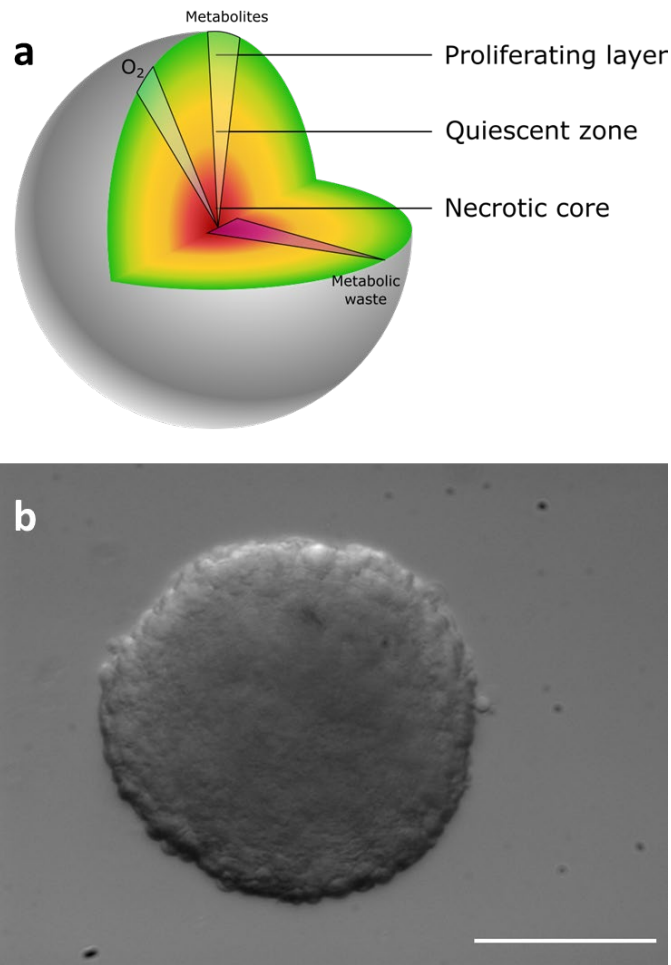


Figure 2-5: (a) Structure of an MCTS. Gradients of O₂, nutrients and metabolic waste divide the MCTS into a proliferating rim, a quiescent zone, and a central necrotic core. (b) Widefield image of an MCTS. Scale bar: 150 μm .

MCTS are notoriously difficult to image due to their heterogeneity. Andilla et al. report scattering coefficients for fixed MCTS made from the HCT116 human colon carcinoma cancer cell line to range from $5,3 \text{ mm}^{-1}$ for a 532 nm wavelength to $2,5 \text{ mm}^{-1}$ for 1040 nm. This corresponds to an MFP of 0.19 mm and 0.40 mm, respectively, meaning the chance of multiple scattering within a medium-sized 400 μm spheroid is likely for visible light [9].

Regarding healthy colon submucous tissue, Bashkatov et al. report scattering coefficients of approximately 10 to 7.5 mm^{-1} for 500 – 1000 nm wavelengths, and 32 to 21 mm^{-1} in the case of mucous tissue [18]. The optical properties of non-healthy tissue are similar. According to Wei et al., the scattering coefficient of adenomatous human colon mucosa and submucosa are 22.3 mm^{-1} for a 532 nm wavelength, while that of healthy mucosa/submucosa is 20.8 mm^{-1} [19]. They also report absorption coefficients of 0.52 mm^{-1} and 0.33 mm^{-1} for adenomatous and healthy tissue, respectively.

Hence, while healthy and tumoral human colon tissue seem to have similar optical properties, fixed MCTS are considerably less opaque, with a scattering coefficient four times lower.

MCTS derived from other human tissues have also been characterized. Work done by Hargrave et al. provides scattering coefficients ranging from 90 to 40 mm^{-1} for wavelength in the 650 - 1000 nm range in fixed MCTS made from the POC human small-cell lung cancer cell line [20], as well as absorption coefficients of 0.2 to 0.1 mm^{-1} for the same wavelengths. This is again in dissonance with the properties of in-vivo healthy lung tissue, for which Beek et al. provide scattering coefficients of 20 to 35 mm^{-1} for a 632.8 nm wavelength, depending of lung volume [21]. Is worth of note that, as opposed to colon MCTS, lung cancer fixed MCTS are more difficult to image than the in-vivo healthy tissue. Unfortunately, to the knowledge of the author no data is present in the literature about the optical properties of human lung tumours, so it is not possible to assess whether or not optical properties of MCTS differ from those of tumoral tissue.

So far, we have only discussed properties of fixed MCTS. While it is well known that fresh MCTS are more difficult to image, this fact has attracted little attention by the scientific community. Indeed, the only research to date that compares the optical properties of fixed and fresh spheroids is the previously mentioned work of Hargrave and co-workers regarding lung MCTS [20]. There, they report scattering

2.2. TISSUE MIMICS

coefficients of approximately 160 to 90 mm^{-1} for wavelengths in the 650 – 1000 nm range for fresh MCTS, i.e., 30% to 100% higher than those their fixed counterparts. Absorption coefficients range from 0.4 mm^{-1} in the visible to less than 0.01 mm^{-1} in the NIR.

Table 2-1: Scattering coefficients μ_s (mm^{-1}) for healthy tissue, tumoral tissue and MCTS for visible and near-infrared wavelengths. (a) Colon tissue. (b) Lung tissue.

a	Healthy tissue	Tumoral tissue	Fixed MCTS
Visible	10 to 32	22.3	5.3
NIR	7.5 to 21	-	2.5

b	Healthy tissue	Fixed MCTS	Fresh MCTS
Visible	20 to 35	90	160
NIR	-	40	90

In MCTS, the scattering contribution to attenuation far outweighs absorption. As seen above, absorption coefficients are one or two order of magnitude lower than scattering coefficients. It is worth noting that fixed spheroids have a much more stable absorption coefficient with respect to wavelength. While fresh lung MCTS μ_a goes from 0.4 mm^{-1} in the visible to almost vanishing in the NIR, fixed MCTS keep a fairly stable profile after 650 nm, with an almost constant μ_a of 0.1 mm^{-1} .

MCTS made from the HCT116 cell line have a refractive index between 1.35 and 1.39 [22], which is noticeably different from that of water ($n = 1.33$). Optical imaging of MCTS suffers from major aberration induced by the highly heterogeneous

refractive index across the spheroid. Coma, astigmatism and trefoil are the most prominent aberrations in MCTS [23], [24].

The highly scattering and aberrating nature of MCTS is of special relevance when choosing an optical imaging method, especially given the limitations imposed by their intrinsic three-dimensional nature. The following section provides an overview of the available alternatives for MCTS imaging, as well as an in-depth dive into our tool of choice, light sheet fluorescence microscopy.

2.3. Light sheet Fluorescence Microscopy

2.3.1. Tissue mimics and microscopy

Due to its unmatched ability to determine their morphology, optical imaging is essential in the study of TM behaviour [25]. However, imaging of thick samples such as TMs is a non-trivial task due to scattering- and aberration-related image degradation.

A straightforward way to acquire 3D images while avoiding such degradation is physical sectioning of the sample into slices thin enough to be imaged without loss of information. This technique, combined with immunostaining, has been successfully applied in the study of brain organoids [26]. Still, while providing useful insight, the destruction of the sample has obvious shortcomings in live imaging.

Since physical slicing is out of the question for work with live samples, researchers have usually favoured optical sectioning for TM imaging. Confocal microscopes are the most popular instruments to allow precise optical sectioning. By using a pinhole, out-of-focus light can be blocked, providing subcellular optical sectioning over suitable FOVs [27], [28]. Since most of the light is blocked out, the sample has to be exposed to high amounts of light, leading to high levels of phototoxicity and

photobleaching. This issue makes confocal microscopy a less-than-ideal approach for sensitive live imaging.

Two-photon microscopy is another well-known method for high-resolution 3D imaging. It works by exploiting the low probability of occurrence of two-photon excitation event in a fluorophore, which requires very high intensities to reliably take place. By focusing a near-infrared laser into a fluorophore, these high intensities will only be present near its focus, thus providing a way to precisely confine excitation in three-dimensions. The laser can be scanned across the sample to provide thin plane images deep into the sample [29]. Since NIR light is weakly absorbed by biological tissue and no fluorescence light is discarded, two-photon excitation is a much gentler approach than confocal microscopy for living samples.

In recent years, another TM imaging method, the light sheet fluorescence microscopy, has become increasingly popular owing to its negligible photodamage and fast acquisition times, which make it an ideal tool for long term live imaging of thick samples. A detailed (though by no means exhaustive) overview of LSFM and its different modalities is presented below.

2.3.2. Basics of LSFM

LSFM is a powerful technique for three-dimensional live imaging of biological samples that permits imaging large specimens over long periods of time. Typically, LSFM involves illuminating the sample with a beam, shaped into a thin sheet (the light sheet), in such a way that only a plane with thickness equivalent to that of the light sheet is excited. The fluorescence light emitted from this plane is collected by a perpendicular objective and registered by a camera as the sample moves through the light sheet, producing a three-dimensional image of the sample. This selective illumination pattern has the advantage that no out-of-focus light has to be filtered, yielding high signal-to-noise ratio (SNR) and precise optical sectioning, while requiring no pinhole schemes. As the whole light emitted from the sample is

registered, LSFM can image with low acquisition times, resulting in a very low phototoxicity for the sample [30]. When imaging with LSFM, a zebrafish embryo is exposed to as much as 5000 times less energy than with confocal microscopy [31].

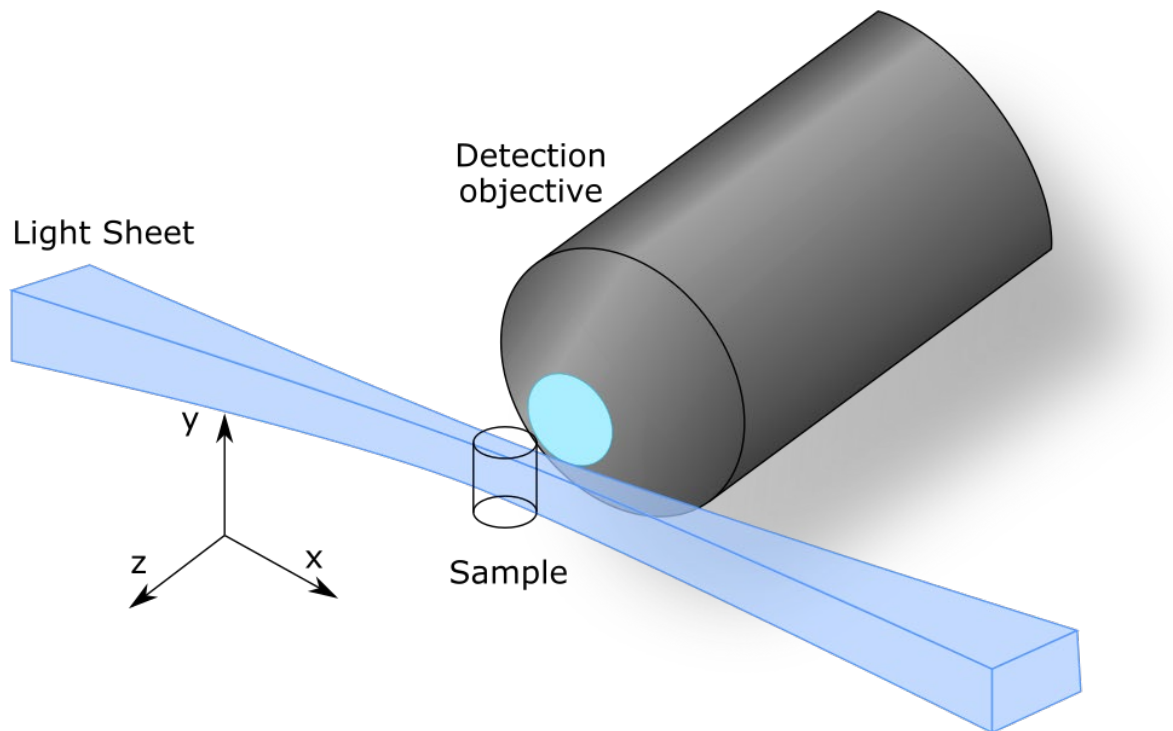


Figure 2-6: SPIM setup.

The first light sheet device to come to existence was the Orthogonal-Plane Fluorescence Optical Sectioning microscope (OPFOS) developed by Voie et al. [32]. This instrument was able to provide optical sectioning by using a light sheet, but was limited to an almost macroscopic resolution. In 2002, Fuchs et al. developed their Thin Light Sheet Microscope (TSLM), which was capable of resolving single bacteria [33]. However, TSLM does not provide optical sectioning, as its intended use is the identification of microorganisms in sea water as opposed to 3D imaging of biological tissue. It was in 2004 that Huisken et al. developed the Selective Plane Illumination Microscope (SPIM) [34], employing it for *in-vivo* imaging of GFP-labelled Medaka

fish *Oryzias latipes* and embryogenesis of the fruit fly *Drosophila melanogaster*. Embryogenesis remains one of the most popular applications of LSFM.

SPIM was the first light sheet microscope to achieve wide awareness and provided the cornerstone that set the LSFM field in motion. Since then, the push for ever higher resolution and speeds has driven the scientific community to develop a plethora of LSFM schemes for imaging in any resolution range, from the macroscopic to super-resolution.

2.3.3. Resolution and speed in LSFM

Due to the decoupling of the illumination and detection paths, LSFM resolution and field of view depend on the NA of both the illumination and detection objectives. High NA illumination objectives will produce a thinner light sheet, improving axial resolution, while a high NA detection objective provides high lateral resolution. However, a common issue in high-resolution instruments is the mechanical constraints limiting objective placement, as high NA objectives are typically bulky and have short working distances. Since they collide with each other when placing them at short distances, it is usually impossible to arrange a system in which the sample is in the focal plane of both orthogonal high NA objectives.

Many schemes have been developed to overcome this problem. A simple solution is to use a low NA illumination objective, permitting longer work distances and more distance between the objectives [35]. Obviously, this approach limits optical sectioning and axial resolution. In single molecule detection microscopes, this loss of depth information can be compensated by means of depth-dependent astigmatism [36], but in many applications where axial resolution is critical an alternative solution has to be sought. Custom-made objectives can reduce the spatial constraints to an extent [37], [38], but their cost can be prohibitive for most microscopists.

Despite the mechanical constraints, super-resolution can be achieved in LSFM using off-the-self components by modifying the geometry of the system. Gebhardt et

al. developed the first of such systems, the reflected light sheet microscope (RLSM), using two opposed objectives with a 45° mirror cantilever between them [39]. The cantilever redirects the light sheet incoming from the illumination objective into the detection focal plane, allowing the use of NA=0.8 and NA=1.4 oil immersion objectives in the illumination and detection paths, respectively.

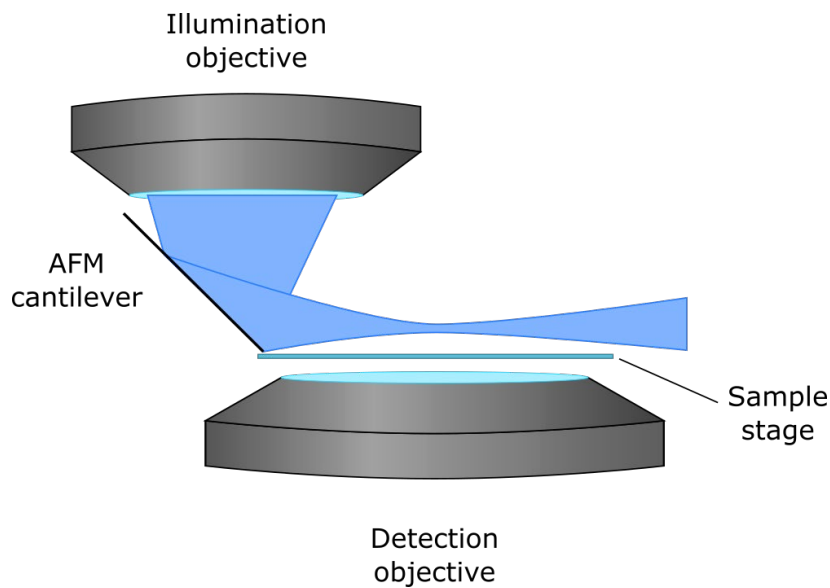


Figure 2-7: Detail of the RLSM illumination scheme.

Oblique illumination techniques have acquired some relevance in the LSFM field. The Highly Laminated Optical sheet microscope (HILO), developed by Tokunaga et al. [40] uses a single objective to generate an oblique light sheet (by off-axis incidence on the objective) and collect the fluorescence light emitted. However, the obliqueness of the light sheet introduces an unavoidable defocus, which is more severe in regions that are the furthest away from the centreline of the image, limiting the effective FOV. This defocus cannot be fixed by simply tilting the detector, as spherical aberrations would arise [41]. Dunsby et al. address this issue in their Oblique Plane Microscope (OPM) by concatenating another oblique microscope in such a way that the axially tilted image formed by the first microscope rests in the focal plane of the

2.3. LIGHT SHEET FLUORESCENCE MICROSCOPY

second (Figure 2-8) [42]. Swept confocally-aligned planar excitation (SCAPE, Bouchard et al.) microscopy improves this design by introducing a scanning mirror, permitting imaging frequencies of up to 20 volumes per second [43]. Furthermore, integrated one- and two-photon scanned oblique plane illumination (SOPi) microscopy (Kumar et al. (Kumar 2018)) integrates two-photon illumination to the SCAPE design, while simplifying it and correcting scan-position dependent tilt of the light sheet present in SCAPE [44].

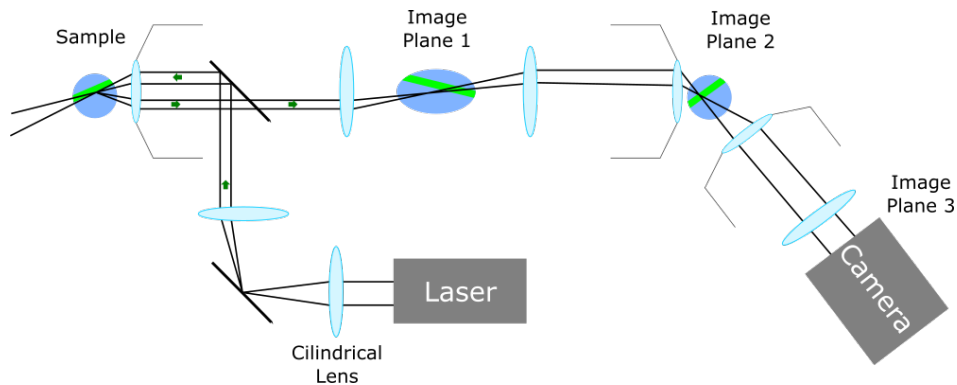


Figure 2-8: OPM setup.

The π SPIM system developed by Theer et al. is a different take on oblique illumination. In this setup, as opposed to single objective systems, the light sheet is created oblique to the illumination objective, while a detection objective is placed perpendicular to the light sheet [45]. In this way, a NA=1.1 detection objective can be used with a NA=1.49 illumination objective, though actual illumination NA is limited by the inclination of the light sheet.

Single objective setups have also seen success in orthogonal illumination. Galland et al. iterated over the RLSM design in their single objective SPIM (soSPIM), in which the light sheet is introduced into the sample from the detection objective and a cantilever is used to place it in the focal plane, in a similar way to RLSM [46]. In this approach, the sample placement is fixed, and the light sheet is horizontally scanned

through the tilted mirror, displacing it axially through the sample. To keep the light sheet in the focal plane, the objective lens is also translated. This entails a horizontal displacement of the light sheet waist, which must be compensated by a tunable lens.

Another single objective setup is the Axial-Plane Optical Microscope (APOM) developed by Li et al. APOM uses the objective to create a light sheet illuminating a plane parallel to the optical axis while a tilted mirror further down the optical path rotates the image over the axis into a lateral image that is registered by a camera. This way, APOM can simultaneously produce a widefield image and an axial SPIM image of the sample using an NA=1.4 oil-immersion objective [47]. The fact that all the required optics for the axial image are remote makes this design easy to implement in a conventional widefield microscope as a module.

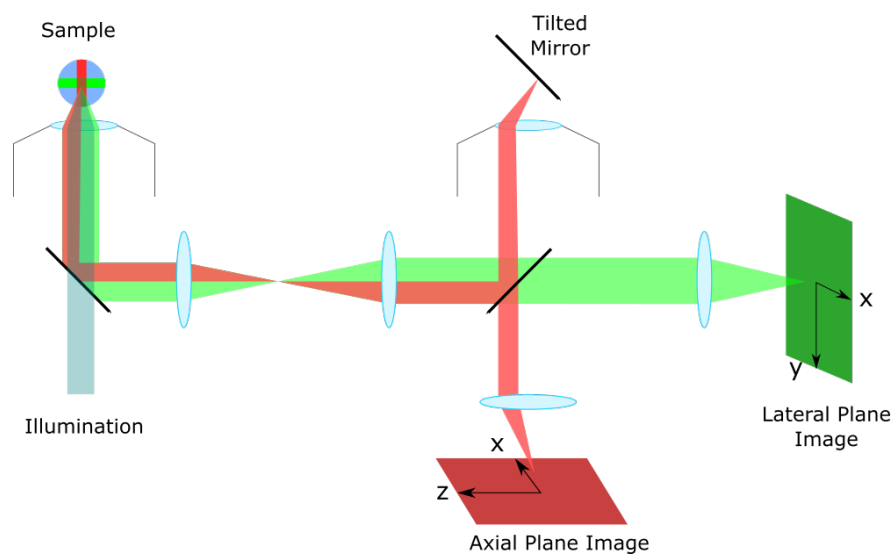


Figure 2-9: APOM microscope. The tilted mirror reflects the axial image of the XZ plane into a lateral image, while a widefield image of the XY plane is registered by another camera.

LSFM systems have been pushed not only to the limits of spatial resolution, but also to the limits of imaging frequency. Since the light sheet must be placed in the focal plane of the objective, sample translation is usually required for volume

imaging. This limits the amount of volumes that can be imaged per second, since fast shacking of the sample will destroy it. By keeping the sample still and scanning the light sheet through it, fast imaging can be achieved. However, the light sheet must be kept in the focal plane through the process in order to allow imaging.

The first of such approach to use this strategy was the Objective-Coupled Planar Illumination microscopy (COPI), developed by Holekamp et al. [48]. In this microscope, both the light sheet and the objective move by means of a piezoelectric manipulator, keeping the light sheet always on focus. Speeds of 5 volumes per second were achieved for calcium imaging of mouse vomeronasal organ.

Fahrbach et al. employed an electrically tunable lens to maintain focus without moving the objective [49]. This way, they achieved imaging at up to 100 volumes per second. Another high-speed system is the previously mentioned SCAPE design, which uses a descanning mirror to keep focus and allow speeds of up to 20 volumes per second [43].

Olarte et al. avoid the use moving parts by employing a phase mask coupled with image deconvolution to extend the depth of field of the objective so the light sheet is always focused. In this way, they achieve imaging of up to 70 volumes per second [50].

Ultimately, the speed of these systems is limited not by their optics, but by camera framerates. Hence, further improvement in LSFM speed is unavoidably linked to the development of faster commercial cameras.

2.3.4. The light sheet

As the characteristic element of LSFM, the light sheet plays an essential role in not only optical sectioning and axial resolution, but also in imaging depth. The ideal light sheet should be as thin as possible at the waist, while maintaining a thin profile over a large FOV. It is evident, however, that these two properties are mutually exclusive: a thin waist is only achievable by using a high NA objective, but this

means a more acute divergence of the light sheet, which translates to a smaller effective FOV.

In addition, light sheet degradation is a concern for LSFM. Inhomogeneities in the sample cause aberration and scattering, resulting in a broadening and loss of quality of the light sheet as it passes through the sample. This leads to a compromised optical sectioning and loss of axial resolution, as well as the apparition of artifacts.

The last issue that needs to be considered for light sheet engineering is phototoxicity. One of the most attractive properties of LSFM is the need for low exposures of the sample, and it is generally taken as given. However, the required exposure and peak intensity delivered to the sample depends greatly on the modality of illumination and it can be far from harmless. Hence, the choice of the illumination system should always be addressed with consideration of not only the resolution and penetration needs, but also the effects of imaging on the biological system under study.

2.3.4.1. Light sheet properties

In this section, the most relevant properties of a Gaussian light sheet (the one used in our system) will be explained. The axial resolution of a LSFM system is given by both the NA of the detection objective and the thickness of the light sheet. Since the light sheet is focused by an objective, it has a hyperbolic profile, which means that there is one point of the beam at which its thickness is minimal. This point, placed at a focal distance of the objective, is called the waist, and its thickness w_0 is perhaps the most relevant property of a light sheet. The beam waist thickness is given by:

$$w_0 = \frac{n\lambda}{\pi NA}, \quad (2-37)$$

where n is the refractive index of the medium, λ is the wavelength of the beam and NA is the numerical aperture of the objective. In most applications, the light sheet is thinner than the depth of field of the detection objective, meaning that the axial

2.3. LIGHT SHEET FLUORESCENCE MICROSCOPY

resolution R_{ax} depends on the optical sectioning capability of the system and can be approximated as the thickness of the light sheet, i.e. $R_{ax} = 2w_0$.

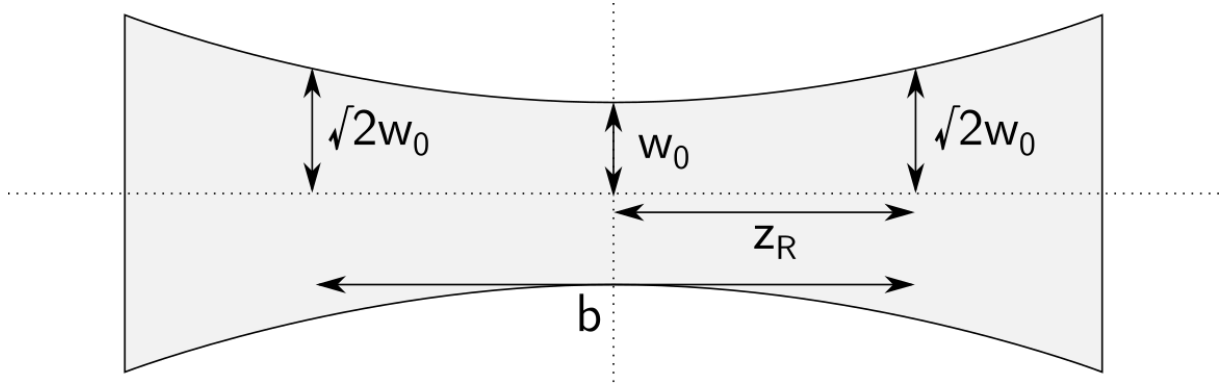


Figure 2-10: Main properties of a light sheet.

The other defining property of the light sheet is its Rayleigh range z_R , which determines the distance from the waist to the point where the beam has become thicker by a factor of $\sqrt{2}$. The Rayleigh range depends directly on the waist thickness, and is given by:

$$z_R = \frac{\pi w_0^2}{\lambda}. \quad (2-38)$$

It is usually considered that the useful portion of the light sheet is that which rests in the Rayleigh range. The total FOV provided by the light sheet is then given by twice the Rayleigh range $FOV = 2z_R$. This distance is sometimes referred in older literature as the confocal parameter $b = 2z_R$. The confocal parameter also provides the full width at half maximum (FWHM) of the axial intensity distribution of the beam.

It is evident from (2-37) and (2-38) that the FOV of a system can be increased by the user of a lower NA objective. However, a lower NA will reduce the optical sectioning capability of the system, since the waist thickness will also increase. This places a fundamental limit on Gaussian light sheets, as a large FOV and high sectioning capability cannot be achieved at the same time.

2.3.5. Illumination modalities

The simplest and most common kind of light sheet is the one created by a Gaussian beam passing through a cylindrical lens, commonly referred as the Gaussian light sheet and first used by Voie et al. [32]. Cylindrical lenses focus light in just one dimension, resulting in a plane of light that is then focused by the illumination objective and introduced into the sample. Though easy to create and practical, static Gaussian light sheets' optical sectioning is typically not better than $1\mu\text{m}$. In addition, shadow artifacts are created as the light sheet encounters opaque obstacles in its path, creating a stripe pattern characteristic of LSFM images.

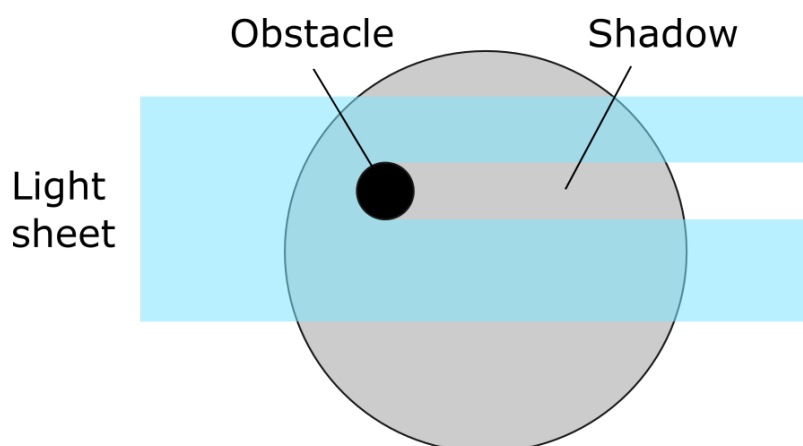


Figure 2-11: Stripe artifact created by the blocking of the light by an obstacle.

Another issue with light sheets in general is the fact that scattering will broaden the light sheet as it passes through the sample, compromising optical sectioning on the far side of it.

Huisken and Stainier addressed both issues of shadow artifacts and asymmetrical optical sectioning over the FOV with their multidirectional selective plane illumination microscope (mSPIM) [51]. In this setup, they illuminate the sample with two opposing light sheets, reducing the effect of scattering, and pivot them vertically over a 10° arc. This way, they severely reduce the stripe artifacts, while increasing

axial resolution by a factor of $\sqrt{2}$. By imaging the sample at different angles, a well resolved 3D image can be acquired. Of course, the several acquisitions entail an increased exposure time along with its associated issues of phototoxicity and photobleaching.

MuVI-SPIM (Krzic et al. [52]) and SIMView (Tomer et al. [53]) take this approach a step further, incorporating a second opposed detection objective. This way, the need for rotation of the sample is reduced and the temporal resolution is increased by a factor of 2 over mSPIM.

Digitally scanned light sheet microscopy (DSLM) provides an alternative and more effective approach to stripe artifact reduction, as shown by Keller et al. [31]. In DSLM, a Gaussian beam is rapidly scanned through the sample, creating a virtual light sheet. Since the pixel dwell time decreases, an increased peak illumination intensity is required in order to achieve a comparable SNR. It has been reported that DSLM operates in a linear photobleaching regime and this does not result in increased photodamage to the sample compared to SPIM [31]. Still, there is strong evidence that this is not the general case (since photodamage is in general not linear) and peak intensity is a better indicator of photodamage than total exposure [38], [54].

Even in DSLM, Gaussian light sheets are not able to achieve subcellular resolution over large FOVs. Non-diffracting beams provide an alternative approach to this problem. Though the laws of electromagnetism (and thus, diffraction) still govern these kinds of beams, they behave as non-diffracting over a small region. As a result, they maintain an invariable profile over this region, usually several times the size of the FOV of a Gaussian beam.

The Bessel beam is probably the most common of these beams. They are usually created by focusing a Gaussian beam with an axicon lens, and their cross-section consists on a central lobe surrounded by rings of diminishing intensity. One of the most interesting properties of Bessel beams is their self-healing nature: when the inner portion of the beam encounters an obstacle, the beam reforms at a short

distance after it [55]. This effect increases penetration depth in thick tissue and makes Bessel beams a powerful tool when imaging heterogeneous samples.

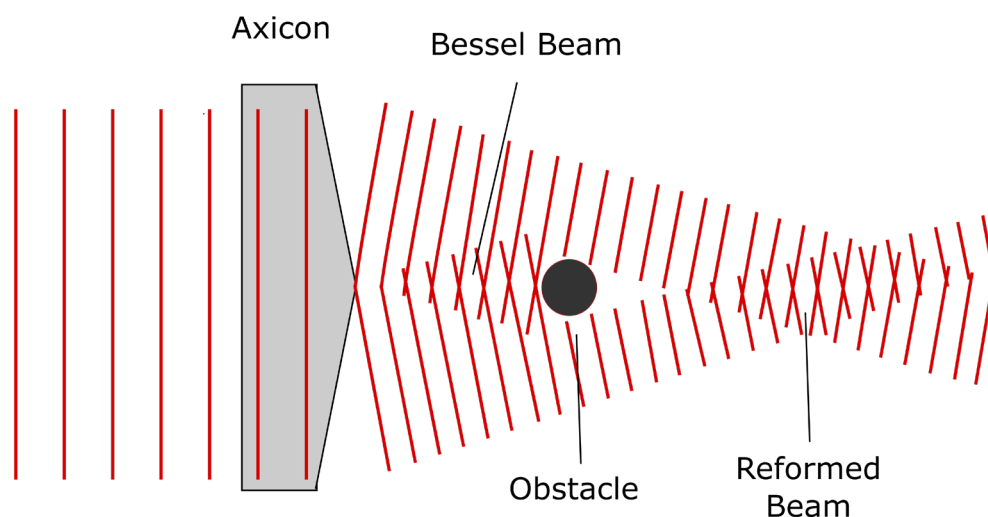


Figure 2-12: Self-healing nature of a Bessel beam. The beam is reformed shortly after encountering an obstacle.

Planchon et al. used a scanned Bessel beam (in a similar way to DSLM) to provide a near-isotropic 290 nm resolution over a 40 μm FOV [56]. Still, Bessel beams produce out-of-focus light originating from side lobe illumination, which compromises the optical sectioning capability of the system and increases exposure of the sample. To address the first issue, they incorporated an optical sectioning algorithm (OS-SIM, Neil et al. [57]) to their system, allowing them to remove the out-of-focus light at the cost of greatly increased phototoxicity. However, the strict validity of the reconstructed images resulting from the OS-SIM algorithm is unclear [58].

Gao et al. improved upon this system by introducing Bessel beam superresolution structured plane illumination (Bessel plane SR-SIM) [58]. This system uses an array of parallel Bessel beams, providing a 50% increase in resolution while requiring a lower peak intensity and diminishing the amount of photodamage to the sample.

2.3. LIGHT SHEET FLUORESCENCE MICROSCOPY

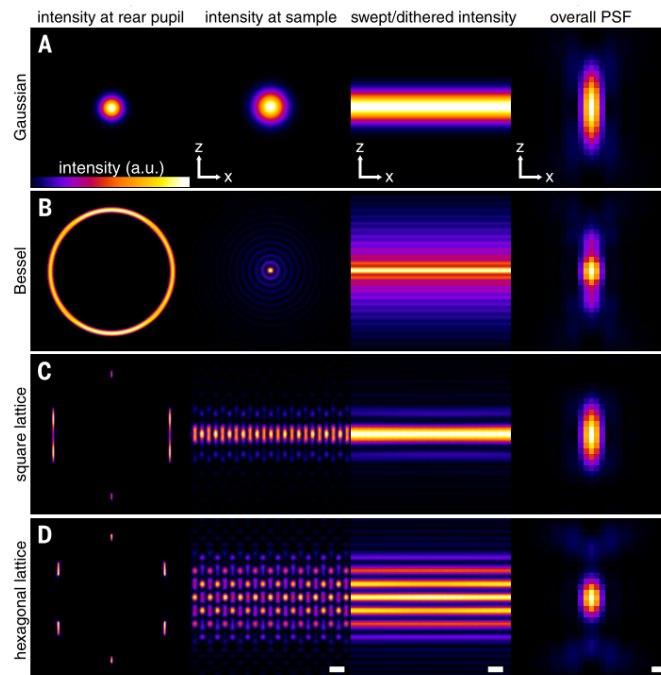


Figure 2-13: Properties of Gaussian and Bessel beams, and square and hexagonal lattices. Modified from [38].

By coherent superposition of several beams, one can create a 2D periodic interference pattern called an optical lattice. Just like a Bessel beam, optical lattices are non-diffractive over a region, making them a suitable candidate for a light-sheet. Moreover, optical lattices can be easily engineered in order to accommodate the needs of the system, such as lower background or higher axial resolution.

Lattice light sheet microscopy (LLSM) was introduced by Chen et al., making use of the periodicity of optical lattices to provide exceptional optical sectioning while delivering low peak intensity to the sample [38]. In their 2014 article, Chen et al. use two lattices: square and hexagonal. Square lattices produce little out-of-focus fluorescence and can be designed so that the out-of-focus contributions fall within the minima of the detection PSF. The lattice is dithered to create the light sheet, effectively imaging a single plane. In this mode, LLSM can acquire up to 1,000 frames

per second, delivering extremely low peak intensities to the sample and reducing phototoxicity by an order of magnitude when comparing to scanned Bessel beams.

The hexagonal lattice was used in combination with SIM to provide superresolution images by taking advantage of the periodic light sheet. Several images were taken for each z plane, stepping the lattice light sheet a fraction of its period between images. These preliminary images could then be used to reconstruct a 3D image with resolution beyond the diffraction point (280 nm axial resolution compared to the diffraction-limited 370 nm in dithered mode).

Both modes can provide high temporal and spatial resolution, though the resolution gain of SIM requires slower acquisition and increased phototoxicity. Overall, LLSM provides the best optical sectioning and resolution of all the LSFM variants.

2.3.6. The penetration problem

Volume imaging of large biological samples presents the unavoidable problem of image degradation. Due to inhomogeneities present in the sample, sample-induced aberrations, absorption and scattering degrade the light passing through it resulting in a loss of SNR and high-frequency detail which tends to worsen at greater depths. This is especially relevant in LSFM, as both the illumination and detection paths suffer from it. The light sheet will broaden when entering the sample, leading to a degraded optical sectioning and loss of axial resolution, while the degradation in the detection path leads to a loss of lateral resolution.

Sometimes, highly scattering structures can simply be removed from the organism. For example, dechoriation (removal of the outer opaque layers of an embryo) is a routine approach to zebrafish embryo imaging as it greatly improves light penetration while producing no substantial physiological effects [59].

When physical removal of scattering structures is not feasible, sample clearing is another popular approach, consisting in homogenising the refractive index of the

sample using a chemical agent. While clearing significantly reduces scattering and aberration arising from the sample, it invariably requires killing it, making this technique incompatible with live imaging.

Since removal of aberrations and scattering at the sample level is not always feasible or even desirable, they should be lessened either by the illumination or after detection. Regarding illumination, this involves increasing penetration depth of the light sheet and reducing scattering underwent by it (and hence background fluorescence).

Both scattering and absorption are wavelength dependent. Scattering generally decreases for longer wavelengths, while the absorption profile depends on the medium. Very long wavelengths incur less scattering, but their use is not always desirable since they limit resolution and, more importantly, absorption coefficients of biological tissue increase dramatically after 1300 nm. Notably, for biological tissue there exists an optical window in the near-infrared range in which absorption is minimal and scattering is greatly reduced. This window can be employed to achieve greater penetration, generally at the cost of resolution.

Wang et al. [60] used NIR excitation and emission to image large chunks of mammal tissue. They employed a 785 nm light sheet to achieve a penetration of up to 2.1 mm in glycerol-cleared brain tissue, and different fluorescent probes (emitting in the 850 – 1700 nm range) permitted cellular resolution imaging up to 2.5 mm deep.

NIR excitation was also exploited by Truong et al., who combined two-photon excitation with SPIM (2P-SPIM) [61]. Instead of the usual light sheet, they scanned a focused NIR pulsed laser vertically through the sample. Due to the quadratic dependence of fluorescence emission with two-photon excitation intensity, precise optical sectioning could be achieved, delivering better axial resolution than both single-photon SPIM and two-photon scanned laser microscopy. Since scattered light is not intense enough to undergo two-photon excitation, 2P-SPIM produce little background light, improving lateral resolution over 1P-SPIM.

This method was further explored by Olarte et al. [62], who combined 2P-SPIM with Bessel beam illumination. This illumination method delivered a six-fold increase of the lateral field of view, but imposed a 40% loss of lateral resolution.

In the end, no matter how good the illumination system is, fluorescence light must pass through the sample to reach the objective, and this process will always degrade the image as a consequence of scattering and aberration. Fortunately, image quality can also be improved after collection. Indeed, by using adaptive optics, the aberrations induced by the sample and the system can be compensated, allowing undistorted imaging at depth.

2.4. Adaptive Optics

2.4.1. Introduction

Aberrations are an unavoidable effect of light passing through a heterogeneous medium. All across history, optical scientists have encountered the problems posed by them (Newton mentions the “tremulous motion of shadows” as far back as 1730 in his *Opticks* [63]), but little progress was made towards improving imaging conditions when aberrations were present until the second half of the 20th century with the apparition of adaptive optics (AO).

AO is a discipline that seeks to improve an optical signal travelling through a medium by manipulating its phase. This involves the use of a phase modulation device (like a deformable mirror or spatial light modulator) that is able to influence the wavefront of the signal in such a way that it compensates all the distortions produced by its passing through the medium. For this, three elements are usually required: a phase modulator, a wavefront sensor and a point emitter of light (the guide star).

A distinction is commonly made between *active* and *adaptive* optics. Some authors argue that everything having to do with actively controlling a beam of light is active optics, while adaptive optics is limited to the control of light in a real-time fashion by means of a feedback loop [3]. This distinction is often made based on other parameters such as the modes of aberration corrected [64] or the bandwidth of the system [65]. For this dissertation, we will use the first definition, with the key element of the presence of a feedback loop being the difference between active and adaptive optics.

AO as a field has been developing over 7 decades since its first modern apparition in 1953, when Babcock presented the concept for an instrument based on a deformable optical element with feedback from a wavefront sensor for its use in large telescopes (that was never implemented) [66]. Nowadays, AO is not only present in all of the largest telescopes, but it is also essential in applications such as beam shaping and optometry. In recent years, AO has been slowly finding its way into optical microscopy.

Booth and Wilson were the first to propose the use of an aberration correction device for microscopy in 2001 [67]. A year later, they implemented AO in a confocal microscope, showing enhanced contrast and axial resolution [68] and opening the way for AO utilization in other systems. Another later application of AO in confocal microscopy came from Azucena et al., who decoupled imaging and wavefront reading by using different wavelengths for each of them [69].

The benefits of AO have not been limited to confocal microscopy. Sherman et al. [70] demonstrated the use of AO in a two-photon excitation microscope imaging inert coumarin solutions. This approach was later used to improve imaging of fixed mouse embryos [71] and in-vivo mouse brain [72]. Wang et al. employed an infrared guide star to further improve imaging depth of in-vivo mouse brain up to 700 μm [73].

More recently, AO has been incorporated in super-resolution systems such as STED [74] and STORM [75]. Thomas et al. developed an adaptive structured

illumination microscope (SIM), in such a way that both the illumination beam and the collected imaged are shaped by a deformable mirror. This allowed them to achieve 140 nm resolution up to 35 μm deep into a *C. elegans* sample while substantially improving image reconstruction [76].

LSFM is an excellent match for AO, since both the illumination and the detection paths of the microscope can be optimized [77], [78]. Recently, Hubert et al. employed an adaptive LSFM to perform guide-star-less corrections in *Drosophila melanogaster* using extended sources for wavefront sensing [79].

Of especial interest to us is the use of adaptive LSFM in TM imaging. Jorand et al. [23] used AO to correct significant aberration in fixed MCTS, improving image quality up to 197 μm deep using fluorescent beads as guide stars. Even deeper corrections can be made by previously clearing the sample. Indeed, Masson et al. [24] developed a model of aberration produced by cleared MCTS and used it to improve resolution at depths of up to 300 μm . It is worth noting that, in this work, aberrations were estimated beforehand as opposed to measuring them during imaging.

TM imaging with adaptive LSFM was further explored by Liu et al. [80]. They developed an adaptive LLSM, able to correct the aberrations of both the lattice light sheet and the image. Given the sensitivity of lattice light sheets to sample-induced aberrations, their correction with AO is fundamental to enhance penetration. In their work, they study in-vivo processes such as clathrin dynamics and organelle morphology, imaging them with diffraction-limited resolution inside zebrafish embryos. By making use of tiled corrections, they achieve consistent resolution over the whole field of view. Though most of their work is done in zebrafish, they briefly demonstrated the ability of their system to perform aberration correction up to 40 μm deep in human stem-cell derived organoids, which allowed them to clearly locate previously-unresolved subcellular features. This same system was employed by Schöneberg et al. to image human intestinal epithelial organoids with similar performance [81].

In conclusion, AO can substantially improve image quality in different optical systems when imaging thick samples, opening the door to precise imaging of dynamics that were previously unreachable by optical microscopy. But AO is a complex process. In this section, a basic overview of AO will be given, with focus on its two main steps: wavefront sensing and wavefront correction.

2.4.2. Wavefront sensing

In order to be able to correct an optical signal, the first logical step is to measure its quality. Ideally this sensing should be performed in real time, i.e., the sensing period should be lower than the time it takes for aberrations to change (which in some applications can be on the order of milliseconds). In microscopy, two main approaches are taken:

- Direct sensing: A wavefront sensor is used to measure the phase of the wavefront, determining it explicitly.
- Indirect sensing: No wavefront sensor is present. Instead, a figure of merit related to the magnitude of the aberrations (such as image sharpness) is used to compensate the wavefront.

Direct sensing provides the most accurate and fast corrections, but it is also the most complex and expensive approach. In this section, the physics behind direct wavefront sensing, as well as the most popular sensing device, the Shack-Hartmann wavefront sensor, will be explained.

2.4.2.1. Measuring the wavefront

The phase of a photon cannot be directly measured, and the only relevant information for wavefront sensing that we can extract from an optical signal is its intensity distribution. Hence, the whole problem of measuring the shape of the wavefront boils down to the problem of extracting phase information from intensity.

The wavefront is always continuous over the pupil, but it can be divided into a number N of subapertures. If we can express the phase of each subaperture as a single number, then the wavefront is completely represented by the set of N values. It is evident that a higher number of subapertures provides us with a more precise representation of the wavefront, which would be exact for $N = \infty$. Moreover, each subpupil can provide more than a single value, such as tip and tilt of the wavefront over that region. In fact, the knowledge of tip and tilt over each region can be used to calculate the modal modes of the full aperture.

The Shack-Hartmann wavefront sensor (SHWFS) makes use of this fact to measure the wavefront. It was developed by R. Shack [82], who improved upon a previous device conceived by J. Hartmann.

The SHWFS consists on a microlens array with an imaging sensor located at the focal plane of the microlenses. This way, each microlens creates a spot on the sensor, which has multiple pixels for each spot. By measuring the position of each spot on the sensor, tip and tilt can be calculated for their corresponding subapertures.

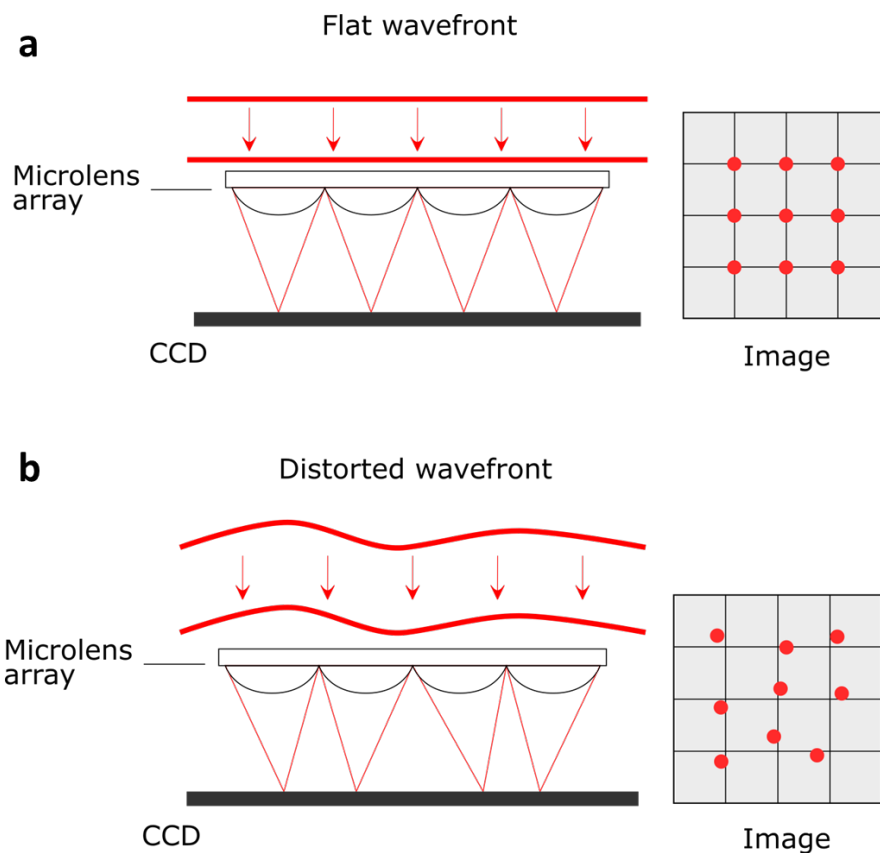


Figure 2-14: Working of a SHWFS. (a) An undistorted wavefront creates a regular array of spots on the imaging chip. (b) When the wavefront is aberrated, the focused spots are distributed in an irregular way. The displacement of each spot determines the slope of wavefront along the corresponding subaperture.

Calculating the spot centroid

The first step to calculate tilt is to locate the centroid of the Shack-Hartmann spot. Let us consider the spot produced by a subaperture of a SHWFS of size d . The spot has an intensity distribution $P(x, y)$ over a region of $W_p \times W_p$ pixels, which can be discretized as an array of the pixel intensity values $I_{i,j}$. The centroid of $P(x, y)$ is located at (x_0, y_0) .

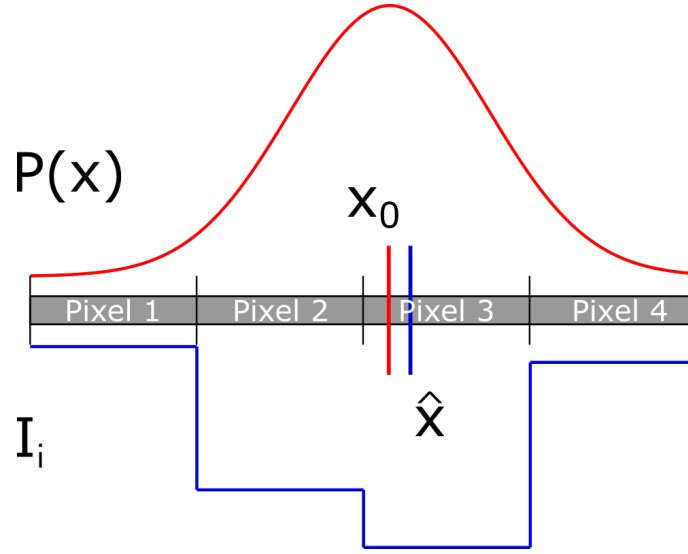


Figure 2-15: Intensity distribution $P(x)$ over a linear array of pixels. The actual distribution is presented in red, while the measured one, I_i , is presented in blue. The actual and calculated centroids are designated by x_0 and \hat{x} , respectively.

Let λ be the wavelength of the incoming wavefront. The parameter $N_{samp} = (\lambda/d)/p$ compares the half-width of the diffraction-limited spot to the pixel angular size. The Nyquist sampling criterion is satisfied when $N_{samp} \geq 2$.

A noise-free, diffraction-limited spot will take the form of a Gaussian function:

$$P(x, y) = \frac{N_{ph}}{2\pi\sigma^2} \exp\left[-\frac{(x - x_0)^2 + (y - y_0)^2}{2\sigma^2}\right], \quad (2-39)$$

where N_{ph} is the total number of photons arriving at the sensor and σ^2 is the variance of the intensity distribution. The FWHM of the spot is given by $FWHM = 2\sqrt{2\ln 2}\sigma = 2.3548\sigma$ [83].

Perhaps the simplest method to calculate the centroid of the spot is the Centre of Gravity (CoG) method. If we denote the calculated centroid by (\hat{x}, \hat{y}) and the pixel coordinates by (x', y') :

$$\hat{x} = \frac{\sum x' I_{x',y'}}{\sum I_{x',y'}}, \quad \hat{y} = \frac{\sum y' I_{x',y'}}{\sum I_{x',y'}}. \quad (2-40)$$

This method is useful in near-ideal conditions, but it is imprecise in the presence of noise. It can be improved by thresholding so that the noise is filtered away. Let I_T be the threshold pixel intensity. The calculated centroid becomes:

$$\hat{x} = \frac{\sum_{I>I_T} x' (I_{x',y'} - I_T)}{\sum_{I>I_T} (I_{x',y'} - I_T)}, \quad \hat{y} = \frac{\sum_{I>I_T} y' (I_{x',y'} - I_T)}{\sum_{I>I_T} (I_{x',y'} - I_T)}. \quad (2-41)$$

This is a more precise result, but still doesn't completely resolve the noise problem. Indeed, in the presence of high noise, a sizeable part of the signal will rest in pixels that fall under the threshold and it will be ignored. Instead, weights can be used so that the contribution of noisy pixels is attenuated as opposed to completely eliminated. Let $w_{x',y'}$ be the discrete weight function. The calculated centroid coordinates are:

$$\hat{x} = \gamma_x \frac{\sum x' I_{x',y'} w_{x',y'}}{\sum I_{x',y'} w_{x',y'}}, \quad \hat{y} = \gamma_y \frac{\sum y' I_{x',y'} w_{x',y'}}{\sum I_{x',y'} w_{x',y'}}. \quad (2-42)$$

where γ_i are normalization coefficients. There exist different approaches for the choice of the function $w_{x',y'}$, a comparison between them was performed by Thomas et al. [83].

Spot centroid can also be calculated by a correlation algorithm. This is especially useful for use with extended light sources as their arbitrary shape may hinder centroid calculation by CoG-based methods. A correlation algorithm uses the cross-correlation function $C(x, y)$ between the spot image I and a template F :

$$C(x, y) = I \otimes F = \sum_{x',y'} I_{x',y'} F(x' + x, y' + y). \quad (2-43)$$

The spot centroid can be calculated by maximizing $\mathcal{C}(x, y)$, which has arbitrarily high resolution. The template F may be an analytical function, the spot of some subaperture or some function of the spots. The correlation method is especially robust against noise, but it is computationally slower than CoG-based methods.

Once the spot is properly located, information about the wavefront can be acquired from its position.

Calculating the slopes

A SHWFS reconstructs the wavefront in a zonal fashion, calculating its two-dimensional slope in each subpupil from the position of the corresponding spot. Let (x, y) be the centroid of a spot, and let (x^*, y^*) be the position of the same spot in the case of a flat, unaberrated wavefront. $\Delta x = x - x^*$ is then the displacement of the spot in the x direction due to aberrations. This displacement is related to the local slope of the wavefront, $\tan \theta_x$, by:

$$s^x = \tan \theta_x = \frac{\Delta x}{f}, \quad (2-44)$$

where s^x is the average slope of the wavefront in the x direction over the subaperture and f is the focal distance of the microlens (Figure 2-16). In terms of the phase $\Phi(\mathbf{r})$:

$$\int_{subaperture} \frac{\partial \Phi(\mathbf{r})}{\partial x} d\mathbf{r} = \frac{2\pi A \Delta x}{\lambda f}, \quad (2-45)$$

where A is the area of the subaperture. This way we calculate a set of slopes $s_i^{x_j}$ (where $\{x_j\} = \{x, y\}$) that can be used to reconstruct the wavefront.

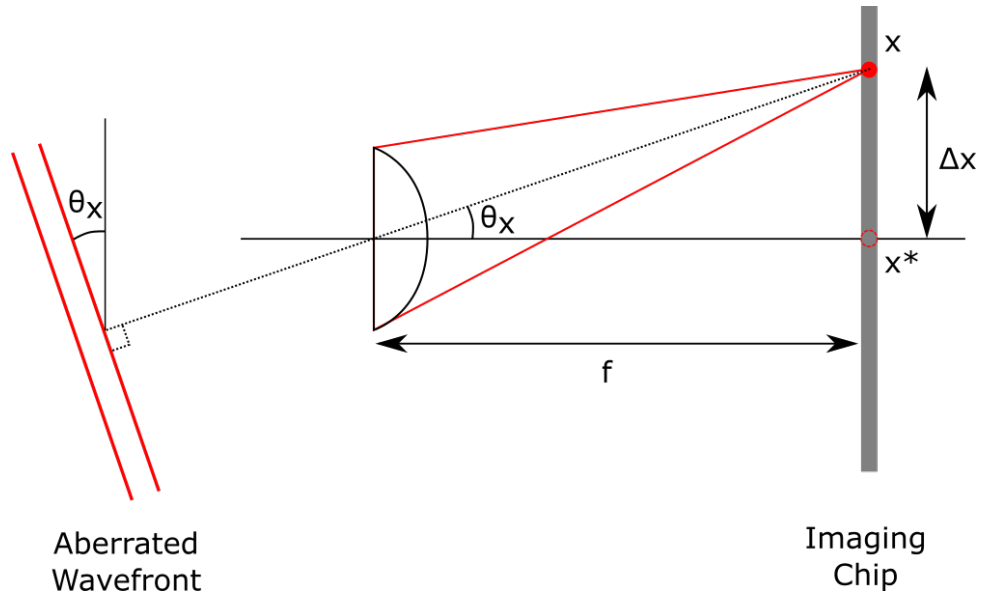


Figure 2-16: Calculation of wavefront slope over a subaperture from the displacement of the Shack-Hartmann spot.

Reconstructing the wavefront

Each of the slopes is related to the phase at the ends of each aperture. For example, using the notation in Figure 2-17 (a):

$$\begin{aligned} s_1^x &= \phi_{-1,1} - \phi_{0,1} \quad , \\ s_1^y &= \phi_{-1,1} - \phi_{-1,0} \quad . \end{aligned} \tag{2-46}$$

Written in matrix form:

$$\mathbf{s} = \mathbf{B}\boldsymbol{\phi}, \tag{2-47}$$

where \mathbf{s} is the slopes vector, $\boldsymbol{\phi}$ is the phase vector and \mathbf{B} is the geometry or wavefront sensor interaction matrix. Hence, the wavefront phase can easily be calculated using the Moore-Penrose pseudoinverse of \mathbf{B} :

$$\boldsymbol{\phi} = (\mathbf{B}^T \mathbf{B})^{-1} \mathbf{B}^T \mathbf{s}. \tag{2-48}$$

The geometry matrix \mathbf{B} depends on the spatial disposition and relations between nodes. If there are N subapertures, $\boldsymbol{\phi}$ has dimension N , while \mathbf{s} has a dimension M that depends on the geometry of the sensor. Hence, \mathbf{B} has dimension $N \times M$. Hudgin and Fried geometries, two common configurations in SHWFS, are shown in Figure 2-17.

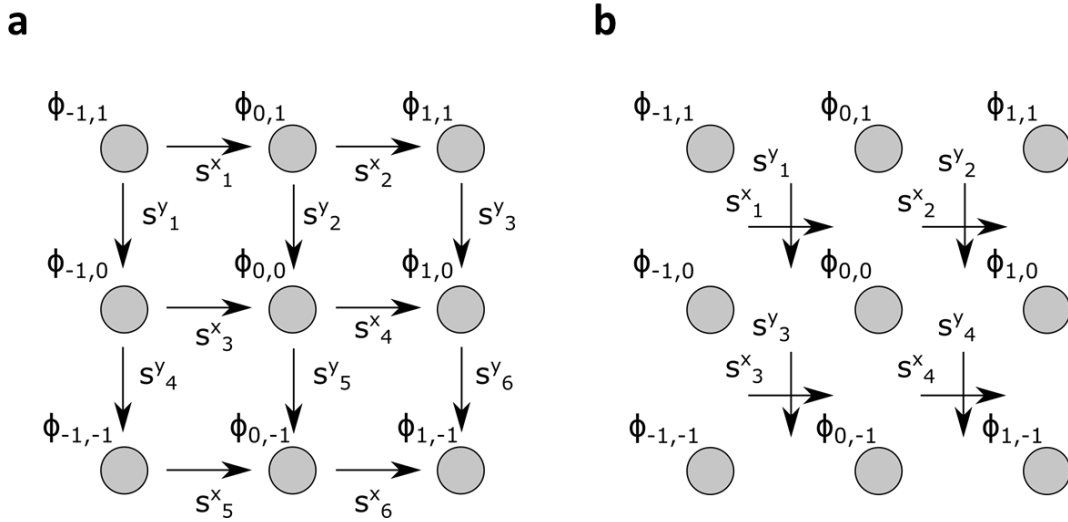


Figure 2-17: Comparison between (a) Hudgin and (b) Fried geometries. Hudgin geometry takes into account the slopes between spots, while in Fried geometry the slopes are considered from the middle of the segments joining the spots.

Calculating the Zernike modes

As seen in section 2.1.5.1, the wavefront can be exactly represented as a linear combination of Zernike polynomials. According to (2-27):

$$\Phi(x, y) = \sum_{n=0}^{\infty} \sum_{m=-n}^n A_{nm} Z_n^m(x, y), \quad (2-49)$$

Where $\Phi(\rho, \theta)$ is the phase of the signal, $Z_n^m(\rho, \theta)$ are the Zernike polynomials and A_{nm} are the Zernike coefficients. The vector $\boldsymbol{\phi}$ is a discrete representation of $\Phi(\rho, \theta)$. Our interest now is to calculate the coefficients A_{nm} from the vector $\boldsymbol{\phi}$. For simplicity and ease of reading, we will denote the polynomials and their coefficients with a

single index k . If we want to calculate the first K modes and neglect higher order aberration:

$$\Phi(x, y) = \sum_k^K A_k Z_k(x, y). \quad (2-50)$$

The slopes s_m^{xj} of each aperture m can then be expressed as:

$$s_m^x = \left. \frac{\partial \Phi}{\partial x} \right|_m = \sum_k^K A_k \left. \frac{\partial Z_k(x, y)}{\partial x} \right|_m,$$

$$s_m^y = \left. \frac{\partial \Phi}{\partial y} \right|_m = \sum_k^K A_k \left. \frac{\partial Z_k(x, y)}{\partial y} \right|_m, \quad (2-51)$$

where the subscript m denotes evaluation at the coordinates (x_m, y_m) . This can be expressed as a matrix equation:

$$\mathbf{s} = \mathbf{Z}\mathbf{A}, \quad (2-52)$$

where \mathbf{s} is the slopes vector and \mathbf{A} is the coefficients vector. Supposing that half of the measurements are slopes in the x direction and half are in the y directions, the vectors \mathbf{s} and \mathbf{A} are:

$$\mathbf{s} = \begin{pmatrix} \left. \frac{\partial \Phi}{\partial x} \right|_1 \\ \vdots \\ \left. \frac{\partial \Phi}{\partial x} \right|_{\frac{M}{2}} \\ \left. \frac{\partial \Phi}{\partial y} \right|_1 \\ \vdots \\ \left. \frac{\partial \Phi}{\partial y} \right|_{\frac{M}{2}} \end{pmatrix}, \quad \mathbf{A} = \begin{pmatrix} A_1 \\ A_2 \\ \vdots \\ A_3 \end{pmatrix}, \quad (2-53)$$

while the matrix \mathbf{Z} takes the form:

$$\mathbf{Z} = \begin{pmatrix} \left. \frac{\partial Z_1(x, y)}{\partial x} \right|_1 & \left. \frac{\partial Z_2(x, y)}{\partial x} \right|_1 & \dots & \left. \frac{\partial Z_K(x, y)}{\partial x} \right|_1 \\ \vdots & \vdots & & \vdots \\ \left. \frac{\partial Z_1(x, y)}{\partial x} \right|_{\frac{M}{2}} & \left. \frac{\partial Z_2(x, y)}{\partial x} \right|_{\frac{M}{2}} & \dots & \left. \frac{\partial Z_K(x, y)}{\partial x} \right|_{\frac{M}{2}} \\ \left. \frac{\partial Z_1(x, y)}{\partial y} \right|_1 & \left. \frac{\partial Z_2(x, y)}{\partial y} \right|_1 & \dots & \left. \frac{\partial Z_K(x, y)}{\partial y} \right|_1 \\ \vdots & \vdots & & \vdots \\ \left. \frac{\partial Z_1(x, y)}{\partial y} \right|_{\frac{M}{2}} & \left. \frac{\partial Z_2(x, y)}{\partial y} \right|_{\frac{M}{2}} & \dots & \left. \frac{\partial Z_K(x, y)}{\partial y} \right|_{\frac{M}{2}} \end{pmatrix}. \quad (2-54)$$

As before, the coefficient vector \mathbf{A} can be calculated as:

$$\mathbf{A} = (\mathbf{Z}^T \mathbf{Z})^{-1} \mathbf{Z}^T \mathbf{s}. \quad (2-55)$$

However, since a finite set of Zernike polynomials over a discrete pupil are neither complete nor orthogonal, the reconstruction will differ from the actual wavefront by an RMS error ϵ , which depends on the number of samples and the geometry of the

sensor [84], [85]. The presence of noise hinders centroid calculation of the Shack-Hartmann spots and will further increase the error as a function of the SNR.

In addition, subsampling is an issue to take into account. If the sampling density of the slopes is not enough for the number of modes required, higher order modes will appear as perturbations on the lower order modes, leading to a higher ϵ .

2.4.2.2. The guide star

Wavefront sensing usually involves the use of a point-like source of light called the “guide star”, recalling the origins of AO in the astronomy field. Although extended sources of light can be used for wavefront measurement, they severely compromise contrast (due to overlapping images) and present complex relationships between wavefront sensor signal and wavefront shape [86], [87].

Guide stars are useful because the wavefront from a point source of light is easy to model, and point-like Shack-Hartmann spots allows us to accurately calculate the wavefront slopes. They are therefore used in almost every wavefront sensor AO scheme.

Unlike the sky, biological tissue doesn't present naturally occurring guide stars. A number of approaches for guide star placing inside tissue have been tried over the last decade. Perhaps the most straightforward of them is the placement of fluorescent beads inside the sample. Beads can be arbitrarily small, are commercially available in a wide variety of spectrums, and usually produce a large amount of fluorescence. The beads can be inserted into the tissue either by microinjection [88] or by adsorption during tissue development [23]. However, these methods either are intrusive or yield random bead placement, limiting the available regions in which corrections can be performed. Moreover, the possibility of beads interfering with cell physiology must be considered. Either a pinhole or single-bead excitation is required to isolate a single guide star.

A less intrusive approach is the use of small fluorescent structures expressed by the cells, such as the centrosome [89]. This approach has the advantage of a more uniform coverage of the tissue by guide stars (depending on the structure of choice), as well as a simpler sample preparation. However, the fluorescence yield of such guide stars is limited, and, more importantly, tracking small structures in live samples in order to isolate a single guide star can be a challenge.

This issue can be solved by the use of a laser guide star. By focusing a laser into larger fluorescent structures, we can generate a single guide star with a limited lateral size [90]. Nonetheless, the axial length of the guide star depends on the axial of the structure, limiting its use to thin structures.

Two-photon excitation (TPE) provides a mechanism by which a laser guide star can be localized in the axial direction. TPE requires the capture of two photons at the same time by a fluorophore, emitting a higher energy photon. Since the probability of this happening is extremely low, it will only occur in high photon density regions. By focusing a femtosecond laser into a fluorescent structure, TPE can be achieved in a small spherical region close to the focus, thus providing a non-linear guide star (NGS) [72]. NGS can be placed at will in the FOV, don't depend on the size of the labelled structure and, since the excitation wavelength is in the IR, are less distorted than guide stars produced by visible lasers. They provide a non-invasive and versatile method for wavefront measurement in biological samples and are arguably the best guide star alternative for live imaging. The main drawback of NGS is their low fluorescence yield, requiring the use of accordingly sensitive sensors.

2.4.3. Wavefront correction

Wavefront correction is, in essence, the process of distorting the wavefront to improve the performance of the system, either by removing or by adding aberration.

Hence, many of the mechanisms that cause wavefront distortion can be used to correct it. The physical process by which the wavefront is corrected and the most important correction devices will be presented in this section.

2.4.3.1. Phase conjugation

The principle behind every AO system is the phase conjugation. Let us consider a distorted wavefront. When this wavefront is reflected in a flat mirror, it preserves its shape while propagating in the opposite direction. But, if the mirror is not flat, the shape of the wavefront will be modified by that of the mirror.

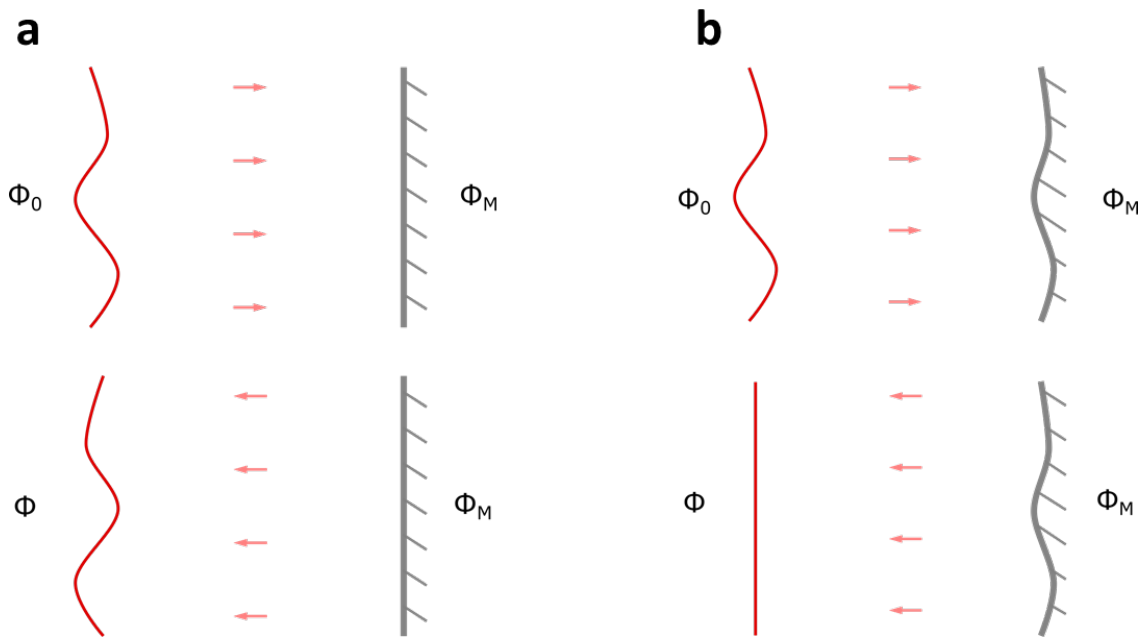


Figure 2-18: Wavefront correction by phase conjugation. (a) A distorted wavefront is reflected by a flat mirror, preserving its shape. (b) The same wavefront is reflected by a mirror of shape $\Phi_M = \Phi_0/2$, producing a flat wavefront.

Indeed, it is easy to see that if $\Phi_0(\rho, \theta)$ is the phase of the incoming wavefront and $\Phi_M(\rho, \theta)$ is the shape of the deformable mirror, the phase $\Phi(\rho, \theta)$ of the reflected wavefront is given by:

$$\Phi(\rho, \theta) = \Phi_0(\rho, \theta) - 2\Phi_M(\rho, \theta). \quad (2-56)$$

So, by applying a mirror shape $\Phi_M = \Phi_0/2$, we obtain a flat wavefront:

$$\Phi(\rho, \theta) = 0. \quad (2-57)$$

2.4.3.2. AO loop

Usually, AO systems work continuously in an iterative fashion (called a loop) either to keep up with changing aberrations or to optimize correction through several passes. Based on the presence or not of feedback, a distinction is made between open and closed loops.

In an open-loop system, the figure of merit (RMS aberration, intensity, image sharpness...) is measured before the correction is performed, in such a way that there is no feedback about the effect of the correction. Sensor-less AO systems often run in open-loop mode.

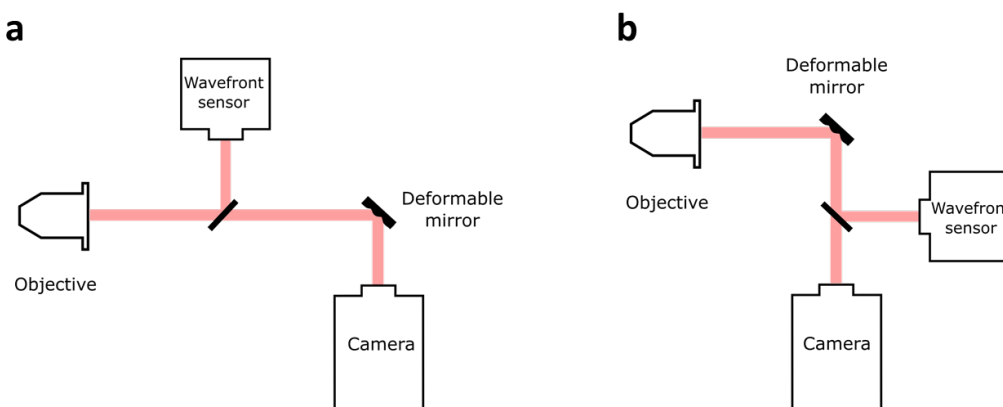


Figure 2-19: Example of (a) open loop configuration and (b) closed loop configuration. In an open loop, the wavefront is measured before the correcting device, while, in the closed loop, it is measured after it.

Closed-loop systems measure the figure of merit after the wavefront has been shaped by a correction device, providing feedback about the quality of the correction.

This way, errors in wavefront shaping can be corrected in subsequent iterations. Closed-loop operation is the norm in wavefront sensor systems.

2.4.3.3. Correction devices

Any instrument able to shape the wavefront of the light can be used as a correction device. Segmented and deformable mirrors are the most popular of such instruments in imaging systems. Due to the impracticality of large deformable mirrors, segmented mirrors most popular in large telescopes, whereas in microscopy deformable mirrors are predominant. A brief description of these devices is presented below.

Segmented Mirrors

The segmented mirror is a device made from a matrix of smaller mirrors with piston or tilt (on one or two axes) capability. Each of the submirrors is placed on top of an actuator that can move it up and down and, in some implementations, tip or tilt it. Submirror shape is a relevant parameter [91], and square, hexagonal and circular mirrors have been used. Segmented mirrors are easily scalable, some mirrors having hundreds or thousands of segments [3], [92].

A notorious drawback of segmented mirrors is the presence of discontinuities between the segments. These gaps produce two main optical effects: a loss of energy through the gaps and a diffraction of energy from the central lobe of the diffraction pattern. Both of these effects are proportional to the ratio of gap to segment area. For gap area less than 2% the impact of the gaps on overall performance are minor [93].

As each segment is operated independently, there is no cross-coupling between them. However, cross-coupling can be introduced in order to increase bandwidth. Segmented mirrors with a bandwidth as high as 5 kHz have been reported [94].

Deformable Mirrors

Deformable mirrors (DM) consist on a continuous reflective surface equipped with some mean of deformation. In microscopy DMs are usually the tool of choice due to their achromaticity, high reflectivity and, most importantly, speed. Many kinds of DMs have been prototyped over the last 50 years, and, thanks to Micro-Electro-Mechanical Systems (MEMS) technology, several models of DMs are now being mass-produced at relatively inexpensive costs. The most commonly used are, depending of on their actuation mechanism:

Electrostatic mirrors

A thin ($0.5\ \mu\text{m}$ to $1\ \mu\text{m}$) conductive membrane acts as the reflecting element of the mirror. It can be deformed by electrostatic forces by means of applying voltage differences between the membrane and the electrode actuators. These forces can only be attractive, so only pull movement is allowed. Movement in the upward direction can be enabled by placing an additional set of transparent actuators above the membrane [95], [96].

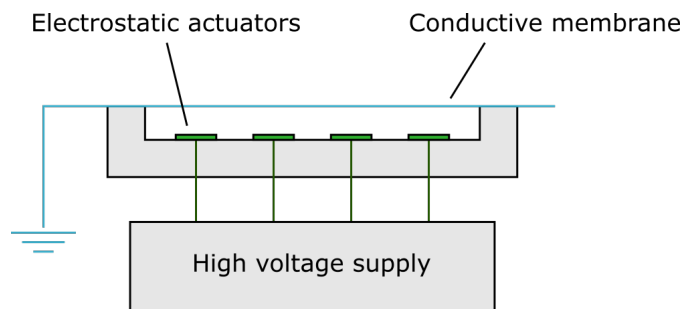


Figure 2-20: Electrostatic deformable mirror.

Damping can be reduced by placing the membrane in a partial vacuum, though the presence of some damping has been found necessary in large-stroke systems to avoid pinning the membrane to the electrodes [3]. This kind of mirrors present no hysteresis.

Electromagnetic mirrors

In this case, the reflective membrane has small magnets at the back of the reflective surface. The membrane can be deformed using voice coil (solenoid) actuators, which are used to both push and pull each magnet. They provide a very fast response time, present no hysteresis, and require low voltages to operate [97], making them particularly popular for small mirrors, although there exist large ones as well [98]. The Mirao 52-e DM used in our system belongs to this category.

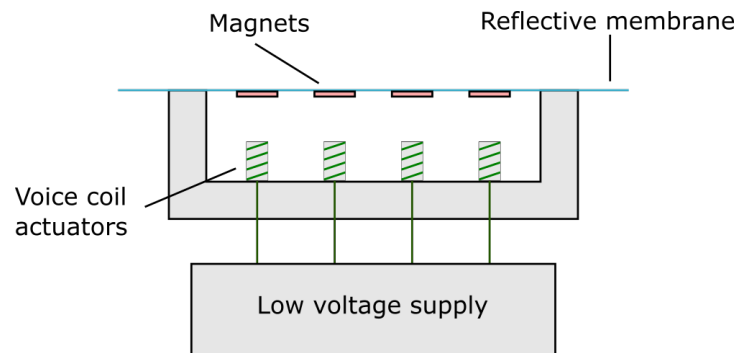


Figure 2-21: Electromagnetic deformable mirror.

Piezoelectric mirrors

A piezoelectric mirror consists on a glass or metal plate firmly attached to a continuous piezoelectric material wafer (unimorph mirror) or two piezoelectric wafers attached together (bimorph mirror). In an unimorph mirror the glass sheet is polished and coated to become the reflecting part of the DM, while on a bimorph mirror one of the piezoelectric wafers may be used as the reflective element [99]. The piezoelectric wafers are polarized normal to their surface. Electrodes concentrically placed on the back of the piezoelectric sheets are used to deform them.

Bimorph mirrors permit the decoupling of low-order and high-order aberration correction, allowing better correcting of low-order aberrations by allocating a larger stroke budget to them.

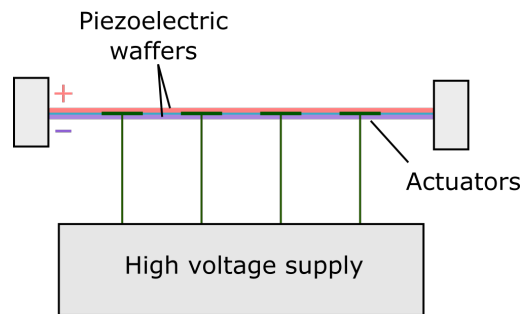


Figure 2-22: Bimorph piezoelectric wafer deformable mirror.

The use of piezoelectric materials leads to the presence of hysteresis, which limits the bandwidth. Depending on the piezoelectric material, high voltages (upwards of 1000V) may be required to drive the mirror, requiring extra support equipment [3]. Piezoelectric mirrors typically have a low number of actuators (a few dozens) compared to electrostatic or electromagnetic mirrors that can have up to thousands of actuators.

Chapter 3

SYSTEM IMPLEMENTATION AND CHARACTERIZATION

3.1. Introduction

SPIM is one of the most popular tools for in-depth imaging of large samples. Its ability to provide subcellular resolution over hundreds of microns, fast acquisition speeds and low photobleaching have made it an essential instrument for live imaging. However, absorption, scattering and aberrations can severely limit its in-depth imaging capability. By using AO, aberrations can be corrected and image quality, as well as imaging depth, can be improved.

Sensor-based AO approaches require the use of guide stars which are not naturally present in organisms and have to be artificially generated, for example, by using beads or labelling small structures inside the sample. However, the process of introducing these guide stars in the sample is often intrusive and yields randomly

located guide stars. The non-linear guide star is an interesting approach to this problem. A non-linear guide star is generated by means of two-photon excitation. It is a non-intrusive method that can place a guide star anywhere on the focal plane of the microscope. Still, depending on the sample NGLs can be notably faint.

We have developed a system, the Wavefront sensor Adaptive Optics SPIM (wAO SPIM) with the objective of improving imaging quality at depth. It is based on a conventional SPIM setup in which an AO subsystem has been implemented, as well as an NIR illumination arm for NGL generation.

Our wAO SPIM makes use of a custom-made high-sensitivity SHWFS made by Imagine Optic in order to be able to work with very faint guide stars when reading the wavefront.

A detailed description of the system and high-sensitivity SHWFS, as well as a characterization of its correction capability, will be provided in this chapter.

3.2. Description of the system

3.2.1. General view

wAO SPIM consists of three main optical paths:

- **Visible illumination path:** A visible laser beam (491, 532 or 595 nm) is focused into a light sheet by a cylindrical lens for SPIM illumination. A 900 nm laser is swapped in for IR illumination.
- **Two-photon illumination path:** A 780 nm femtosecond laser is directed by a pair of galvanometric mirrors and focused into the sample for NGL generation.

3.2. DESCRIPTION OF THE SYSTEM

- **Detection path:** Light is collected, corrected and split into two sub-paths. The shorter wavelengths reach the SHWFS while the longer ones reach a dual wavelength imaging camera.

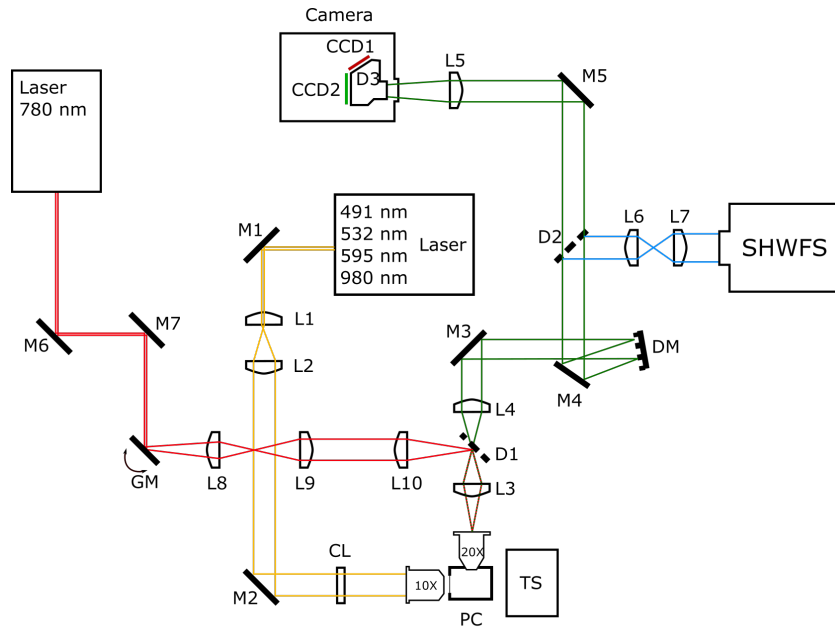


Figure 3-1: Schematic image of WAO SPIM (not to scale). L1–10: Lenses; M1–7: Mirrors; D1–3: Dichroic beamsplitters; CL: Cylindrical lens; DM: Deformable mirror; SHWFS: Shack–Hartmann wavefront sensor; GM: Pair of galvanometer mirrors; PC: Physiological chamber; TS: Translation stage.

The lateral resolution of the microscope is $0.64 \mu\text{m}$. The axial resolution depends on the light sheet thickness, and is around $2 \mu\text{m}$, depending on the illumination wavelength. A detailed account of the optical elements of the system is provided in Appendix 1.

3.2.1.1. Visible illumination path

An Errol compact laser launch generates the laser lines of 491, 532 and 595 nm which are then coaxially merged. An acousto-optic tuneable filter permits precise control over the intensity of each beam.

The output beam is collimated and expanded by a telescope. A cylindrical lens generates the light sheet, which is focused into the sample by a 10x, 0.25 NA air objective (Leica Microsystems).

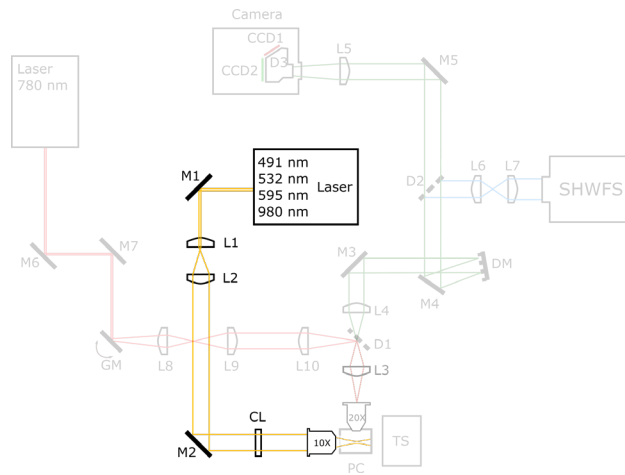


Figure 3-2: Detail of the illumination path.

For experiments requiring NIR illumination, a 980 nm continuous laser was used instead. In these cases, lenses L1 and L2 were replaced by lenses of similar focal distance but coated for operation in the infrared.

The waist thickness and Rayleigh range of the Gaussian light sheet is provided in Table 3-1.

3.2. DESCRIPTION OF THE SYSTEM

Table 3-1: Waist thickness and Rayleigh range of the light sheet for all the possible illumination modes.

λ	w_0 (μm)	z_R (μm)
491 nm	0.83	4.41
532 nm	0.90	4.78
595 nm	1.01	5.29
980 nm	1.66	8.80

3.2.1.2. Two-photon illumination path

A 780 nm femtosecond laser (Toptica Photonics) is directed by a pair of galvanometric mirrors to the sample. A 20x, 0.5 NA water immersion objective (Leica Microsystems), shared with the detection path, is used to focus the beam into the sample. The pair of galvanometric mirrors is conjugated with the back-pupil plane of the objective. A short-pass dichroic mirror (Semrock, <746/9 nm pass) is used to introduce the NIR beam into the detection path.

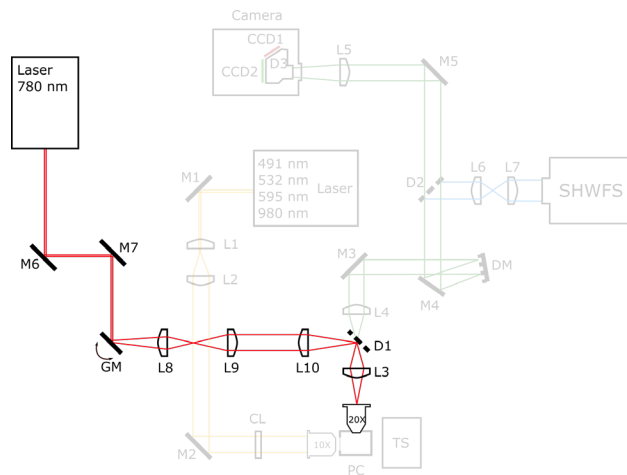


Figure 3-3: Detail of the two-photon excitation arm.

3.2.1.3. Detection path

Fluorescence light is collected by a 20x, 0.5 NA water immersion objective and expanded by a telescope. The back-pupil plane of the telescope is conjugated with a Mirao 52-e electromagnetic DM (Imagine Optic). A long-pass dichroic beamsplitter (Semrock, >520/8 nm pass) directs the 350-512 nm wavelengths to the SHWFS, while allowing the 528-750 nm wavelengths to reach the ORCA-D2 dual imaging camera (Hamamatsu Photonics). The ORCA-D2 permits simultaneous imaging in the 641 (CCD1) and 520 nm (CCD2) wavelengths.

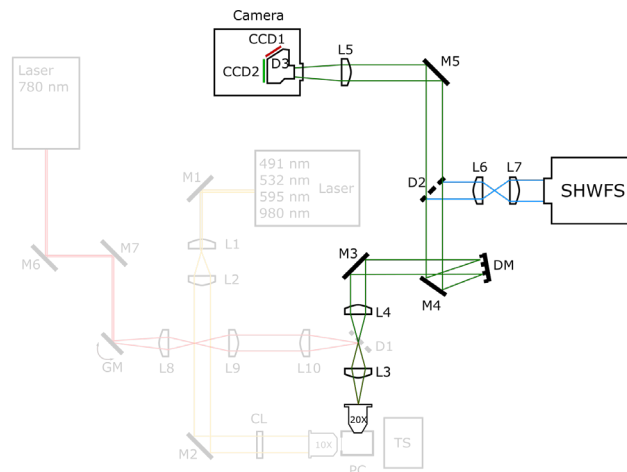


Figure 3-4: Detail of the detection path.

3.2.1.4. Sample mounting

The sample is embedded in an agarose cylinder that is polymerized inside a glass capillary. This capillary is immersed in an aqueous solution while hanging from a translation stage that allows sub-micron three-dimensional displacement of the sample. The agarose cylinder is pushed out from the glass capillary and exposed prior to observation.

3.2. DESCRIPTION OF THE SYSTEM

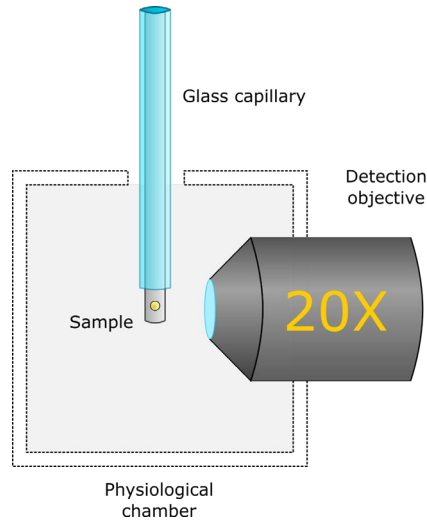


Figure 3-5: Mounting scheme of our system.

3.2.1.5. Electronic control

The main control software of `WAOSPIIM` is the house-made `AMISPIIM` software based on `LavView`. The AO system was driven by the `WaveSuite` software (Imagine Optic) while galvanometer mirrors driving the NGS were controlled by the `iLas` software (Roper Scientific).

3.2.2. The non-linear guide star

The NGS is generated by means of two-photon excitation. A focused 780 nm femtosecond pulsed laser excites a fluorophore (GFP or fluorescein in our case) that only emits light in a small region around the focus. This region is small enough to be used as a guide star for wavefront measurements. A full characterization of the NGS used in our system, outside and inside TMs, is provided in this section.

In order to decouple NGS shape from the TM's fluorophore spatial distribution, unlabelled MCTS were used. The MCTS were immersed in a fluorescein solution for an hour before imaging. Fluorescein is a soluble fluorophore with peak emission

around 520 nm that easily permeates MCTS and distributes uniformly within them, permitting reliable NGS generation inside and outside MCTS.

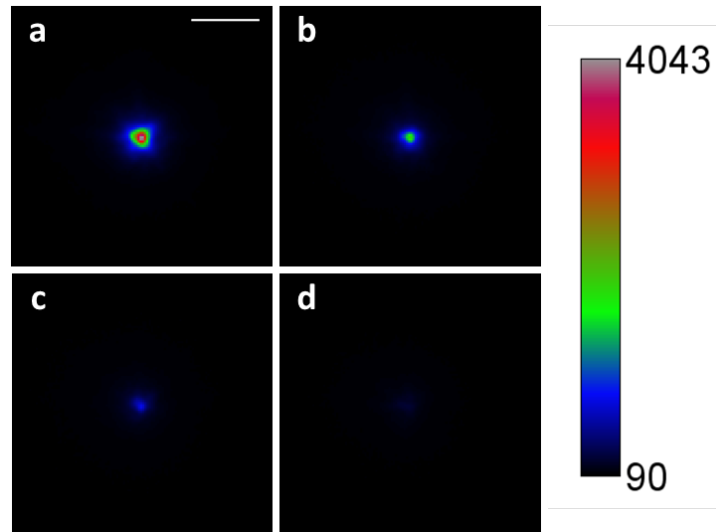


Figure 3-6: Guide star observed at different depths within an MCTS. The MCTS was immersed in a fluorescein solution and the NGS imaged after 1h. (a) NGS outside spheroid. (b) Depth: 25 μm . (c) Depth: 50 μm . (d) Depth: 75 μm . Scale bar: 10 μm .

The lack of ability of our microscope to move the guide star in the z direction prevented us from assessing the axial FWHM. The guide star had a lateral diameter of around 2.2 μm (FWHM) in agarose. In order to be considered as a point source, the guide star has to be below the diffraction limit of the wavefront sensor. In our case, for a 520 nm wavelength, this limit is 8.62 μm , so the NGS is a suitable point emitter for wavefront reading.

3.2. DESCRIPTION OF THE SYSTEM

Table 3-2: Observed lateral FWHM of the NGS at different depths inside the MCTS.

Depth (μm)	FWHM _x (μm)	FWHM _y (μm)
0	2.2	2.2
25	2.4	2.1
50	2.4	2.3
75	4.7	4.9
100	8.7	7.9

As expected, the observed quality of the NGS decreased with depth. The maximum observed intensity suffered an exponential decline inside the MCTS, while the lateral FWHM usually increased after 50 μm , with a fast broadening typically occurring around the 70 nm mark. Deterioration from scattering in both the illumination and detection paths made the NGS typically unusable for wavefront reading after 90-100 μm .

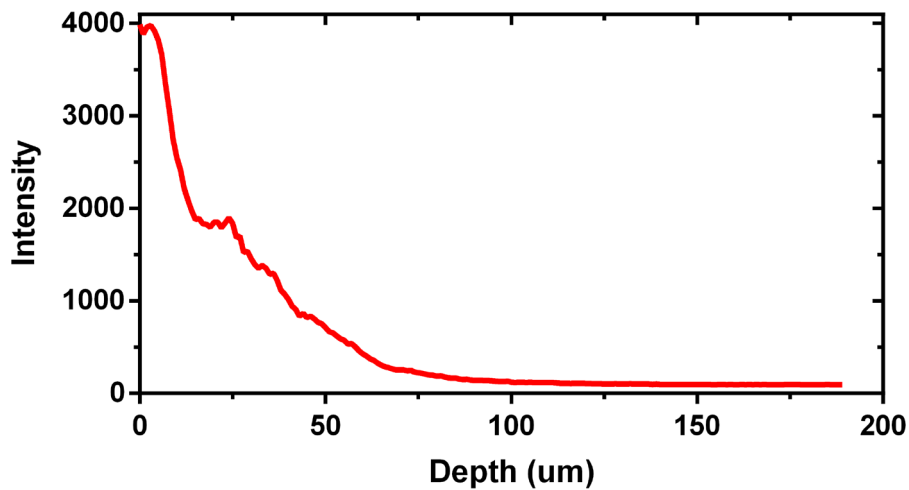


Figure 3-7: NGS observed maximum intensity as a function of depth inside an MCTS.

3.2.3. High-sensitivity Shack-Hartmann wavefront sensor

As stated before, our setup requires the use of an especially sensitive SHWFS. Imagine Optic (Orsay, France) prototyped such a sensor with feedback from our team which it was implemented in the $W_{AO}SPIM$ system. Our SHWFS is based on a Photometrics Evolve 512 EMCCD camera. EMCCD (electron-multiplying charge-coupled device) sensors are some of the most sensitive available, with a quantum efficiency over 0.9 in the visible range. Their electromagnetic gain can be tuned in real time, allowing a trade-off between exposure time and signal-to-noise ratio. These characteristics make EMCCD a powerful and versatile tool when working with a low photon budget, and the logical choice for a high-sensitivity wavefront sensor. The Evolve 512 EMCCD has a 1-300 EM gain range.

Wavefront measurement error depends on parameters such as photon flux, noise, number of subapertures and type of sensor (see section 2.4.2). More specifically, centroid calculation error has a strong dependence on both readout and photon noise. Let $\sigma_{\epsilon_{ph}}^2$ and $\sigma_{\epsilon_r}^2$ be the contributions to phase variance of the photon and readout noise, respectively. It can be shown that, for a centre-of-gravity algorithm [83]:

$$\sigma_{\epsilon_{ph}}^2 = \frac{\pi^2}{2 \ln 2} \frac{1}{N_{ph}} \left(\frac{w}{N_{samp}} \right)^2, \quad (3-1)$$

$$\sigma_{\epsilon_r}^2 = \frac{\pi^2}{3} \frac{N_r^2 S^2}{N_{ph}^2 N_{samp}^2}, \quad (3-2)$$

where N_{ph} is the total number of photons detected by the sensor, $N_{samp} = (\lambda/d)/p$ is the ratio of the half-width of the diffraction ration to the pixel angular size, w is the FWHM of the spot in pixels, N_r is the readout noise and S is the total number of pixels used in the CoG calculation.

Amplifying the signal N_{ph} detected by the sensor can reduce the contributions of both photon and readout noise. However, if EM gain is applied to achieve it, the reduced photon and readout noise come at the price of amplifying thermal and clock-

3.2. DESCRIPTION OF THE SYSTEM

induced noise. The optimal solution is to increase the photon flux that reaches the sensor, but that is not always feasible. Hence, a careful balance has to be stricken between amplification of signal and amplification of noise.

A model of wavefront error as a function of photon flux and EM was carried out by Imagine Optic. Their analysis concludes that at least 2×10^5 photons are required for an optimal wavefront measurement. With this amount of photons and an EM gain of 10 or more, the RMS wavefront error is kept below 7 nm. Additionally, using the maximum EM gain of 300 allows us to work with less than 5×10^4 photons while maintaining an error of less than 10 nm.

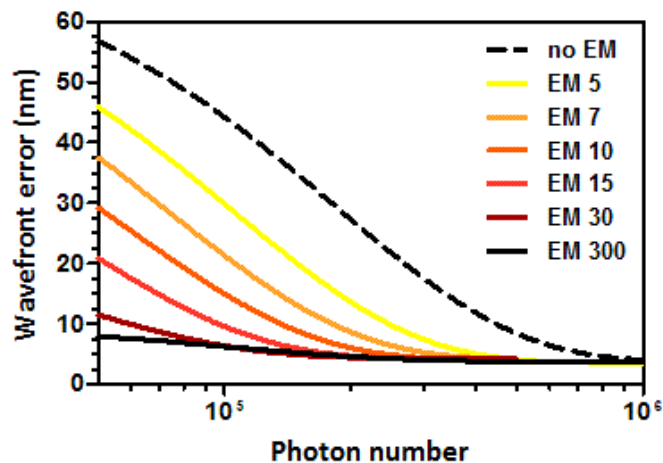


Figure 3-8: Simulated wavefront error as a function of the total number of photons reaching the sensor.

In order to maximize the photon flux per subaperture, the only option is to reduce the number of subpupils so that the photons are less distributed between them. However, the reduced amount of subapertures implies a reduced number of slopes, which will reduce sensor accuracy. Additionally, in a SHWFS there are many other parameters such as microlens focal length, sensor geometry, CCD pixel size, etc.

The design of a wavefront sensor is a complex multiparameter problem that requires a fine tuning of all these parameters to be able to meet the application requirements. In essence, this it is a trade-off between accuracy, sensitivity and dynamic range. In our case sensitivity is a priority, as reflected by the final specifications of the SHWFS.

To help define optimal wavefront sensor design, a simulation (data not shown) of the wavefront measurement dynamic and accuracy as a function of the number of microlenses and photon flux was performed by Imagine Optic. As the objective is to maximize sensitivity, dynamic range was fixed to the minimum required for MCTS imaging.

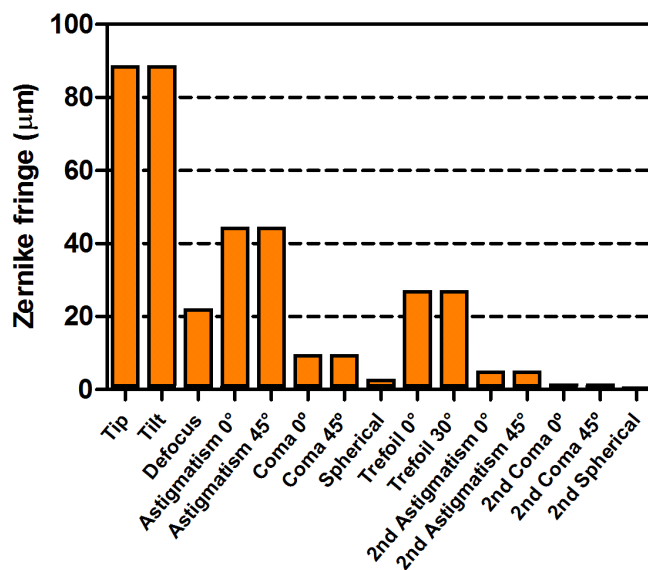


Figure 3-9: Simulated dynamic range of wavefront reconstruction.

In section 2.2, it was discussed how the most significant aberrations in SPIM for MCTS, in minimized refractive index mismatch conditions, are astigmatism, coma, and spherical aberrations. Based on previous experiments carried out by our team, it was evaluated that a 3 μm peak-to-valley dynamic range is necessary on the third-

3.2. DESCRIPTION OF THE SYSTEM

order spherical aberration (Z_4^0) for a 555 nm wavelength in order to sufficiently characterize the aberrations produced by an MCTS.

Table 3-3: Specifications of our Shack-Hartmann wavefront sensor for a 555 nm guide star.

Aperture Dimension (mm²)	7.73×7.73
Number of microlenses	14×14
Microlens step (mm)	0.552
Focus dynamic range (μm)	24.1
Wavefront dynamic on Z_0^4	5.4λ
Photon number for optimal accuracy	200 000
Wavefront measurement accuracy	$\lambda/70$
Working wavelength range (nm)	400–800
Readout speed (MHz)	5
Electron-Multiplying gain	1–300
Diffraction limit (μm)	9.20

The problem then becomes a trade-off between sensitivity and accuracy. Since wavefront correction error is dependent on both the wavefront measurement and wavefront modulation errors, wavefront measurement error must be kept smaller than the modulation error to ensure accurate wavefront correction by the DM. For our Mirao 52-e mirror, this error is no more than 20 nm RMS. This provides a rough approximation of the required wavefront sensing accuracy. It was determined that a 14×14 array of microlenses is able to provide a wavefront reconstruction that meets our accuracy and dynamic range requirements, while maximizing photon flux per subpupil.

3.3. System set-up

The dichroic beamsplitters D1 and D2 introduce a considerable amount of aberration in our system (especially astigmatism and coma). In addition, misalignments between the optical elements of the microscope can also induce a lesser degree of aberration. In order to allow diffraction-limited imaging, these aberrations must be compensated by the AO system. A preliminary system configuration was used with this objective.

Since the main sources of system-induced aberration are the dichroic mirrors, aberrations must be measured after transmission by both of them. The SHWFS was therefore placed after beamsplitter D2 as shown in Figure 3-10.

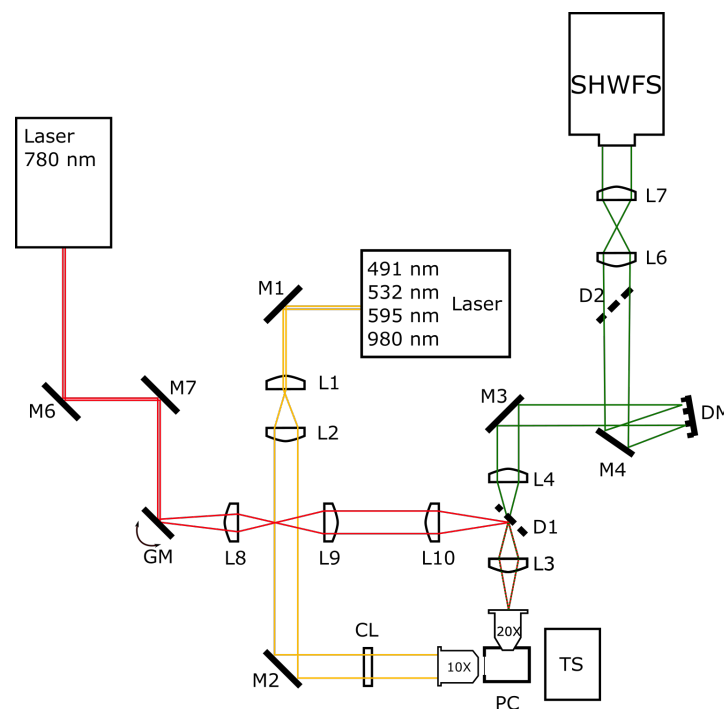


Figure 3-10: Alternative position of the SHWFS used for the correction of system-induced aberrations.

3.3. SYSTEM SET-UP

This way, the wavefront could be measured after passing through most of the system. Although there was still a differential path between the SHWFS and the imaging camera, the wavefront phase difference was considered negligible. The DM was then shaped to generate a flat wavefront in the SHWFS position (Figure 3-11), which was therefore also flat at the imaging camera. This DM shape compensated all system-induced aberration and was used as the default state of the system, denoted as “AO off” from here on.

The SHWFS was then placed in its dedicated path (Figure 3-1). With the DM locked in the “AO off” shape, the SHWFS measured aberrations equal to those produced by the differential path between its current position and its previous one. The measured wavefront was saved and henceforth used as the target wavefront for all AO corrections.

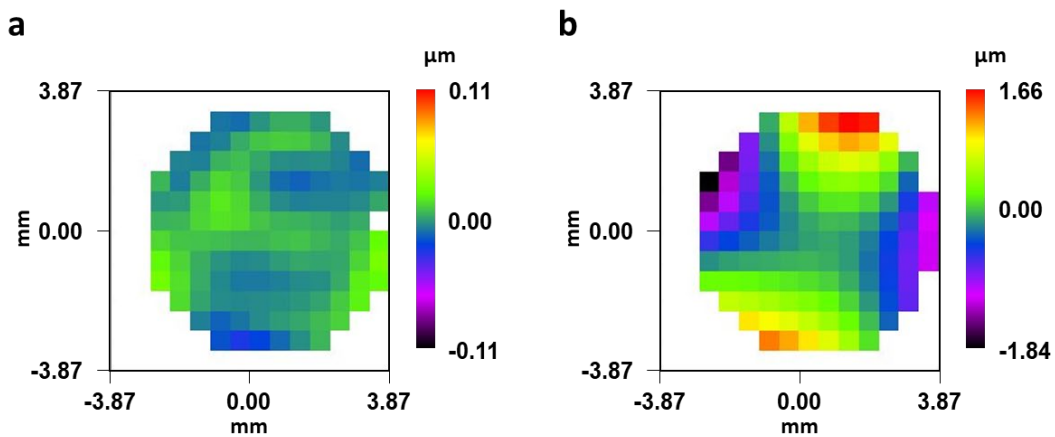


Figure 3-11: Wavefronts measured at the two different SHWFS positions with the mirror in the “AO off” shape. **a)** Preliminary position. **b)** Final position. This wavefront was used as the target for all subsequent corrections.

This process was repeated whenever mechanical drifts of the optical elements of the system (especially in the differential path between the camera and SHWFS) caused the apparition of measurable aberration.

3.4. Adaptive optics performance

The correction capability of $w_{AO}SPIM$ in transparent media was evaluated. For this, we corrected the image of green fluorescent beads using a closed-loop AO. Since our TM imaging imposes the restriction of a limited photon flux, performance was evaluated in both high and low intensity conditions as a function of available light and number of closed-loop iterations. A detailed description of the experiment is presented below.

3.4.1. Methods

In order to evaluate the adaptive optics correction capability of $w_{AO}SPIM$, a set of experiments involving fluorescent beads in transparent media was performed. Green fluorescent beads (InSpeck™ Green, Thermo-Fisher) with a diameter of 2.5 μm and 515 nm emission peak were embedded in a 1% agarose cylinder, which was polymerized inside a glass capillary. The agarose cylinder could be pushed out of the glass capillary at will by a piston.

In a first step, a set of beads were observed in agarose, with the mirror in the “AO off” configuration. The sample was illuminated by a 491 nm light sheet with constant intensity.

A different set of the same kind of beads was then observed inside the glass capillary. The glass capillary acts as a source of aberration, whose main component is astigmatism and, to a lesser extent, trefoil and first order comma. This caused the image to appear distorted in the lateral direction. The wavefront was then corrected using an AO closed loop with a set number of iterations, $N = 15$, and the beads were observed again.

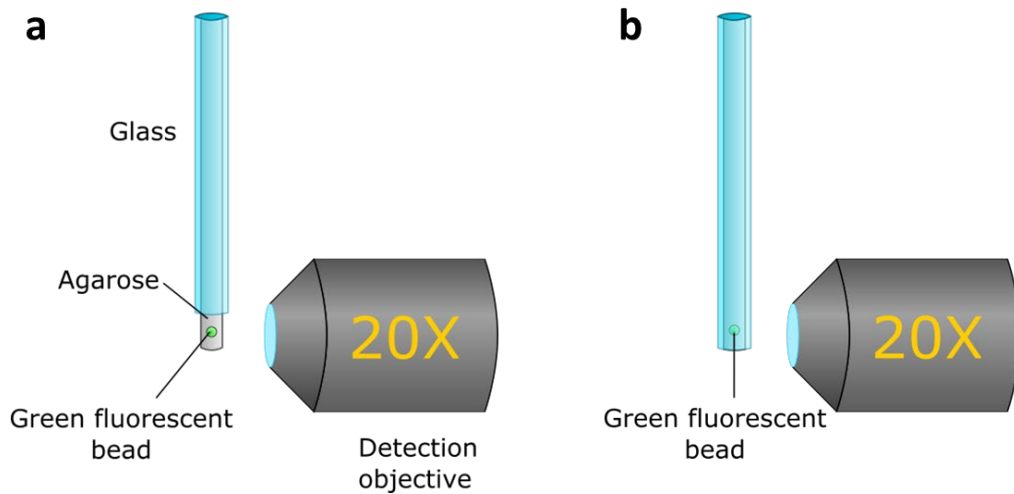


Figure 3-12: Schematic of the experiment. Beads with a diameter of $2.5\ \mu\text{m}$ were observed through (a) agarose and (b) a glass capillary filled with agarose.

For the evaluation of the performance of the AO correction as a function of the number of available photons, a similar number of closed loop iterations, $N = 15$, was used. Performance was also evaluated as a function of the number of closed loop iterations for a fixed photon flux.

The RMS aberrations were calculated from the wavefront slopes and displayed in real time. The Strehl ratio was then calculated using the Maréchal approximation as shown in section 2.1.4.

To evaluate performance as a function of the amount of light, the number of photons reaching the sensor was estimated from the acquired signal and the physical properties of the sensor. The signal $I_t(x, y)$ detected by the sensor has three main sources:

- Signal photons from the guide star that reach the subapertures and are focused into a bright spot.
- Signal photons from the guide star diffracted by the subaperture grid that forms a diffraction pattern between the Shack-Hartmann spots.
- Noise and background signal, $I_b(x, y)$.

$I_t(x, y) = I_{gs}(x, y) + I_b(x, y)$, where $I_{gs}(x, y)$ is the signal coming from the guide star. As our main interest is to determine how much light we need to collect from the guide star to perform an accurate correction, a step to remove background was performed. The background signal distribution $I_b(x, y)$ was determined to be approximately constant over the pupil, and was roughly estimated as equal to the median value of the total intensity distribution $I_t(x, y)$. The number of signal photons N_{ph} was then estimated as:

$$N_{ph} = \frac{I \cdot CG}{EM \cdot QE}, \quad (3-3)$$

where

$$I = \sum I_{gs}(x, y) \quad (3-4)$$

is the sum of the pixel value over the image after removing background, CG is the conversion gain of the sensor, EM is the electron multiplying gain applied and QE is the quantum efficiency of the sensor.

3.4.2. Performance results

Favourable light conditions correction

In order to determine AO performance, green fluorescent beads were first observed in agarose. Beads showed a round shape, with a mean FWHM of $2.61 \times 2.32 \times 3.11$ μm .

When imaging beads at $z = 100$ μm through the glass capillary, the image appeared greatly distorted in the lateral direction. RMS error of the measured wavefront was 0.238 ± 0.014 μm before correction. After correction, the image of the bead was restored, with a similar shape to that of the previous, capillary-free observation. RMS error after correction was 0.011 ± 0.001 μm . Strehl ratio (estimated using the Maréchal approximation) improved from 0.007 ± 0.021 to 0.983

3.4. ADAPTIVE OPTICS PERFORMANCE

± 0.005 . Contrast was improved by an average $80\% \pm 29\%$ (peak signal to background).

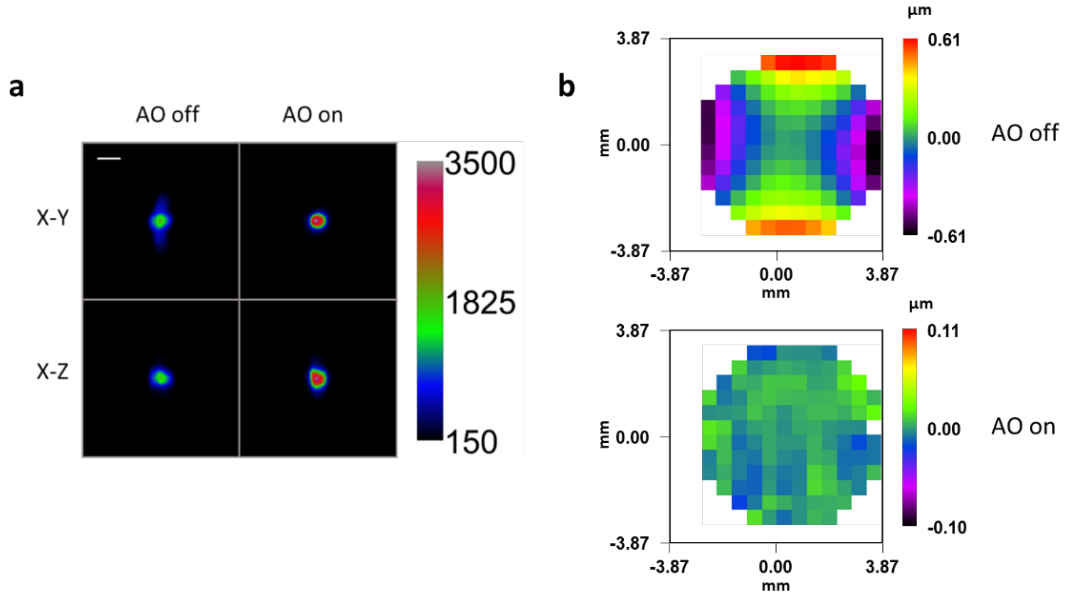


Figure 3-13: (a) Maximum intensity projection of green fluorescent beads embedded in 1% agarose and imaged through a capillary glass at a depth of 100 μm , both before and after AO correction. Scale bar: 5 μm . Beads were illuminated with constant intensity at 491 nm. (b) Measured wavefronts before and after correction, offset by the reference wavefront corresponding to an aberration-free system.

Table 3-4: Mean full width at half maximum (FWHM), RMS aberration and Strehl ratio (SR) values for beads imaged through a glass capillary before and after correction.

	AO off	AO on
FWHM_x (μm)	3.38 ± 0.18	2.61 ± 0.12
FWHM_y (μm)	4.68 ± 1.16	2.43 ± 0.28
FWHM_z (μm)	3.49 ± 0.54	3.78 ± 0.46
RMS (μm)	0.238 ± 0.014	0.011 ± 0.001
SR	0.007 ± 0.004	0.983 ± 0.002

Performance in low-light conditions

A similar experiment as above, in which beads were imaged through a glass capillary, was performed with decreasing illumination intensity. During experiments,

emission intensity was measured as a fraction of the saturation value of the SHWS, defined as the maximum readable intensity for each pixel. The number of captured photons was later calculated from the acquired SHWS images.

Corrected images typically achieved imaging near the diffraction limit ($SR > 0.8$). Good corrections were obtained with as few as 12×10^3 signal photons over the pupil, with correction performance increasing with intensity. For intensities below 12×10^3 photons (6.6% of SHWS saturation value), our software failed to measure wavefront aberrations due to low SNR, making it impossible to correct the image. Beyond that limit, corrections typically allowed for imaging near the diffraction limit.

Table 3-5: Mean correction results for images of beads through a glass capillary for different emission intensities.

	AO on			
	7%	8%	9%	10%
FWHM_x (μm)	2.672 ± 0.019	2.695 ± 0.016	2.686 ± 0.018	2.682 ± 0.018
FWHM_y (μm)	2.343 ± 0.030	2.230 ± 0.045	2.277 ± 0.030	2.281 ± 0.025
FWHM_z (μm)	3.491 ± 0.073	3.483 ± 0.065	3.495 ± 0.070	3.540 ± 0.063
RMS (μm)	0.025 ± 0.002	0.016 ± 0.001	0.014 ± 0.001	0.013 ± 0.001
SR	0.909 ± 0.011	0.961 ± 0.003	0.969 ± 0.003	0.973 ± 0.002

AO performance as a function of the number of closed loop iterations employed in the correction for fixed emission intensity was evaluated in a different experiment. Four closed loop iterations were necessary for a good correction in low intensity conditions (8% of SHWS saturation value, 14.5×10^3 to 16.5×10^3 signal photons), while three were enough under high intensity conditions (90% of SHWS saturation value, 290×10^3 to 305×10^3 signal photons).

3.4. ADAPTIVE OPTICS PERFORMANCE

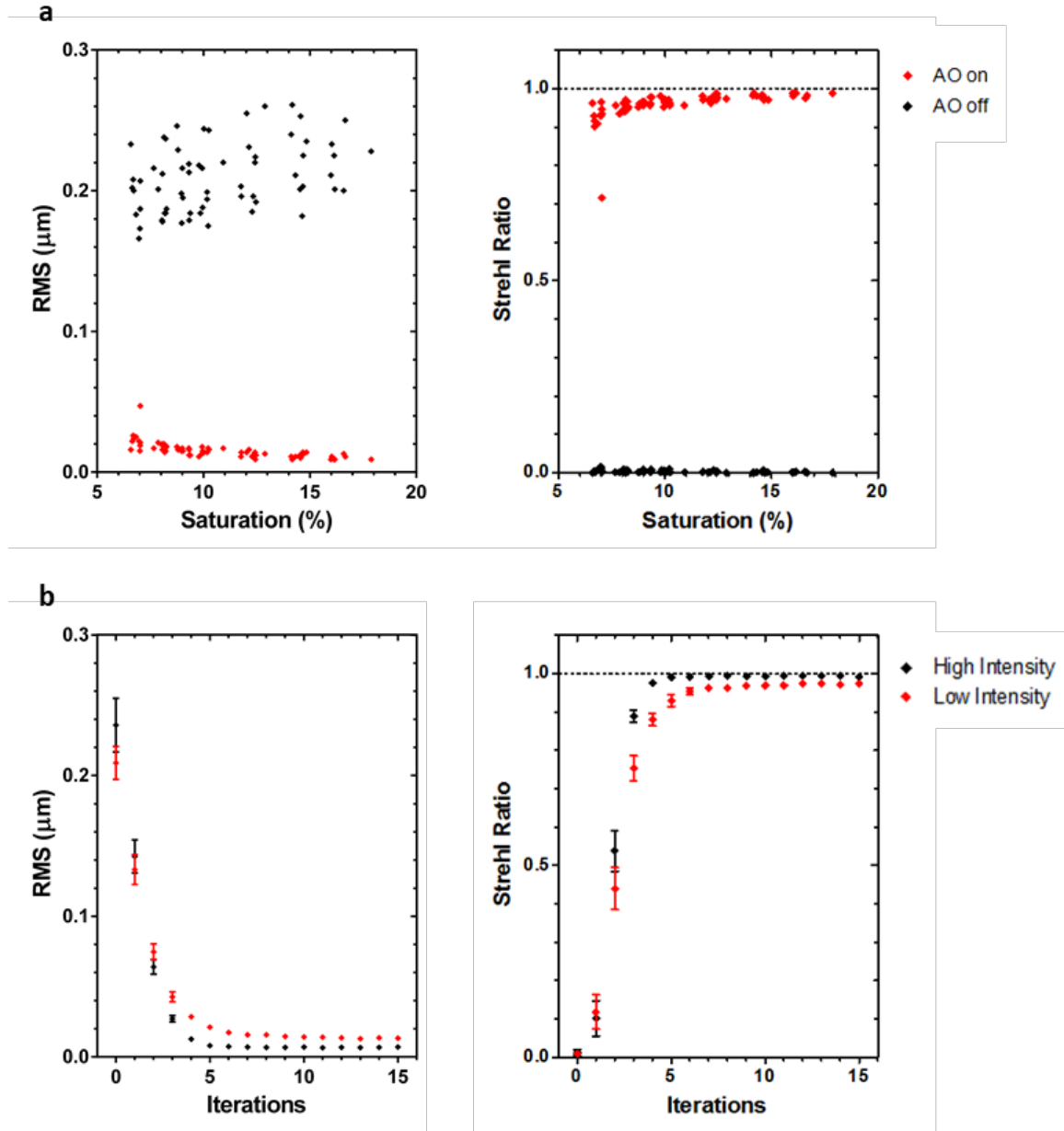


Figure 3-14: (a) RMS and Strehl ratio values of wavefronts before and after correction for a range of light conditions. 15 closed loop iterations were used for each correction. Each pair of points (AO off and AO on) corresponds to a different fluorescent bead. (b) SR and RMS values after correction as a function of the number of iterations used in the closed loop, for fixed low (8% saturation) and high (90% saturation) emission intensity.

3.5. Conclusion

We have implemented an AO-capable SPIM and characterized its correction ability. Since the intended application in TM imaging imposes the restriction of a low available photon flux for wavefront sensing, a custom made EMCCD-based SHWFS was developed by Imagine Optic with our feedback. An assessment of AO correction performance in low photon flux conditions was performed.

It was found that wavefront sensing was the limiting factor in the AO correction. Even though 2×10^5 photons are required for an optimal wavefront reconstruction, as few as 1.2×10^4 signal photons (62 per SHWFS subpupil) are sufficient to measure the wavefront phase in a low-scattering environment. If the wavefront could be reconstructed, AO corrections typically permitted near diffraction-limited imaging ($SR > 0.8$).

The alignment of the two-photon excitation path is crucial, since aberrations arising from its misalignment may cause the NGS to become distorted and appear as an extended light source (especially in the z direction) severely hindering centroid calculation of the Shack-Hartmann spots. In addition, misalignment of the two-photon excitation path causes the typically faint NGS to be even fainter, limiting correction ability in adverse conditions. Our system does not currently have the ability to acquire precise axial information of the NGS, making alignment a difficult process.

The NGS used in our system is $2.2 \mu\text{m}$ when unaberrated. However, NGS intensity decreases exponentially inside MCTS, and its observed diameter tends to increase after $50 \mu\text{m}$, with fast deterioration after approximately $70 \mu\text{m}$.

The SPIM architecture of our microscope, paired with its aberration correction capabilities with a low photon flux using non-invasive methods, makes it a powerful tool for TM imaging.

Chapter 4

MULTI-CELLULAR TUMOR SPHEROID IMAGING

4.1. Introduction

Multi-cellular tumor spheroids are three-dimensional cultures of tumoral cells grown in a roughly spherical shape. They are a widely used TM that has proven invaluable in the study of cancer progression and treatment. However, MCTS are notoriously difficult to image in depth due to the high levels of aberration and scattering introduced by the sample.

In this chapter, I show the ability of our w_{AO} SPIM setup to improve the quality of images of MCTS up to 120 μm deep. For imaging and NGS generation purposes, we marked the H2B histone present in the nucleus with GFP and KillerRed fluorophores. As a histone, H2B has a role on structuring and condensing DNA

during the different phases of the cell cycle and it is therefore commonly used to observe DNA distribution inside the nucleus [100].

AO corrections allowed us to resolve subcellular features that were not resolved before correction, as it is made clear by an increase of high spatial frequency features after correction. AO corrections allowed us to clearly discern biologically relevant features, such as mitotic cells, that couldn't be observed before correction.

4.2. Methods

The ability of $w_{AO}SPIM$ to correct aberration within TM was evaluated using MCTS made from the HCT116 cell line. The MCTS expressed H2B-GFP and ArrestRed (H2B-tKR) histones and were fixed at a diameter of around 300 μm . ArrestRed has an emission maximum at 610 nm and was used for imaging, whereas H2B-GFP was used for both NGS generation and imaging purposes. The spheroids were embedded in 1% agarose cylinders.

An NGS was employed for wavefront reading. H2B-GFP was excited with a 780 nm femtosecond pulsed laser, with an emission peak around 510 nm. A full characterization of the NGS is provided in section 3.2.2. Corrections were performed at different points and depths using different exposures depending on NGS intensity. MCTS were imaged using 100 ms exposures.

Improvements in image quality were quantitatively assessed in terms of spatial frequency [24]. Let $u(x, y)$ be an $M \times N$ image, and let $\hat{u}(f_x, f_y) = \mathcal{F}(u(x, y))$ be its Fourier transform, defined for $(f_x, f_y) \in [0, M - 1] \times [0, N - 1]$. Fourier representation allows us to determine the frequencies corresponding to an object of a size d_r . By angularly projecting the Fourier transform we can represent its value as a function of the size of the object, ignoring the influence of orientation.

For this we construct a set of concentric rings Ω_r comprising frequencies $|f_x| = M/2d_r$ in the x direction and $|f_y| = N/2d_r$ in the y direction. By summing the value of $\hat{u}(f_x, f_y)$ along Ω_r we obtain the angular projection of $\hat{u}(f_x, f_y)$ as a function of the radial frequency f_r . Denoting this projection as $\hat{U}(f_r)$:

$$\hat{U}(f_r) = \frac{\sum_{\Omega_r} |\hat{u}(f_x, f_y)|}{|\hat{u}(0,0)|}. \quad (4-1)$$

By comparing $\hat{U}(f_r)$ before and after correction we can evaluate improvements in frequencies corresponding to specific feature sizes. We define the relative difference, RD , of radial frequencies between images acquired before and after correction ($\hat{U}_{off}(f_r)$ and $\hat{U}_{on}(f_r)$, respectively) as:

$$RD(f_r) = \frac{\hat{U}_{on}(f_r) - \hat{U}_{off}(f_r)}{\hat{U}_{off}(f_r)}. \quad (4-2)$$

Improvements in observed high-frequency detail can be readily assessed by evaluating $RD(f_r)$. The 3D images were split in several z-sections and a maximum intensity z-projection was done in each of them. RD was evaluated in each section for corrections performed at different depths.

4.3. Results

MCTS were observed while embedded in 1% agarose cylinders before and after AO correction at different depths. Typically, a maximum of five to ten closed loop iterations could be performed due to the fast bleaching of the fluorophore and the long exposure times required for wavefront measurements (usually from 0.3 to 1s, depending on the sample and location of the guide star).

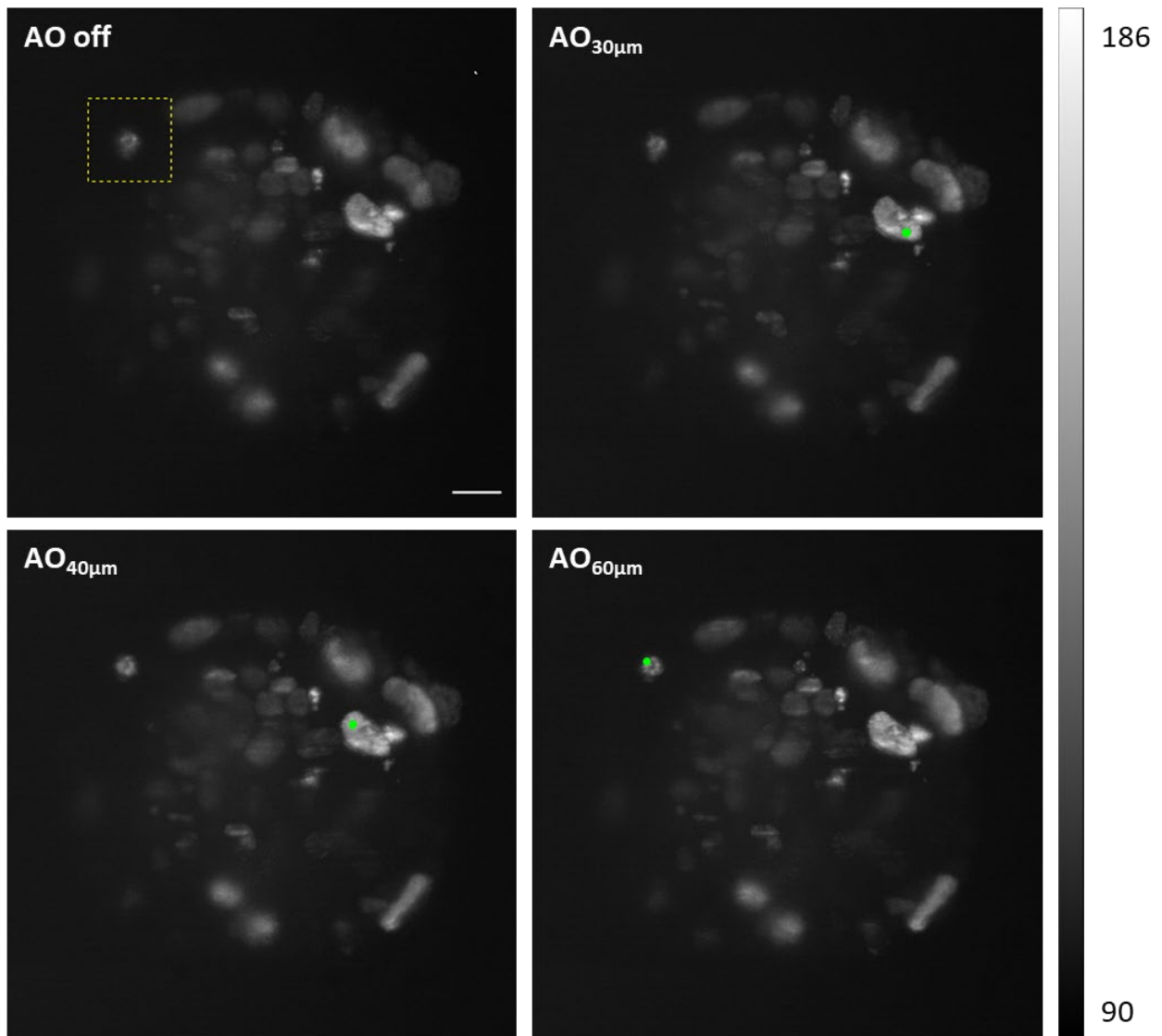


Figure 4-1: Maximum intensity projection of an MCTS expressing H2B-GFP. The MCTS was imaged before AO correction and after corrections performed at 30, 40 and 60 μm deep with the guide star placed at the green spots in each case. Corrections were performed using 1s exposures. Scale bar: 25 μm . The highlighted feature is further analysed in Figure 4-3.

Figure 4-1 shows a maximum intensity projection of an MCTS imaged up to 150 μm deep. Corrections were performed at depths of 30, 40 and 60 μm , with guide stars located at different suitable points for each correction. The AO-corrected images

4.3. RESULTS

show improvements in resolution and contrast when compared to the uncorrected one.

Wavefronts were measured before and after correction for each case. RMS aberration was reduced by 61.5 %, 70.9 % and 87.6 % for corrections performed at 30 μm , 40 μm and 60 μm , respectively (figure 4-2). RMS values before and after correction are provided in Table 4-1.

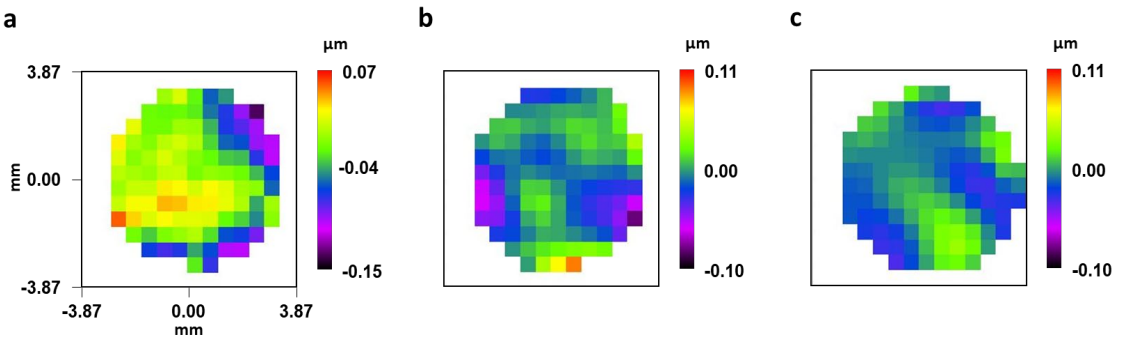


Figure 4-2: Measured wavefronts after AO corrections at different depths. a) Correction at 30 μm . b) Correction at 40 μm . c) Correction at 60 μm .

Table 4-1: RMS aberration before (RMS_{off}) and after AO correction (RMS_{on}) at different depths.

Correction depth	RMS_{off} (μm)	RMS_{on} (μm)
30 μm	0.096	0.037
40 μm	0.086	0.025
60 μm	0.129	0.016

Image quality improvements after AO correction are especially clear in the region of interest highlighted in figure 4-1. This ROI features a single cell nucleus located at a depth spanning approximately from $z = 55 \mu\text{m}$ to $z = 65 \mu\text{m}$. XY and XZ projections of the cell before and after AO corrections are provided in figure 4-3. Improvements in image quality are greater for corrections performed at 40 μm and 60

μm , since the guide star is spatially closer to the feature. While the uncorrected image is too blurry to extract any useful information, AO correction allows us to clearly identify a spatial structure of H2B (and hence DNA). The ring-like distribution shows H2B forming chromosomes that are split apart at different ends of the nucleus, as it is characteristic of a cell undergoing metaphase.

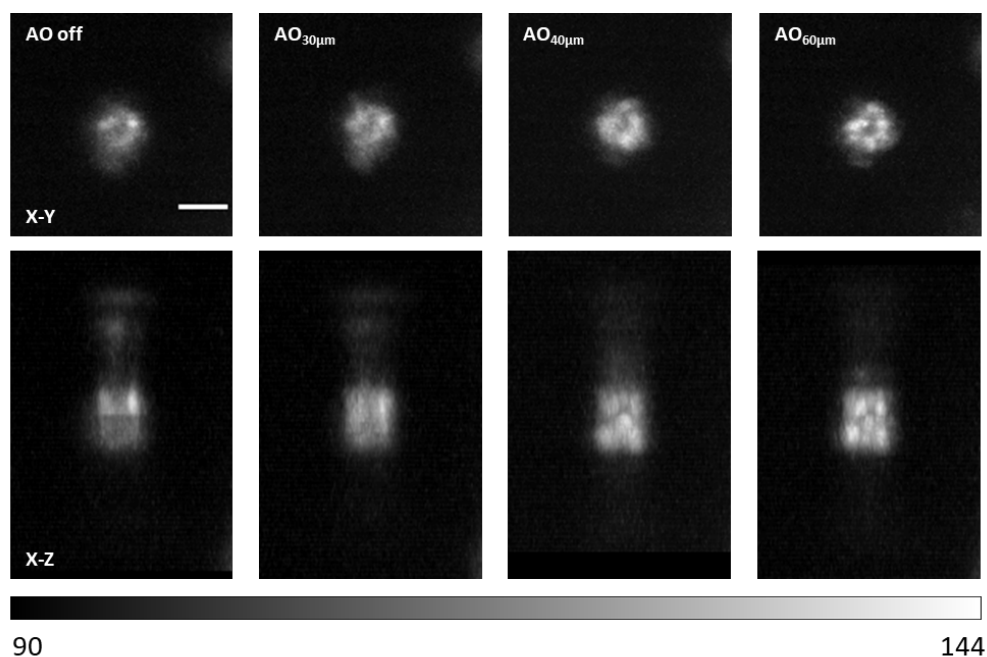


Figure 4-3: Maximum intensity projection of an HCT116 nucleus expressing H2B-GFP, located at a depth of approximately $60 \mu\text{m}$ inside the MCTS. The cell was imaged before AO correction and after corrections were performed at a depth of 30 , 40 and $60 \mu\text{m}$. Structured DNA can be easily discerned after corrections at $40 \mu\text{m}$ and $60 \mu\text{m}$. Scale bar: $10 \mu\text{m}$.

Figure 4-4 shows an MCTS expressing ArrestRed (H2B-tKR) before AO correction and after correction at 30 , 50 and $80 \mu\text{m}$. The spheroid was imaged up to $120 \mu\text{m}$ deep each time. In order to quantitatively analyse image quality improvements at different depths, the 3D images were divided into three Z sections ($Z_{1-40\mu\text{m}}$, $Z_{41-80\mu\text{m}}$, $Z_{81-120\mu\text{m}}$), after which a maximum intensity projection was

4.3. RESULTS

performed in each one. A region of interest was selected at each z-section. Projections for each ROI and correction depth are provided in figure 4-5.

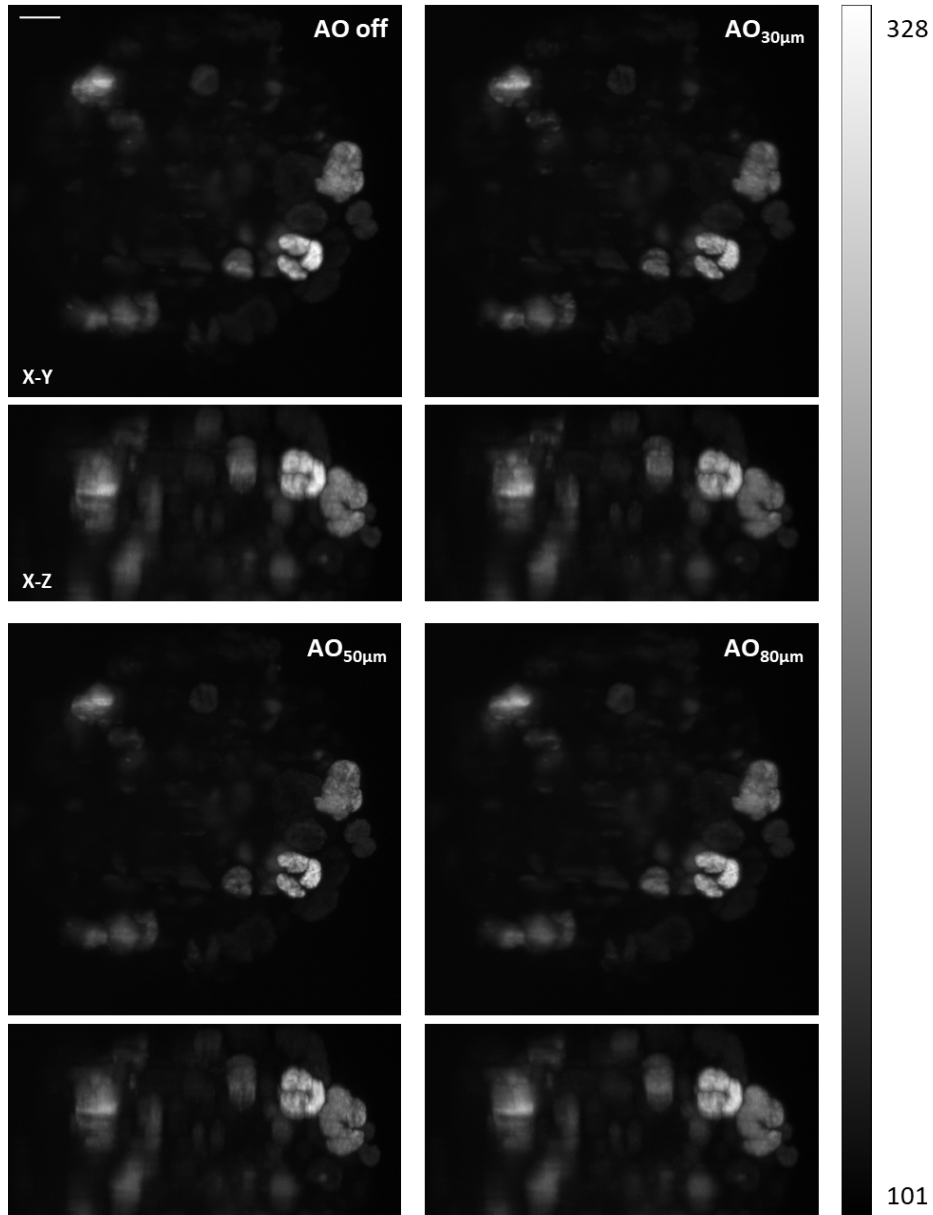


Figure 4-4: Maximum intensity projections of an MCTS expressing the fluorescent histone ArrestRed before AO correction and after corrections were performed at 30, 50 and 80 μm . Corrections were all performed using 1s exposure. Scale bar: 25 μm .

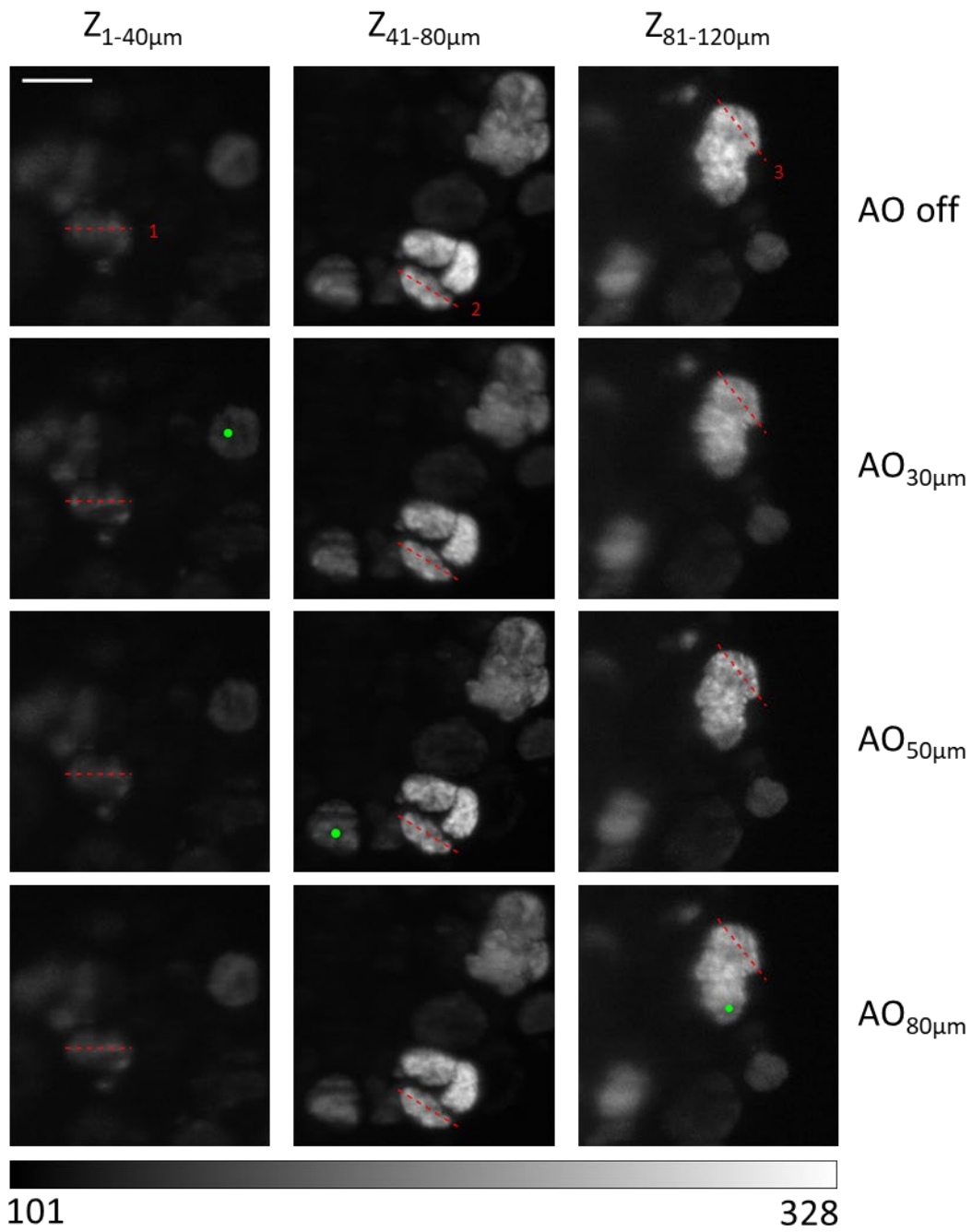


Figure 4-5: Maximum intensity projection of three regions of an MCTS before and after AO correction. NGSs were placed at the green dots in the respective corrections. Scale bar: 25 μm .

4.3. RESULTS

The AO-corrected images show again improvements in contrast and resolution with respect to the uncorrected image. Subcellular sized structures that were not well resolved in the “AOs off” position can be resolved after correction.

Frequencies were evaluated by means of angular projections of the Fourier transform of the images, as described in section 4.2. Profiles along the paths highlighted in figure 4-5, along with relative differences of frequencies with respect to the uncorrected image are shown in Figure 4-6.

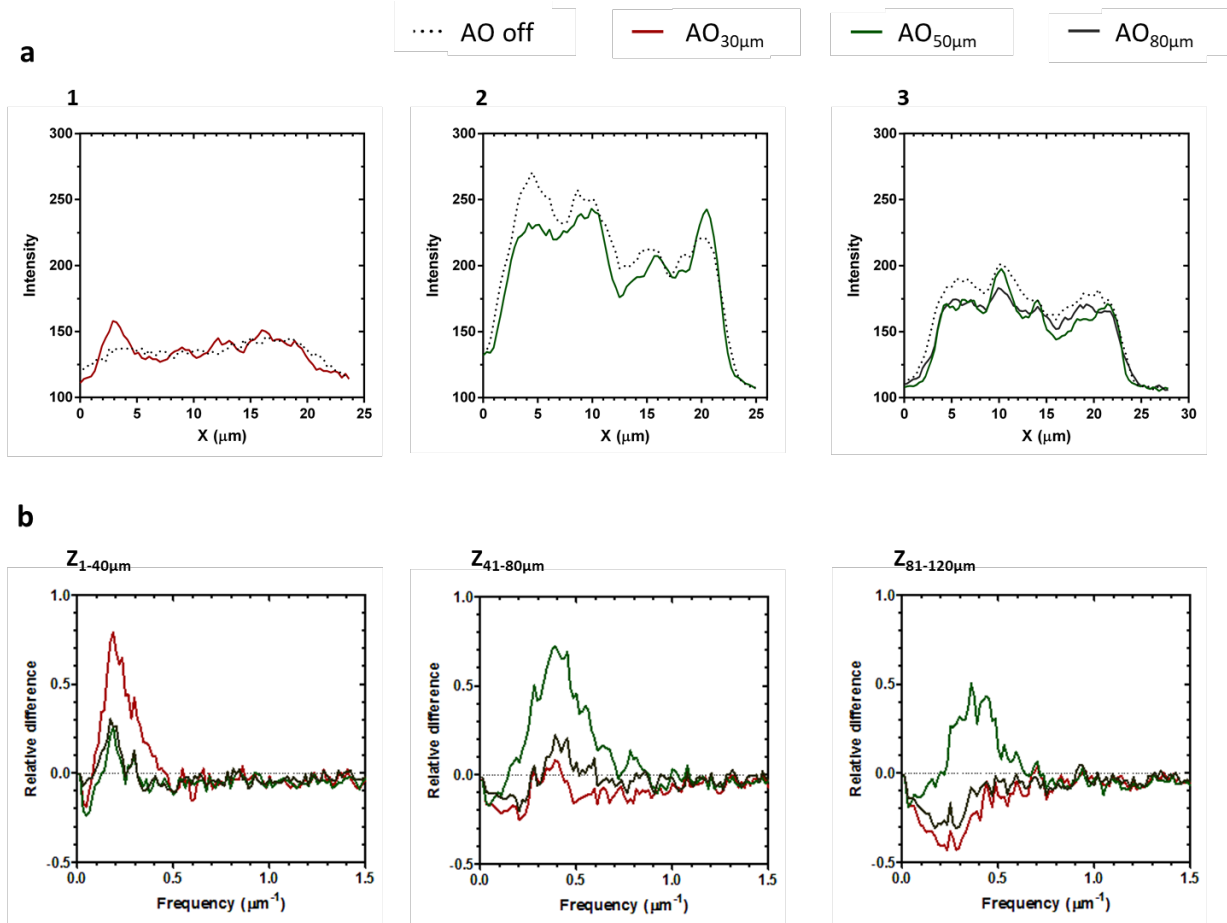


Figure 4-6: Quantitative analysis of AO correction in MCTS. **a)** Intensity profiles along paths 1,2 and 3 of Figure 4-5. **b)** Relative differences of spatial frequencies between each of the corrections and the uncorrected case for each region of interest.

Compared to the uncorrected case, there is a substantial increase (up to 79%) of frequencies in the range 0.1 to $0.8 \mu\text{m}^{-1}$, corresponding to features of cellular and subcellular size (1.25 to $10 \mu\text{m}$). Frequencies outside this range show a slight decrease. For the $Z_{1-40\mu\text{m}}$ section, the most efficient correction was realized at $30 \mu\text{m}$, while at the $Z_{41-80\mu\text{m}}$ section the most efficient was realized at $50 \mu\text{m}$. At $Z_{81-120\mu\text{m}}$ imaging depth, AO correction becomes unreliable and those performed at 30 and $80 \mu\text{m}$ showed a general worsening of image quality, although the one performed at $50 \mu\text{m}$ showed a slight improvement.

4.4. Discussion

We have shown how AO corrections can improve in-depth imaging in optically thick MCTS. Our system is capable of reducing the MCTS-induced aberrations by up to 87.6% (RMS), resulting in improvements in image quality regarding resolution and high-frequency detail. Corrections are more effective near the guide star, and result in greater image quality gains when performed at shallow depths. The reduction of aberrations allows the identification of biologically relevant features (such as chromosome distribution) inside MCTS where only blurry outlines could be previously observed².

Correction depth is mainly limited by scattering. Signal-to-noise ratio degrades deeper into the sample due to the loss of ballistic photons and the increase of noise originating from scattered light. The loss of SNR translates into a loss of accuracy of the Shack-Hartmann spots centroid calculation, resulting in inaccurate wavefront readings, and the total inability to measure the wavefront at greater depths. Although wavefront reading is typically impossible deeper than around $100 \mu\text{m}$,

² This work has been the subject of a publication, provided here as an appendix.

corrections performed at shallower depths can still improve image quality after that point.

Another relevant issue when performing AO corrections is the fast bleaching of the NGS. Typically, between 5 and 10 iterations can be performed before the NGS becomes too faint to measure the wavefront. This is more prominent at greater depths, as scattering further limits the amount of available light. In its current state, our system is controlled by several different software and manual controls, resulting in the generation of an NGS for a few seconds while no correction is being performed and further limiting the maximum number of iterations per correction. A more integrated hardware and software could provide an increase of 1 to 3 iterations per correction.

To sum up, wAO SPIM permits imaging of features of subcellular size at depths inaccessible to standard SPIM setups. By using an NGS, we can perform corrections targeted at the desired region of interest while keeping intrusiveness to a minimum, making wAO SPIM a powerful and versatile instrument.

Chapter 5

UP-CONVERTING NANOPARTICLES AS GUIDE STARS

5.1. Introduction

Lanthanide-doped up-converting nanoparticles (UCNP) are inorganic nanomaterials in which the lanthanide cations embedded in the host matrix can convert incident NIR light to visible or ultraviolet light. Unlike other nonlinear processes such as second harmonic generation or two-photon fluorescence, photon up-conversion involves real intermediate energy levels, with lifetimes of up to tens of milliseconds (compared to hundreds of attoseconds for two-photon fluorescence) [101]. The longer lifetimes of the intermediate states reduce the required excitation power by several orders of magnitude, allowing the use of lamps or continuous wave lasers as illumination sources.

The excitation by NIR light sources makes UCNP compatible with biological tissue imaging, as photodamage is kept to a minimum and autofluorescence is nearly absent. In addition, they present no blinking or bleaching upon continuous NIR irradiation over long periods [102]. Hence, they are excellent tools for long-term in-vivo imaging of live samples [103].

UCNP are formed by a substrate, such as NaYF_4 or NaGdF_4 , that is usually doubly doped by a sensitizer cation, typically Yb^{3+} , and an activator cation, such as Yb^{3+} , Er^{3+} or Tm^{3+} . The optical properties of the UCNP (e.g. emission and excitation wavelength, quantum yield, photostability) depend mainly on the cation pair of choice [104].

The advantageous optical properties of UCNP can be exploited for their use in adaptive optics. Given their photostability and intensity, a guide star made from such material could allow performing frequent and fast AO corrections comprising tens of closed-loop iterations with no photobleaching of the guide star while being completely innocuous to the sample. However, since individual particles are not bright enough for wavefront reading, small aggregates of them would have to be used as a guide star. In addition, while the optical compatibility of UCNP with biological tissue is remarkable, the toxicological compatibility is not so clear. Hence, in order to make useful guide stars, the UCNP must meet the following requirements:

- i. They must not interfere with cell physiology or tissue development.
- ii. They must form aggregates that are small enough to be considered point-like (less than 10 μm) but large enough to provide a sufficient amount of photons for wavefront reading.

In this chapter, the adequacy of $\text{NaYF}_4:\text{Yb},\text{Tm}$ -based UCNP to be used as guide stars for AO correction is evaluated using the criteria established above.

5.2. Methods

The UCNP employed in this chapter, denoted CR3936-69P1, consist on NaYF₄:Yb,Tm nanoparticles coated in PEG₆₀₀₀-PAA₆₅₀₀, with a size of 36 ± 4 nm. CR3936-69P1 has photon up-conversion emission peaks at 346, 362, 452 and 476 nm as well as a much greater peak at 801 nm.

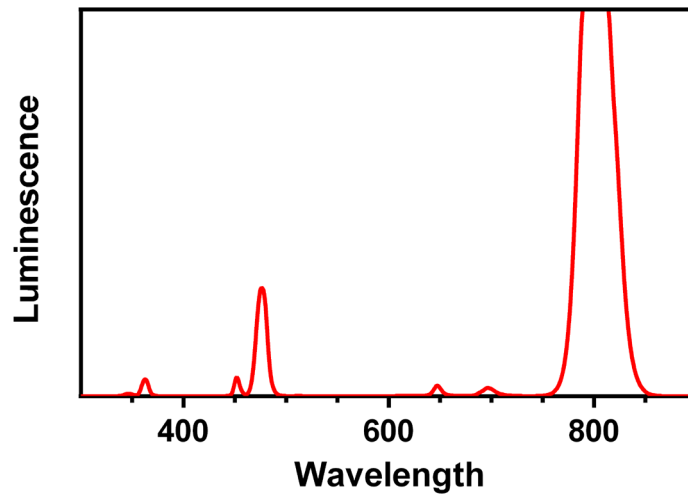


Figure 5-1: CR3936-69P1 up-conversion spectrum.

HCT116-H2BGFP/ArrestRed cells were cultured in DMEM+GlutaMAX (Dulbecco's modified eagle medium; Thermo Fisher Scientific, Walt ham, USA), supplemented with 10% fetal bovine serum and 1% penicillin–streptomycin (Pen Strep; Gibson), and maintained at 37 °C with 5% CO₂ in an incubator. Cells were mixed with different concentrations of UCNP prior to MCTS preparation. MCTS were prepared in ultra-low attachment 96-well plates (Costar). Cells were plated at a density of 700 cells/well in 100 μ l cell culture medium per well, and then centrifuged to enable MCTS formation. After five days of growth, some of the MCTS were collected, washed three times with PBS, before being fixed with 10% neutral buffered formalin (Sigma-Aldrich) at room temperature for two hours. Live MCTS were measured after 4 and 8 days of growth.

MCTS were mounted on 1% agarose cylinders for imaging. Firstly, widefield transmitted light images of the MCTS were taken, after which an NIR light sheet was used to excite the UCNP, which were imaged by conventional SPIM.

The viability of several UCNP solubilization strategies was studied. For this, MCTS were grown in the presence of both UCNP and a 1 mg/ml BSA solution. UCNP concentrations of 0.1 $\mu\text{g/ml}$ and 1 $\mu\text{g/ml}$ were employed in each case. MCTS were measured and fixed after 5 days.

5.3. Results

5.3.1. Toxicity

The compatibility of CR3936-69P1 with biological tissue was determined. For this, MCTS were grown in the presence of CR3936-69P1, in concentrations ranging from 0.1 $\mu\text{g/ml}$ to 100 $\mu\text{g/ml}$.

A concentration of 0.1 $\mu\text{g/ml}$ produced MCTS with a mean size of 340 nm and 490 nm after 4 and 8 days, respectively. This is in accord with growth dynamics of unperturbed MCTS and, thus, this concentration did not appear to hamper MCTS growth. However, larger concentrations significantly affected MCTS growth. After 4 days, MCTS were 7.4% and 16.7% smaller when grown in 1 $\mu\text{g/ml}$ and 10 $\mu\text{g/ml}$ concentrations, respectively (Table 5-1, Figure 5-2). The size difference was reduced to 4.6% and 12.1% after 8 days (Table 5-2).

5.3. RESULTS

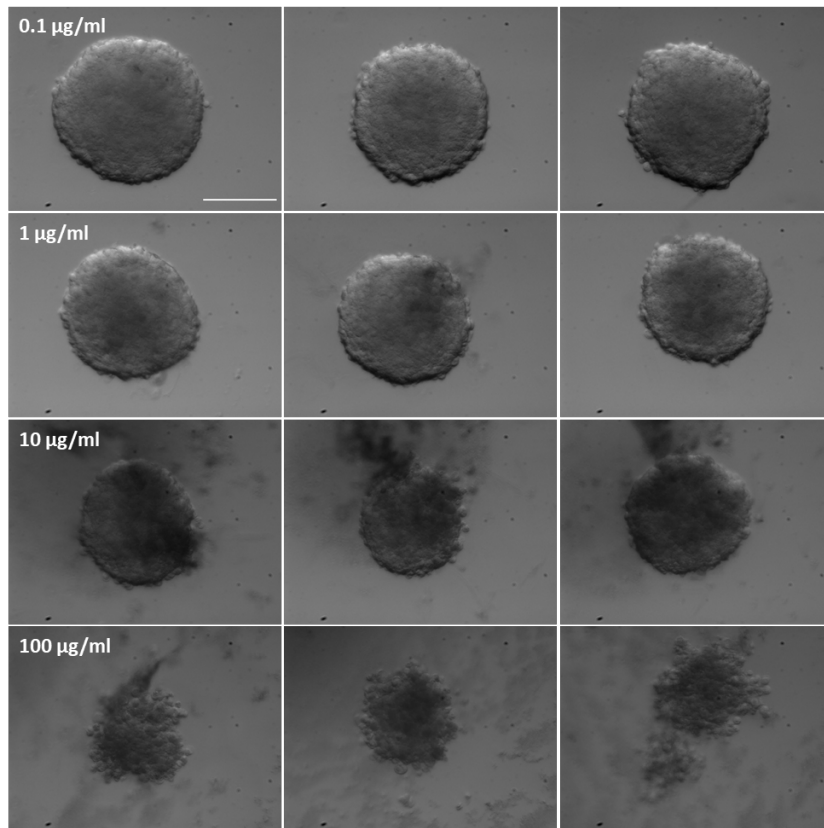


Figure 5-2: Widefield image of MCTS after 4 days of growth in presence of different concentrations of CR3936-69P1. MCTS grown in 0.1 $\mu\text{g/ml}$ concentrations exhibited a nominal development, while those grown in 1 $\mu\text{g/ml}$ and 10 $\mu\text{g/ml}$ presented a slower growth. Cells grown in 100 $\mu\text{g/ml}$ concentrations did not ultimately form spheroids. Scale bar: 150 μm .

Cells plated in the presence of 100 $\mu\text{g/ml}$ CR3936-69P1 did not form spheroids after 4 days, arranging in irregular aggregates instead. These cell aggregates had dispersed by the 8th day.

Table 5-1: Size of MCTS grown in the presence of CR3936-69P1 after 4 days.

CR3936-69P1 concentration	MCTS size (μm)
0.1 $\mu\text{g/ml}$	340.0 ± 32.5
1 $\mu\text{g/ml}$	315.8 ± 17.4
10 $\mu\text{g/ml}$	283.3 ± 24.6
100 $\mu\text{g/ml}$	Irregular cell aggregates

Table 5-2: Size of MCTS grown in the presence of CR3936-69P1 after 8 days.

CR3936-69P1 concentration	MCTS size (μm)
0.1 $\mu\text{g/ml}$	490.0 ± 14.1
1 $\mu\text{g/ml}$	467.5 ± 25.6
10 $\mu\text{g/ml}$	430.8 ± 42.7
100 $\mu\text{g/ml}$	Few scattered cells

5.3.2. Distribution inside MCTS

The viability of using UCNP as guide stars depends on their spatial distribution inside the spheroid, due to the requirement that guide stars must be point-like. A single nanoparticle acts as a point-like source of light, but its small size causes it not to be intense enough to be useful. Therefore, clusters of UCNP should be big enough to produce a workable signal-to-noise ratio but small enough to be considered point-like. Furthermore, these clusters should be uniformly distributed over the MCTS in order to provide a versatile selection of regions of interest in which to perform the AO correction.

5.3. RESULTS

Due to toxicity of CR3936-69P1 at high concentrations, MCTS were grown in UCNP solutions at 0.1 $\mu\text{g}/\text{ml}$ and 1 $\mu\text{g}/\text{ml}$. They were fixed and observed after 5 days. The nanoparticles formed aggregates with a size of up to tens of microns (Figure 5-3). These aggregates tended to cluster in on size of the spheroid, leading to a total lack of UCNP in most of the MCTS.

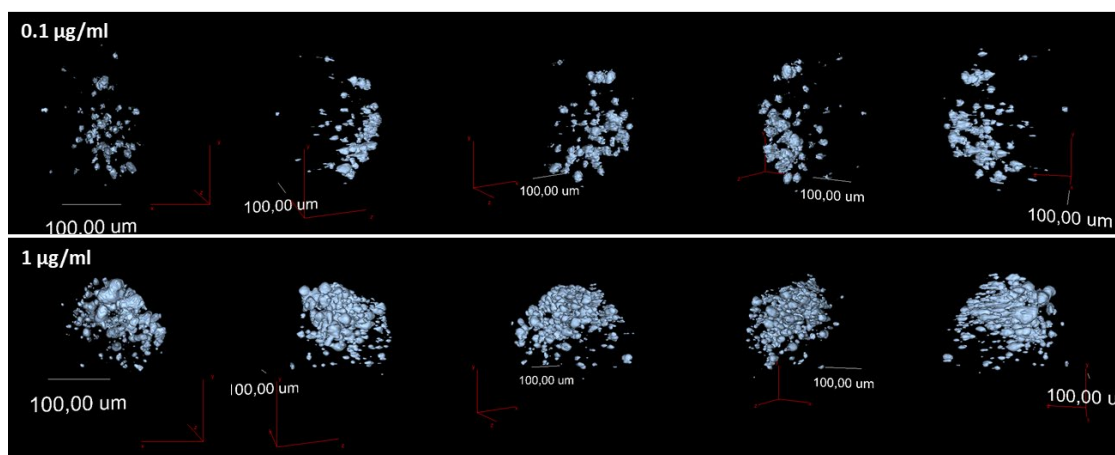


Figure 5-3: Three-dimensional distribution of nanoparticles on MCTS as seen from different angles over the Y axis. UCNP formed aggregates with a typical size of up to tens of μm , which tended to be clustered in one side of the spheroid. MCTS grown in 1 $\mu\text{g}/\text{ml}$ CR3936-69P1 presented larger and brighter aggregates of UCNP. Intensity data not shown.

Increasing nanoparticle concentration did not translate into a more uniform distribution. Instead, the UCNP formed a greater number of aggregates, which were larger and brighter. However, they still clustered in a side of the spheroids while not being present in the rest of their volume.

The distribution of UCNP into a single large cluster in each MCTS led us to believe that, during their development, the spheroids were not properly spreading the nanoparticles in the vertical direction, probably due to the short precipitation time of CR3936-69P1 (a few minutes). As the consequence, the UCNP rested at the bottom of the spheroids, producing a highly unbalanced distribution.

Bovine serum albumin (BSA) is a commonly used protein known to enhance solubility and promote surface biofunctionalization [105]. To improve UCNP distribution and avoid an accumulation of them at the bottom of the spheroid, a batch of MCTS were grown in presence of both CR3936-69P1 and BSA.

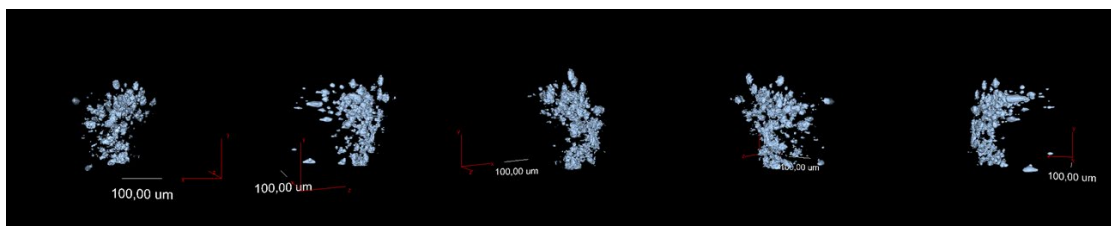


Figure 5-4: Effect of BSA on the three-dimensional distribution of nanoparticles on an MCTS. MCTS were grown in a 1 $\mu\text{g}/\text{ml}$ CR3936-69P1, 1 mg/ml BSA solution. No substantial improvements caused by the addition of BSA could be observed.

The resulting nanoparticle distribution was similar to that obtained in the absence of BSA. UCNP formed aggregates that grouped into a single large cluster, presumably at the bottom of the MCTS.

5.4. Discussion

Up-converting nanoparticles are rare-earth-based particles that undergo photon up-conversion when excited, emitting photons of higher energy than the captured ones. This characteristic makes UCNP an attractive approach to guide stars, as they can be illuminated using NIR light while emitting in the visible, substantially decreasing photodamage to the sample. We have studied the viability of one of such UCNPs, CR3936-69P1, to be used as guide stars in TMs.

One of the predicted possible issues with rare-earth based compounds is toxicity to the sample. We found that CR3936-69P1 hinders MCTS growth at concentrations

greater than 0.1 $\mu\text{g}/\text{ml}$. However, effects on the physiology of the tissue at lower concentrations cannot be definitively discarded without further research.

While a concentration of 0.1 $\mu\text{g}/\text{ml}$ provides enough light to be able to measure the wavefront in our setup, the three-dimensional spatial distribution of the nanoparticles makes this task impossible. The point-like nature of guide stars and the resolution of our SHWFS require that the sources of light do not surpass roughly 9 μm . However, the aggregates that are bright enough to be used as a guide star have diameters typically greater than 20 μm . However, our setup uses an inefficient illumination system, with an objective that is not optimal for NIR applications, blocking around 90% of the incoming beam intensity. The use of a better suited illumination objective would probably allow wavefront reading using much smaller UCNP aggregates, with sizes suitable for their use as guide stars.

A more worrying issue is the fact that the UCNP aggregates distribution is not uniform over the volume of the MCTS. The UCNP tend to form a large cluster in one side of the spheroid, while, at most, very small amounts are present anywhere else. Therefore, no corrections can be performed in most of the volume of the spheroid due to a lack of guide star. Since the fast precipitation of CR3936-69P1 was assumed to be the main factor in the uneven UCNP distribution, we tried to improve their solubility and cell adhesion by adding BSA to the MCTS growth medium. However, the addition of BSA did not lead to a more uniform distribution.

In summary, CR3936-69P1 does not evidently affect MCTS development at low concentrations ($< 0.1 \mu\text{g}/\text{ml}$). This UCNP concentration can offer small nanoparticle aggregates, which are presumed to provide enough light for wavefront reading with an NIR-optimized illumination system. Therefore, the main detriment for the use of UCNP as guide stars is their uneven distribution inside the MCTS due to the low solubility of the nanoparticles. Further research in solubilization strategies for these UCNP with the objective of improving solubility or suspension time could open the

way for this application. Specifically, precipitation times longer than 4 or 5 days could provide a uniform UCNP distribution over the volume of the MCTS.

Chapter 6

CONCLUSION

Over the last years, TM have acquired increasing relevance in the study of biological processes, since they provide a physiologically relevant environment for cell growth, tissue morphogenesis and disease spread. A popular tool for TM imaging is light sheet fluorescence microscopy, as it provides fast 3D acquisition with minimal photodamage to the sample. However, in-depth optical imaging of TMs poses a challenge due to absorption, scattering and aberration arising from the sample. This thesis is devoted to the improvement of in-depth imaging of such challenging samples by combining LSFM with adaptive optics.

Summary

I have implemented an adaptive SPIM that makes use of a non-linear guide star and a custom high-sensitivity Shack-Hartmann wavefront sensor to correct aberrations arising from the sample. The NGS used in our system can be placed at will over the FOV, allowing the correction of aberrations in any region of interest.

Additionally, the infrared light used for the two-photon excitation suffers from minimal absorption and scattering, generating useful NGS up to 100 μm deep in TMs.

The main concern regarding NGS is the low amount of light emitted, especially when working with rather opaque samples. To be able to measure the wavefront in TMs, we employed a custom high-sensitivity wavefront sensor based on EM-CCD technology. We have fully characterized the system and shown that adequate corrections can be performed with as few as 12000 photons. Even so, long exposures (0.3 s - 1 s) are required to collect that many photons from NGS in TMs. When coupled with fast bleaching, this severely limits the amount of correction steps that can be completed to between 5 and 10. However, further optimization of our system, especially the control software, seems straightforward and could somewhat alleviate this problem.

The ability of wAO SPIM to correct aberrations has been demonstrated in fixed MCTS, showing improvements in in-depth imaging regarding resolution and high-frequency detail. RMS aberration was reduced by up to 87,6%. Image improvements are greater near the guide star and when the correction is performed at shallow depths. AO correction allowed us to clearly identify previously-undistinguishable mitotic cells.

However, scattering limits the maximum depth at which useful corrections can be performed. Indeed, the loss of SNR usually precludes aberration correction deeper than 100 μm , even though shallower corrections can slightly improve image quality after this point.

The use of up-converting nanoparticles as guide stars could provide a way to increase the maximum depth accessible to AO. They can be illuminated with IR light, produce high emission intensities and show negligible photobleaching. However, their toxicity for TMs has never been ascertained, and their small size requires them to be clustered to provide enough light for wavefront reading. We proved that MCTS

show slower development when in presence of UCNP concentrations upwards of 1 $\mu\text{g}/\text{ml}$.

A more severe issue with the use of UCNP is the lack of uniform coverage inside TMs. The nanoparticles tend to cluster at the bottom of the spheroid, with almost no presence in over half of it. We believe that this is a consequence of the lack of solubility of the tested UCNP. Exploratory trials with the objective of increasing their solubility in cell culture medium were unsuccessful.

Perspectives

Given the versatility of LSFM and the many innovations present in the literature, there is a vast amount of options for further development of our microscope.

Our wAO SPIM system can adequately correct aberrations in highly scattering samples, but the maximum depth at which we can improve imaging is limited by scattering to around 120 μm . While this is enough for small TMs, larger samples would benefit from deeper corrections. It is thus desirable to increase the SNR produced by the guide star in such conditions.

Beads and UCNP can provide more light than NGS, improving the SNR and allowing correction at greater depths [23]. The use of UCNP is however more desirable than fluorescent beads, since they exhibit almost no photobleaching and IR illumination is less damaging to the sample. By optimizing the illumination path of the system for NIR light, we could potentially use small UCNP aggregates as guide stars in non-toxic concentrations. However, their uneven distribution inside MCTS makes this impractical. It is my belief that further research into the assimilation of UCNP by biological tissue, especially TMs, could lead to greater viability of their use as guide stars. Another approach worth of consideration to increase SNR is the use of longer wavelength guide stars, which are less sensitive to scattering [73]. The longest accessible wavelength is, however, limited by the optics of the detection path of the

microscope, which are coated for the visible and thus block wavelengths longer than approximately 700 nm.

A scanned NGS approach has been proposed to decrease speckle-like artifacts in the wavefront sensor image [73]. By scanning the NGS over a small region, scattering artifacts can be averaged out. This approach could somewhat improve wavefront reading accuracy at depth, but it would require a significant redesign of the microscope, as well as an increase of system complexity. We believe the small expected gains (since these artifacts are more prominent in high-resolution systems) are not worth the significant undertaking.

The light sheet is also subject to scattering. Scattered illumination produces undesired fluorescence from out-of-focus regions, giving way to ghost image artifacts and severely decreasing resolution. A dual illumination approach would somewhat alleviate ghosting artifacts, but its implementation would require rethinking the geometry of our system due to the space constraints. A better option would be the use of non-diffractive beams.

Bessel beams have shown increased penetration depth and reduction of ghost artifacts, due to the self-healing nature of the beam [55], [106]. This illumination method could further improve axial and lateral resolution to allow the detection of features deep into the sample. A scanned Bessel beam strategy is especially attractive for our system. By keeping the sample still, the light sheet can be scanned in the z direction while the AO system corrects the resulting defocus, opening the way to faster imaging and simpler sample mounting [49].

Since AO correction is most effective near the guide star, the resulting image quality will vary greatly across the field of view. One of the advantages of NGS is that it can be positioned anywhere in the image, allowing correction near the objects of interest. An image can be repeatedly corrected placing the NGS at different points to later stitch the well-corrected regions together, obtaining a single image that is well corrected everywhere [80]. This approach could be easily implemented in our

microscope, since it would only require the development of a software algorithm. However, it is of limited utility for TM imaging. Indeed, since an acquisition is required for each correction, several exposures are required for each final image. In highly heterogeneous tissue, given the small size of the isoplanatic patch, the number of required corrections per image could easily scale into the hundreds. The increase in acquisition time defeats the main advantages of SPIM: fast acquisitions and low photodamage. Hence, while easy to implement, this tiling method would be useful only in limited cases.

In any case, adaptive optics is a necessary technology for optical TM imaging. While AO is still to be fully embraced by the microscopy community, it is a rapidly developing field that is rapidly expanding the range of applications of optical microscopy. The implementation of current and future ideas in our adaptive wAO-SPIM system will lead to an even more powerful instrument for the imaging of tissue mimics.

References

- [1] M. Born and E. Wolf, *Principles of Optics: Electromagnetic Theory of Propagation, Interference and Diffraction of Light*. CUP Archive, 2000.
- [2] C. Huygens, *Traite de la lumiere. OÙ sont expliquées les causes de ce qui luy arrive dans la reflexion, & dans la refraction. Et particulièrement dans l'étrange refraction du cristal d'Islande, par C.H.D.Z. Avec un Discours de la cause de la pesanteur*. chez Pierre Vander Aa marchand libraire, 1690.
- [3] R. K. Tyson, *Principles of Adaptive Optics*, 4 edition. Boca Raton: CRC Press, 2015.
- [4] von F. Zernike, "Beugungstheorie des schneidenverfahrens und seiner verbesserten form, der phasenkontrastmethode," *Physica*, vol. 1, no. 7, pp. 689–704, May 1934.
- [5] A. B. Bhatia and E. Wolf, "On the circle polynomials of Zernike and related orthogonal sets," *Math. Proc. Camb. Philos. Soc.*, vol. 50, no. 1, pp. 40–48, Jan. 1954.
- [6] R. J. Noll, "Zernike polynomials and atmospheric turbulence*," *JOSA*, vol. 66, no. 3, pp. 207–211, Mar. 1976.
- [7] V. Lakshminarayanan and A. Fleck, "Zernike polynomials: a guide," *J. Mod. Opt.*, vol. 58, no. 7, pp. 545–561, Apr. 2011.
- [8] B. R. A. Nijboer, "The diffraction theory of aberrations," 1942.
- [9] J. Andilla *et al.*, "Imaging tissue-mimic with light sheet microscopy: A comparative guideline," *Sci. Rep.*, vol. 7, no. 1, p. 44939, Apr. 2017.

- [10]E. R. Shamir and A. J. Ewald, “Three-dimensional organotypic culture: experimental models of mammalian biology and disease,” *Nat. Rev. Mol. Cell Biol.*, vol. 15, no. 10, pp. 647–664, Oct. 2014.
- [11]S. L. Jacques, “Optical properties of biological tissues: a review,” *Phys. Med. Biol.*, vol. 58, no. 11, pp. R37–R61, Jun. 2013.
- [12]A. J. Welch and M. J. van Gemert, Eds., *Optical-Thermal Response of Laser-Irradiated Tissue*, 2nd ed. Springer Netherlands, 2011.
- [13]V. Ntziachristos, “Going deeper than microscopy: the optical imaging frontier in biology,” *Nat. Methods*, vol. 7, no. 8, pp. 603–614, Aug. 2010.
- [14]A. J. Nichols, E. Roussakis, O. J. Klein, and C. L. Evans, “Click-Assembled, Oxygen-Sensing Nanoconjugates for Depth-Resolved, Near-Infrared Imaging in a 3 D Cancer Model,” *Angew. Chem. Int. Ed.*, vol. 53, no. 14, pp. 3671–3674, Apr. 2014.
- [15]M. Xu and R. R. Alfano, “Fractal mechanisms of light scattering in biological tissue and cells,” p. 3.
- [16]M. Schwertner, M. J. Booth, M. A. A. Neil, and T. Wilson, “Measurement of specimen-induced aberrations of biological samples using phase stepping interferometry,” *J. Microsc.*, vol. 213, no. 1, pp. 11–19, Jan. 2004.
- [17]R. M. Sutherland, “Cell and Environment Interactions in Tumor Microregions: The Multicell Spheroid Model,” *Sci. New Ser.*, vol. 240, no. 4849, pp. 177–184, 1988.
- [18]A. N. Bashkatov, E. A. Genina, V. I. Kochubey, V. S. Rubtsov, E. A. Kolesnikova, and V. V. Tuchin, “Optical properties of human colon tissues in the 350 – 2500 nm spectral range,” *Quantum Electron.*, vol. 44, no. 8, pp. 779–784, Aug. 2014.
- [19]H.-J. Wei, “Determination of optical properties of normal and adenomatous human colon tissues *in vitro* using integrating sphere techniques,” *World J. Gastroenterol.*, vol. 11, no. 16, p. 2413, 2005.

- [20]P. Hargrave, P. W. Nicholson, D. T. Delpy, and M. Firbank, “Optical properties of multicellular tumour spheroids,” *Phys. Med. Biol.*, vol. 41, no. 6, pp. 1067–1072, Jun. 1996.
- [21]J. F. Beek, H. J. van Staveren, P. Posthumus, H. J. C. M. Sterenborg, and M. J. C. van Gemert, “The optical properties of lung as a function of respiration,” *Phys. Med. Biol.*, vol. 42, no. 11, pp. 2263–2272, Nov. 1997.
- [22]N. Hari, P. Patel, J. Ross, K. Hicks, and F. Vanholsbeeck, “Optical coherence tomography complements confocal microscopy for investigation of multicellular tumour spheroids,” *Sci. Rep.*, vol. 9, no. 1, p. 10601, Dec. 2019.
- [23]R. Jorand *et al.*, “Deep and Clear Optical Imaging of Thick Inhomogeneous Samples,” *PLoS ONE*, vol. 7, no. 4, p. e35795, Apr. 2012.
- [24]A. Masson, P. Escande, C. Frongia, G. Clouvel, B. Ducommun, and C. Lorenzo, “High-resolution in-depth imaging of optically cleared thick samples using an adaptive SPIM,” *Sci. Rep.*, vol. 5, no. 1, p. 16898, Dec. 2015.
- [25]A. C. Rios and H. Clevers, “Imaging organoids: a bright future ahead,” *Nat. Methods*, vol. 15, no. 1, pp. 24–26, Jan. 2018.
- [26]M. A. Lancaster *et al.*, “Cerebral organoids model human brain development and microcephaly,” *Nature*, vol. 501, no. 7467, pp. 373–379, Sep. 2013.
- [27]P. R. Jamieson, J. F. Dekkers, A. C. Rios, N. Y. Fu, G. J. Lindeman, and J. E. Visvader, “Derivation of a robust mouse mammary organoid system for studying tissue dynamics,” *Development*, vol. 144, no. 6, pp. 1065–1071, Mar. 2017.
- [28]E. Leary, C. Rhee, B. T. Wilks, and J. R. Morgan, “Quantitative Live-Cell Confocal Imaging of 3D Spheroids in a High-Throughput Format,” *SLAS Technol. Transl. Life Sci. Innov.*, vol. 23, no. 3, pp. 231–242, Jun. 2018.
- [29]J. F. Dekkers *et al.*, “High-resolution 3D imaging of fixed and cleared organoids,” *Nat. Protoc.*, vol. 14, no. 6, pp. 1756–1771, Jun. 2019.
- [30]R. M. Power and J. Huisken, “A guide to light-sheet fluorescence microscopy for multiscale imaging,” *Nat. Methods*, vol. 14, no. 4, pp. 360–373, Apr. 2017.

- [31]P. J. Keller, A. D. Schmidt, J. Wittbrodt, and E. H. K. Stelzer, “Reconstruction of Zebrafish Early Embryonic Development by Scanned Light Sheet Microscopy,” *Science*, vol. 322, no. 5904, pp. 1065–1069, Nov. 2008.
- [32]A. H. Voie, D. H. Burns, and F. A. Spelman, “Orthogonal-plane fluorescence optical sectioning: Three-dimensional imaging of macroscopic biological specimens,” *J. Microsc.*, vol. 170, no. 3, pp. 229–236, Jun. 1993.
- [33]E. Fuchs, J. Jaffe, R. Long, and F. Azam, “Thin laser light sheet microscope for microbial oceanography,” *Opt. Express*, vol. 10, no. 2, p. 145, Jan. 2002.
- [34]J. Huisken, J. Swoger, F. D. Bene, J. Wittbrodt, and E. H. K. Stelzer, “Optical Sectioning Deep Inside Live Embryos by Selective Plane Illumination Microscopy,” *Science*, vol. 305, no. 5686, pp. 1007–1009, Aug. 2004.
- [35]F. C. Zanicchi *et al.*, “Live-cell 3D super-resolution imaging in thick biological samples,” *Nat. Methods*, vol. 8, no. 12, pp. 1047–1049, Dec. 2011.
- [36]B. Huang, W. Wang, M. Bates, and X. Zhuang, “Three-dimensional super-resolution imaging by stochastic optical reconstruction microscopy,” *Science*, vol. 319, no. 5864, pp. 810–813, Feb. 2008.
- [37]R. K. Chhetri, F. Amat, Y. Wan, B. Höckendorf, W. C. Lemon, and P. J. Keller, “Whole-animal functional and developmental imaging with isotropic spatial resolution,” *Nat. Methods*, vol. 12, no. 12, pp. 1171–1178, Dec. 2015.
- [38]B.-C. Chen *et al.*, “Lattice light-sheet microscopy: Imaging molecules to embryos at high spatiotemporal resolution,” *Science*, vol. 346, no. 6208, p. 1257998, Oct. 2014.
- [39]J. C. M. Gebhardt *et al.*, “Single-molecule imaging of transcription factor binding to DNA in live mammalian cells,” *Nat. Methods*, vol. 10, no. 5, pp. 421–426, May 2013.
- [40]M. Tokunaga, N. Imamoto, and K. Sakata-Sogawa, “Highly inclined thin illumination enables clear single-molecule imaging in cells,” *Nat. Methods*, vol. 5, no. 2, pp. 159–161, Feb. 2008.

- [41]E. J. Botcherby, R. Juskaitis, M. J. Booth, and T. Wilson, “Aberration-free optical refocusing in high numerical aperture microscopy,” *Opt. Lett.*, vol. 32, no. 14, pp. 2007–2009, Jul. 2007.
- [42]C. Dunsby, “Optically sectioned imaging by oblique plane microscopy,” *Opt. Express*, vol. 16, no. 25, pp. 20306–20316, Dec. 2008.
- [43]M. B. Bouchard *et al.*, “Swept confocally-aligned planar excitation (SCAPE) microscopy for high-speed volumetric imaging of behaving organisms,” *Nat. Photonics*, vol. 9, no. 2, pp. 113–119, Feb. 2015.
- [44]M. Kumar, S. Kishore, J. Nasenbeny, D. L. McLean, and Y. Kozorovitskiy, “Integrated one- and two-photon scanned oblique plane illumination (SOPi) microscopy for rapid volumetric imaging,” *Opt. Express*, vol. 26, no. 10, pp. 13027–13041, May 2018.
- [45]P. Theer, D. Dragneva, and M. Knop, “ π SPIM: high NA high resolution isotropic light-sheet imaging in cell culture dishes,” *Sci. Rep.*, vol. 6, no. 1, p. 32880, Dec. 2016.
- [46]R. Galland, G. Greci, A. Aravind, V. Viasnoff, V. Studer, and J.-B. Sibarita, “3D high- and super-resolution imaging using single-objective SPIM,” *Nat. Methods*, vol. 12, no. 7, pp. 641–644, Jul. 2015.
- [47]T. Li *et al.*, “Axial Plane Optical Microscopy,” *Sci. Rep.*, vol. 4, no. 1, p. 7253, May 2015.
- [48]T. F. Holekamp, D. Turaga, and T. E. Holy, “Fast Three-Dimensional Fluorescence Imaging of Activity in Neural Populations by Objective-Coupled Planar Illumination Microscopy,” *Neuron*, vol. 57, no. 5, pp. 661–672, Mar. 2008.
- [49]F. O. Fahrbach, F. F. Voigt, B. Schmid, F. Helmchen, and J. Huisken, “Rapid 3D light-sheet microscopy with a tunable lens,” *Opt. Express*, vol. 21, no. 18, p. 21010, Sep. 2013.
- [50]O. E. Olarte, J. Andilla, D. Artigas, and P. Loza-Alvarez, “Decoupled illumination detection in light sheet microscopy for fast volumetric imaging,” *Optica*, vol. 2, no. 8, p. 702, Aug. 2015.

- [51]J. Huisken and D. Y. R. Stainier, “Even fluorescence excitation by multidirectional selective plane illumination microscopy (mSPIM),” *Opt. Lett.*, vol. 32, no. 17, pp. 2608–2610, Sep. 2007.
- [52]U. Krzic, S. Gunther, T. E. Saunders, S. J. Streichan, and L. Hufnagel, “Multiview light-sheet microscope for rapid in toto imaging,” *Nat. Methods*, vol. 9, no. 7, pp. 730–733, Jul. 2012.
- [53]R. Tomer, K. Khairy, F. Amat, and P. J. Keller, “Quantitative high-speed imaging of entire developing embryos with simultaneous multiview light-sheet microscopy,” *Nat. Methods*, vol. 9, no. 7, pp. 755–763, Jul. 2012.
- [54]J. M. Murray, P. L. Appleton, J. R. Swedlow, and J. C. Waters, “Evaluating performance in three-dimensional fluorescence microscopy,” *J. Microsc.*, vol. 228, no. 3, pp. 390–405, Dec. 2007.
- [55]F. O. Fahrbach and A. Rohrbach, “A line scanned light-sheet microscope with phase shaped self-reconstructing beams,” *Opt. Express*, vol. 18, no. 23, p. 24229, Nov. 2010.
- [56]T. A. Planchon *et al.*, “Rapid three-dimensional isotropic imaging of living cells using Bessel beam plane illumination,” *Nat. Methods*, vol. 8, no. 5, pp. 417–423, May 2011.
- [57]M. A. A. Neil, R. Juškaitis, and T. Wilson, “Method of obtaining optical sectioning by using structured light in a conventional microscope,” *Opt. Lett.*, vol. 22, no. 24, p. 1905, Dec. 1997.
- [58]L. Gao *et al.*, “Noninvasive Imaging beyond the Diffraction Limit of 3D Dynamics in Thickly Fluorescent Specimens,” *Cell*, vol. 151, no. 6, pp. 1370–1385, Dec. 2012.
- [59]P. J. Keller, “In vivo imaging of zebrafish embryogenesis,” *Methods*, vol. 62, no. 3, pp. 268–278, Aug. 2013.
- [60]F. Wang *et al.*, “Light-sheet microscopy in the near-infrared II window,” *Nat. Methods*, vol. 16, no. 6, pp. 545–552, Jun. 2019.
- [61]T. V. Truong, W. Supatto, D. S. Koos, J. M. Choi, and S. E. Fraser, “Deep and fast live imaging with two-photon scanned light-sheet microscopy,” *Nat. Methods*, vol. 8, no. 9, pp. 757–760, Sep. 2011.

- [62]O. E. Olarte *et al.*, “Image formation by linear and nonlinear digital scanned light-sheet fluorescence microscopy with Gaussian and Bessel beam profiles,” *Biomed. Opt. Express*, vol. 3, no. 7, p. 1492, Jul. 2012.
- [63]I. Newton, *Opticks Or, A Treatise of the Reflections, Refractions, Inflections, and Colours of Light*. 1730.
- [64]J. W. Hardy, “Active optics: A new technology for the control of light,” *Proc. IEEE*, vol. 66, no. 6, pp. 651–697, Jun. 1978.
- [65]R. N. Wilson, F. Franza, and L. Noethe, “Active Optics,” *J. Mod. Opt.*, vol. 34, no. 4, pp. 485–509, Apr. 1987.
- [66]H. W. Babcock, “The Possibility of Compensating Astronomical Seeing,” *Publ. Astron. Soc. Pac.*, vol. 65, p. 229, Oct. 1953.
- [67]M. J. Booth and T. Wilson, “Refractive-index-mismatch induced aberrations in single-photon and two-photon microscopy and the use of aberration correction,” *J. Biomed. Opt.*, vol. 6, no. 3, p. 266, 2001.
- [68]M. J. Booth, M. A. A. Neil, R. Juskaitytis, and T. Wilson, “Adaptive aberration correction in a confocal microscope,” *Proc. Natl. Acad. Sci.*, vol. 99, no. 9, pp. 5788–5792, Apr. 2002.
- [69]O. Azucena *et al.*, “Adaptive optics wide-field microscopy using direct wavefront sensing,” *Opt. Lett.*, vol. 36, no. 6, p. 825, Mar. 2011.
- [70]L. Sherman, J. Y. Ye, O. Albert, and T. B. Norris, “Adaptive correction of depth-induced aberrations in multiphoton scanning microscopy using a deformable mirror,” *J. Microsc.*, vol. 206, no. 1, pp. 65–71, Apr. 2002.
- [71]D. Débarre, E. J. Botcherby, T. Watanabe, S. Srinivas, M. J. Booth, and T. Wilson, “Image-based adaptive optics for two-photon microscopy,” *Opt. Lett.*, vol. 34, no. 16, p. 2495, Aug. 2009.
- [72]R. Aviles-Espinosa *et al.*, “Measurement and correction of in vivo sample aberrations employing a nonlinear guide-star in two-photon excited fluorescence microscopy,” *Biomed. Opt. Express*, vol. 2, no. 11, p. 3135, Nov. 2011.

- [73]K. Wang, W. Sun, C. T. Richie, B. K. Harvey, E. Betzig, and N. Ji, “Direct wavefront sensing for high-resolution in vivo imaging in scattering tissue,” *Nat. Commun.*, vol. 6, no. 1, p. 7276, Nov. 2015.
- [74]T. J. Gould, D. Burke, J. Bewersdorf, and M. J. Booth, “Adaptive optics enables 3D STED microscopy in aberrating specimens,” *Opt. Express*, vol. 20, no. 19, pp. 20998–21009, Sep. 2012.
- [75]K. F. Tehrani and P. Kner, “Point spread function optimization for STORM using adaptive optics,” in *MEMS Adaptive Optics VIII*, 2014, vol. 8978, p. 89780I.
- [76]B. Thomas, A. Wolstenholme, S. N. Chaudhari, E. T. Kipreos, and P. Kner, “Enhanced resolution through thick tissue with structured illumination and adaptive optics,” *J. Biomed. Opt.*, vol. 20, no. 2, p. 026006, Feb. 2015.
- [77]C. Bourgenot, C. D. Saunter, J. M. Taylor, J. M. Girkin, and G. D. Love, “3D adaptive optics in a light sheet microscope,” *Opt. Express*, vol. 20, no. 12, p. 13252, Jun. 2012.
- [78]D. Wilding, P. Pozzi, O. Soloviev, G. Vdovin, and M. Verhaegen, “Adaptive illumination based on direct wavefront sensing in a light-sheet fluorescence microscope,” *Opt. Express*, vol. 24, no. 22, p. 24896, Oct. 2016.
- [79]A. Hubert *et al.*, “Adaptive optics light-sheet microscopy based on direct wavefront sensing without any guide star,” *Opt. Lett.*, vol. 44, no. 10, p. 2514, May 2019.
- [80]T.-L. Liu *et al.*, “Observing the cell in its native state: Imaging subcellular dynamics in multicellular organisms,” *Science*, vol. 360, no. 6386, p. eaaq1392, Apr. 2018.
- [81]J. Schöneberg *et al.*, “4D cell biology: big data image analytics and lattice light-sheet imaging reveal dynamics of clathrin-mediated endocytosis in stem cell-derived intestinal organoids,” *Mol. Biol. Cell*, vol. 29, no. 24, pp. 2959–2968, Nov. 2018.
- [82]B. C. Platt and R. Shack, “History and Principles of Shack-Hartmann Wavefront Sensing,” *J. Refract. Surg.*, vol. 17, no. 5, pp. S573–S577, Sep. 2001.

- [83]S. Thomas, T. Fusco, A. Tokovinin, M. Nicolle, V. Michau, and G. Rousset, “Comparison of centroid computation algorithms in a Shack-Hartmann sensor: Comparison of centroid computation algorithms,” *Mon. Not. R. Astron. Soc.*, vol. 371, no. 1, pp. 323–336, Aug. 2006.
- [84]R. Navarro, J. Arines, and R. Rivera, “Direct and inverse discrete Zernike transform,” *Opt. Express*, vol. 17, no. 26, p. 24269, Dec. 2009.
- [85]D. Ramos-López, M. A. Sánchez-Granero, M. Fernández-Martínez, and A. Martínez-Finkelshtein, “Optimal sampling patterns for Zernike polynomials,” *Appl. Math. Comput.*, vol. 274, pp. 247–257, Feb. 2016.
- [86]T. R. Rimmele and R. R. Radick, “Solar adaptive optics at the National Solar Observatory,” presented at the Astronomical Telescopes & Instrumentation, Kona, HI, 1998, p. 72.
- [87]V. Michau *et al.*, “Shack-Hartmann wavefront sensing with extended sources,” presented at the SPIE Optics + Photonics, San Diego, California, USA, 2006, p. 63030B.
- [88]N. Träber *et al.*, “Polyacrylamide Bead Sensors for *in vivo* Quantification of Cell-Scale Stress in Zebrafish Development,” *Biophysics*, preprint, Sep. 2018.
- [89]X. Tao *et al.*, “Live imaging using adaptive optics with fluorescent protein guide-stars,” *Opt. Express*, vol. 20, no. 14, p. 15969, Jul. 2012.
- [90]X. Tao, O. Azucena, M. Fu, Y. Zuo, D. C. Chen, and J. Kubby, “Adaptive optics confocal microscopy using fluorescent protein guide-stars for brain tissue imaging,” presented at the SPIE MOEMS-MEMS, San Francisco, California, USA, 2012, p. 82530M.
- [91]M. N. Malakhov, V. F. Matiukin, and B. V. Prilepskii, “Estimating the parameters of a multielement mirror of an adaptive optical system,” *Sov. J. Opt. Technol.*, vol. 51, pp. 16–18, Mar. 1984.
- [92]J. W. Hardy, “Instrumental Limitations In Adaptive Optics For Astronomy,” in *Active Telescope Systems*, 1989, vol. 1114, pp. 2–13.

- [93]W. G. Hulburd, T. K. Barrett, E. L. Cuellar, and D. G. Sandler, “High-bandwidth long-stroke segmented mirror for atmospheric compensation,” presented at the San Diego - DL tentative, San Diego, CA, 1992, p. 64.
- [94]B. Hulburd, “Segmented Mirrors For Atmospheric Compensation,” in *New Technologies for Astronomy*, 1989, vol. 1130, pp. 42–51.
- [95]M. Yellin, “Using Membrane Mirrors In Adaptive Optics,” presented at the 1976 SPIE/SPSE Technical Symposium East, Reston, 1976, pp. 97–102.
- [96]S. Bonora and L. Poletto, “Push-pull membrane mirrors for adaptive optics,” *Opt. Express*, vol. 14, no. 25, pp. 11935–11944, Dec. 2006.
- [97]A. H. Seilly, “HELENOID Actuators-A New Concept in Extremely Fast Acting Solenoids,” presented at the 1979 Automotive Engineering Congress and Exposition, 1979, p. 790119.
- [98]T. Andersen, M. Owner-Petersen, A. Ardeberg, and T. Korhonen, “A new concept for large deformable mirrors for extremely large telescopes,” presented at the SPIE Astronomical Telescopes + Instrumentation, Orlando, Florida , USA, 2006, p. 62720Y.
- [99]E. Steinhaus and S. G. Lipson, “Bimorph piezoelectric flexible mirror,” *J. Opt. Soc. Am.*, vol. 69, no. 3, p. 478, Mar. 1979.
- [100] T. Kanda, K. F. Sullivan, and G. M. Wahl, “Histone–GFP fusion protein enables sensitive analysis of chromosome dynamics in living mammalian cells,” *Curr. Biol.*, vol. 8, no. 7, pp. 377–385, Mar. 1998.
- [101] G. Chen, H. Qiu, P. N. Prasad, and X. Chen, “Upconversion Nanoparticles: Design, Nanochemistry, and Applications in Theranostics,” *Chem. Rev.*, vol. 114, no. 10, pp. 5161–5214, May 2014.
- [102] S. Wu *et al.*, “Non-blinking and photostable upconverted luminescence from single lanthanide-doped nanocrystals,” *Proc. Natl. Acad. Sci.*, vol. 106, no. 27, pp. 10917–10921, Jul. 2009.
- [103] Y. I. Park, K. T. Lee, Y. D. Suh, and T. Hyeon, “Upconverting nanoparticles: a versatile platform for wide-field two-photon microscopy and multi-modal in vivo imaging,” *Chem. Soc. Rev.*, vol. 44, no. 6, pp. 1302–1317, 2015.

- [104] K. Shin, Y. Song, Y. Goh, and K. Lee, “Two-Dimensional and Three-Dimensional Single Particle Tracking of Upconverting Nanoparticles in Living Cells,” *Int. J. Mol. Sci.*, vol. 20, no. 6, p. 1424, Mar. 2019.
- [105] L. Muzi, F. Tardani, C. L. Mesa, A. Bonincontro, A. Bianco, and G. Risuleo, “Interactions and effects of BSA-functionalized single-walled carbon nanotubes on different cell lines,” *Nanotechnology*, vol. 27, no. 15, p. 155704, Feb. 2016.
- [106] F. O. Fahrbach, V. Gurchenkov, K. Alessandri, P. Nassoy, and A. Rohrbach, “Light-sheet microscopy in thick media using scanned Bessel beams and two-photon fluorescence excitation,” *Opt. Express*, vol. 21, no. 11, p. 13824, Jun. 2013.

Appendix 1: Detailed list of the optical elements of $w_{AO}SPIM$

This appendix provides further detail about the components of $w_{AO}SPIM$ that the reader might find useful.

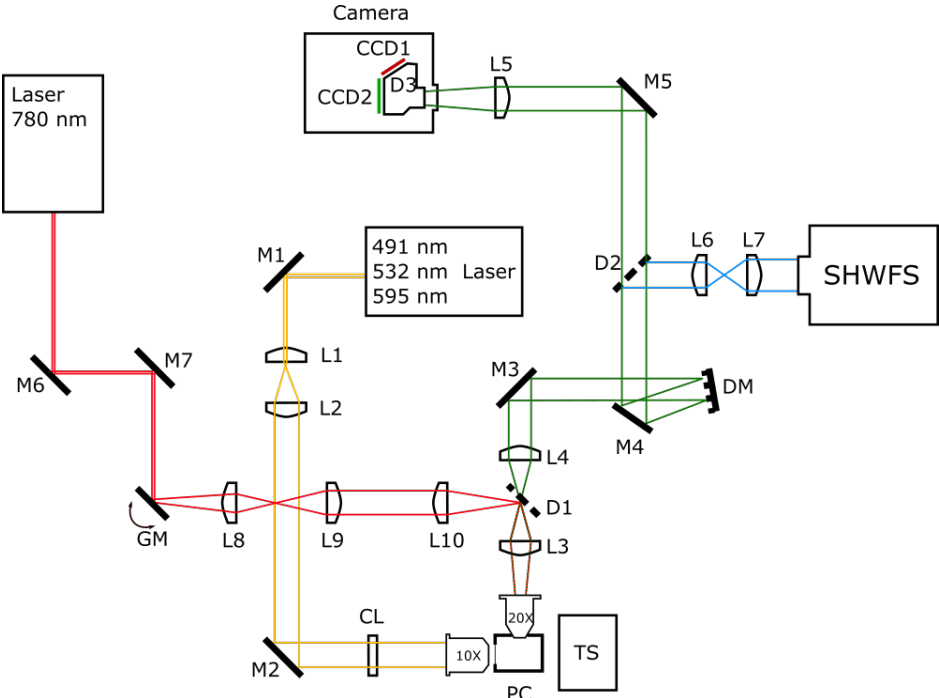


Figure A1-1: $w_{AO}SPIM$ sketch for reference.

Table A1-2: Lenses

Lens	Focal distance (mm)	Type	Model	Manufacturer
L1	-25,4	Biconvex	LD2297-A	Thorlabs
L2	200	Achromatic	AC254-200-A-ML	Thorlabs
L3	100	Achromatic	AC254-100-A-ML	Thorlabs
L4	150	Achromatic	AC254-150-A-ML	Thorlabs
L5	300	Achromatic	AC254-300-A-ML	Thorlabs
L6	150	Achromatic	AC254-150-A-ML	Thorlabs
L7	75	Biconvex	LB1910-A	Thorlabs
L8	50	Air-Spaced Achromatic	ACA254-050-A-ML	Thorlabs
L9	100	Achromatic	AC254-100-A-ML	Thorlabs
L10	40	Achromatic	AC254-040-A-ML	Thorlabs
CL	100	Cylindrical	LJ1567L1-A	Thorlabs

Table A1-2: Other elements

Element	Model	Manufacturer
D1	FF746-SDi01	Semrock
D2	FF520-Di02	Semrock
DM	Mirao 52-e	Imagine Optic
10X, 0.25 NA objective		Leica Microsystems
20X, 0.5 NA objective		Leica Microsystems

Appendix 2: *Methods and Protocols*
publication

Article

Highly Sensitive Shack–Hartmann Wavefront Sensor: Application to Non-Transparent Tissue Mimic Imaging with Adaptive Light-Sheet Fluorescence Microscopy

Javier Morgado Brajones ¹, Gregory Clouvel ² , Guillaume Dovillaire ², Xavier Levecq ² and Corinne Lorenzo ^{1,*}¹ ITAV, Université de Toulouse, CNRS, 31106 Toulouse, France² Imagine Optic, 91400 Orsay, France

* Correspondence: corinne.lorenzo@itav.fr

Received: 10 May 2019; Accepted: 8 July 2019; Published: 11 July 2019



Abstract: High-quality in-depth imaging of three-dimensional samples remains a major challenge in modern microscopy. Selective plane illumination microscopy (SPIM) is a widely used technique that enables imaging of living tissues with subcellular resolution. However, scattering, absorption, and optical aberrations limit the depth at which useful imaging can be done. Adaptive optics (AOs) is a method capable of measuring and correcting aberrations in different kinds of fluorescence microscopes, thereby improving the performance of the optical system. We have incorporated a wavefront sensor adaptive optics scheme to SPIM ($W_{AO}SPIM$) to correct aberrations induced by optically-thick samples, such as multi-cellular tumor spheroids (MCTS). Two-photon fluorescence provides us with a tool to produce a weak non-linear guide star (NGS) in any region of the field of view. The faintness of NGS; however, led us to develop a high-sensitivity Shack–Hartmann wavefront sensor (SHWS). This paper describes this newly developed SHWS and shows the correction capabilities of $W_{AO}SPIM$ using NGS in thick, inhomogeneous samples like MCTS. We report improvements of up to 79% for spatial frequencies corresponding to cellular and subcellular size features.

Keywords: light-sheet fluorescence microscopy; adaptive optics; highly-sensitive Shack–Hartmann; tissue mimics

1. Introduction

In recent years, tissue mimics (TMs) such as microtissues, spheroids, and organoid cultures have become increasingly important in life-science research, as they provide a physiologically more relevant environment for cell growth, tissue morphogenesis, and stem cell differentiation. Selective plane illumination microscopy (SPIM), the most prevalent light-sheet fluorescence microscope, is a sine qua non tool today to understand cell biology in these TMs. Yet, due to their thick, inhomogeneous, and high light-scattering properties, observing TMs at high resolution, in-depth, and in real time remains a major technical challenge. While SPIM is recognized as a very powerful and promising tool for imaging such samples [1], it still suffers from various specific limitations. Indeed, scattering, but also absorption and optical aberrations, limit the depth to which useful imaging can be done. Moreover, in these biological samples, refractive index differences in and between cells are the main source of optical aberrations [1–3]. Overall, these effects severely limit SPIM for imaging deep within complex heterogeneous opaque TMs, typically beyond 50–100 μm .

Previous approaches to improve in-depth image quality include the use of adaptive optics (AOs). Originally developed for astronomical telescopes, AOs is a method capable of measuring and correcting

optical aberrations, thereby improving performance of the optical system. In direct wavefront sensing configurations, it does so by introducing a sensor, such as a Shack–Hartmann wavefront sensor (SHWS), that measures the distorted wavefront coming from an ideal point source emitter. In astronomy, this point source emitter can be a well-known star (a “guide star”) or the fluorescence produced when focusing a powerful pulsed laser into the atmosphere (artificial guide star). The guide star must be smaller than the diffraction limit defined by an SHWS microlens, and its emitted fluorescence must generate enough photons to provide the required signal-to-noise ratio for accurate wavefront measurements. From the wavefront measurement, a corrective element, such as a deformable mirror (DM), compensates for the optical aberrations by means of a feedback loop (e.g., a closed-loop).

Over the past decade, AOs has been increasingly used in microscopy and has proven a valuable tool for correcting aberrations in different kinds of fluorescence microscopes, such as confocal [4], two-photon fluorescence [5], structured illumination [6], and lattice light-sheet microscopes [7]. Wavefront sensor-less AOs has also been implemented in several microscope modalities [8,9], including light-sheet microscopy [10]. Previously, we successfully applied a SHWS-AOs scheme using fluorescent beads as guide stars [3] to use with SPIM ($w_{AO}SPIM$) to correct complex aberrations induced by the TM itself. The same setup was also used to compensate for aberrations arising from refractive index mismatches induced by optical clearing methods [10]. Direct wavefront measurements using an SHWS in biological samples remain difficult since the latter do not display natural point source references, as do the guide stars used in astronomy.

In Jorand and coworkers [3], we addressed this issue by using bright 2.5 μm fluorescent beads directly inserted into the sample as suitable fluorescence point source references. This method enabled us to measure the aberrations induced by multi-cellular tumor spheroids (MCTS) and to compensate for them using closed-loop AOs. MCTS are TM models that are highly useful in investigating the influence of malignant cell interactions during cell proliferation [11]. Due to their opacity and density; however, they raise significant challenges for imaging by light microscopy [12]. Even if, in our case, the inserted fluorescence beads did not seem to alter the MCTS growth, they can disturb cell behavior within MCTS and; thus, the natural MCTS architecture. These possible effects need to be considered for live 3D imaging experiments. Moreover, spatial variations of aberrations within such inhomogeneous, non-transparent samples result in major changes to the light path and limit the quality of AOs correction outside a small region around the guide star—the isoplanetic patch. Guide star placement; therefore, plays a critical role in the AOs process. Bead placement inside living samples is random and intrusive [13], and requires the use of a pinhole limiting the usefulness of the correction.

To overcome these difficulties and to provide a minimally-invasive and more versatile approach, Aviles-Espinosa [8] and Wang [14] proposed the use of a non-linear guide star (NGS) that was successfully applied to confocal [15] and lattice light-sheet microscopes [7]. However, in samples such as MCTS, the NGS fluorescence light reaching the sensor is weak and often limits the accuracy of the wavefront measurement and; therefore, the efficiency of the correction. Indeed, light scattering drastically reduces the number of ballistic photons forming the NGS image, making it impossible to accurately measure aberrations with an SHWS coupled with a CCD sensor (as in our previous work). Speed of image acquisition with correction is limited by exposure time and by sampling requirements to accurately measure the wavefront from the guide star. Therefore, in live 3D imaging experiments where phototoxicity and speed are critical, the use of an NGS in combination with an SHWS coupled with a CCD sensor rapidly reaches its limits. Electron multiplying CCD (EMCCD) sensors offer high sensitivity and very low read-out noise, making them an ideal choice in this context. Recently, EMCCD-based SHWFS have been successfully employed in correcting sample-induced aberrations [7]. However, little detail has been published about the practical considerations of developing and using an EMCCD-based SHWFS. We have developed a high-sensitivity EMCCD-based SHWFS suitable for NGS and compatible with live 3D TM imaging studies. To be able to work with minimal light, the SHWFS development focused on photon collection efficiency, optimizing the microlens array to maximize

photon flux in each sub-pupil of the sensor. A complete description of our sensor is presented in this article.

In optically-thick TMs, the loss of signal-to-background ratio due to scattering defines the maximum depth at which useful corrections can be made. Previous applications of AOs in lattice light-sheet microscopy show image quality improvements up to 30 μm deep [10] when imaging organoids. However, conventional light-sheet microscopy systems, including our own, typically entail imaging larger volumes, comprising larger fields of view, and requiring correction at greater depths. By coupling our WAO SPIM with an EMCCD-based SHWFS specifically designed for TM imaging, we demonstrate the in-depth correction capabilities in MCTS up to 120 μm deep.

2. Materials and Methods

2.1. Experimental Setup

Laser lines were generated using a compact laser launch (Errol). Laser beams of 491, 532, and 595 nm were generated and merged into a single beam. An acousto-optic tunable filter allowed for precise control over the illumination intensity of each beam.

The output beam was collimated and expanded by means of a telescope. A cylindrical lens generated the light-sheet which was focused into the sample with a 10×0.25 NA air objective (Leica Microsystems). The light-sheet thickness was 2.02 μm at the waist, with a Rayleigh range of 21.54 μm . Fluorescence light was collected by a 20×0.5 NA water immersion objective (Leica Microsystems) and expanded by telescope. The back-pupil plane of the telescope was conjugated with a Mirao 52-e DM (Imagine Optic, Orsay, France). The wavefront was measured using an SHWS made of a 14×14 microlens array and a Photometrics Evolve 512 EMCCD camera. In order to correct imaging path aberrations, the SHWS was first placed on the detection path. In this position, the wavefront was corrected to a plane wavefront, and the shape of the mirror was recorded. After correction, the SHWS was placed perpendicularly to the detection path. A dichroic beamsplitter (model FF520-Di02 Semrock, Rochester, NY, USA) directed the 350–512 nm wavelengths to the SHWS while allowing the 528–950 nm wavelengths to reach the ORCA-D2 camera (Hamamatsu Photonics, Hamamatsu, Japan). The camera itself allowed for dual imaging in 641 (CCD1) and 520 nm (CCD2) wavelengths.

A 780 nm femtosecond laser (Toptica Photonics, Gräfelfing, Germany) was directed to the sample by a pair of galvanometric mirrors. The galvanic mirrors were conjugated with the back-pupil plane of the detection objective. A dichroic mirror (model FF746-SDi01, Semrock, Rochester, NY, USA) made it possible to insert the infrared beam into the detection path, while the beam was focused into the sample by the detection objective. The sample was placed in the light-sheet inside a physiological chamber filled with aqueous solution. A moving stage enabled precise three-dimensional placement of the sample (Figure 1).

In WAO SPIM , dichroic beamsplitters D1 and D2 introduce significant aberrations, mostly astigmatism and coma. To compensate for these optically-induced aberrations, the latter were measured by placing the SHWS in the imaging camera focal plane. We could then set the DM shape ("AOs off" in the text) so that it corrected imaging path aberrations. By repositioning the SHWS in its dedicated path, we measured a reference wavefront corresponding to the differential aberrations between the imaging and the SHWS path. This reference wavefront was henceforth used as a target for all AOs corrections.

The optical system was driven by WaveSuite software (Imagine Optic) and custom-made AMISPM software.

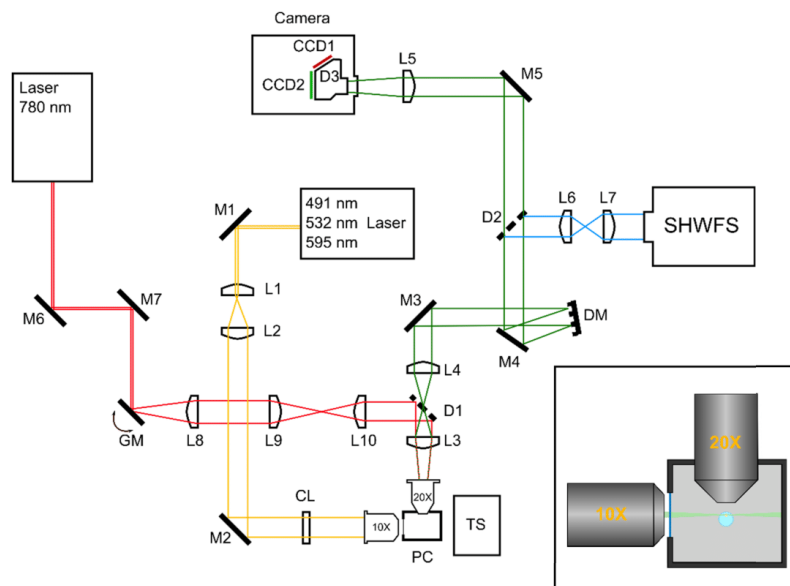


Figure 1. (left) Schematic image of the $wAOSPIM$ system. L1–10: Lenses; M1–7: Mirrors; D1–3: Dichroic beamsplitters; CL: Cylindrical lens; DM: Deformable mirror; SHWFS: Shack–Hartmann wavefront sensor; GM: Pair of galvanic mirrors; PC: Physiological chamber; TS: Translation stage. (right) Top-down view of the sample mounting scheme. The sample is placed inside an agarose cylinder that hangs from a movable stage. The physiological chamber is filled with an aqueous solution.

2.2. Cell Culture and MCTS Production

HCT116-H2BFP/ArrestRed cells were cultured in DMEM+GlutaMAX (Dulbecco's modified eagle medium; Thermo Fisher Scientific, Waltham, MA, USA), supplemented with 10% fetal bovine serum and 1% penicillin–streptomycin (Pen Strep; Gibco), and maintained at 37 °C with 5% CO₂ in an incubator. To produce the MCTS, we used the centrifugation method described in [16]. MCTS were prepared in ultra-low attachment 96-well plates (Costar). Cells were plated at a density of 1000 cells/well in 150 μ L cell culture medium per well, and then centrifuged to enable MCTS formation. After three to four days of growth, MCTS of 300 μ m in diameter were collected, washed three times with PBS, before being fixed with 10% neutral buffered formalin (Sigma-Aldrich) at room temperature for two hours.

2.3. Sample Preparation

2.5 μ m fluorescent beads (Invitrogen Inspeck Green 505/515 100% relative intensity) and MCTS were embedded in 1.3% agarose (Euromedex low melting point) inside 100 μ L capillary pipettes (Hirschmann Ringcaps).

2.4. Image Processing

Images were processed with open-source image-processing Fiji software and custom MATLAB scripts. Image quality assessment (spatial frequency comparison) Matlab codes are available on request.

3. Results

3.1. Wavefront Sensor

Our SHWS is based on a Photometrics Evolve 512 EMCCD camera. With a quantum efficiency greater than 0.9 in the visible range, EMCCD technology provides the most sensitive sensors available. The sensor's electromagnetic gain can be tuned in real time allowing a trade-off between exposure time and signal-to-noise ratio. These characteristics make EMCCD a versatile tool when working with a low photon budget, and a good candidate for a high sensitivity wavefront sensor. The Evolve 512 EMCCD camera has a 1–300 EM gain range.

Wavefront measurement error depends on photon flux and EM gain. Wavefront reconstruction in a SHWS is based on the correct centroid calculation of the Shack–Hartmann spots and thus amplification of noise, if too strong, may introduce errors. We modeled the wavefront error as a function of photon flux and EM gain. This analysis concludes that we need at least 2×10^5 photons for an optimal wavefront measurement (Figure 2). With 2×10^5 photons and a gain of 10 or more, the wavefront error is kept below 7 nm. Additionally, using a gain of 300 allows us to work with less than 5×10^4 while maintaining error of less than 10 nm.

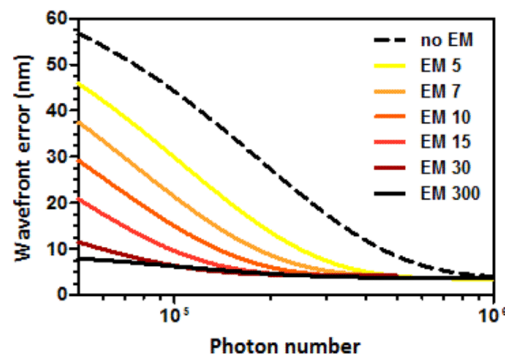


Figure 2. Simulated wavefront error as a function of the total number of photons arriving at the sensor.

Wavefront sensor design is a multiparameter problem leading to a compromise between different variables concerning the microlens matrix design (focal length, size, distribution) and camera specifications (pixel size, CCD surface). All of these parameters must be finely tuned to be able to measure local wavefront slopes according to the application requirements. Table 1 presents details of the sensor properties. The most significant aberrations in SPIM for MCTS imaging with minimized refractive index mismatch conditions, due to the sample itself, can be decomposed primarily as astigmatism, coma, and spherical aberrations themselves. To help define optimal wavefront sensor design, we performed a simulation (data not shown) of the wavefront measurement dynamic and accuracy as a function of the number of microlenses and photon flux. Wavefront correction error is dependent on both the wavefront measurement and wavefront modulation errors. To ensure accurate wavefront correction by the DM, wavefront measurement error must be kept smaller than the modulation error (for the Mirao 52-e mirror, no more than 20 nm rms, cf. Mirao 52-e specification sheet). This accuracy must be kept constant for different levels of aberrations to obtain reliable correction quality. A tradeoff must, therefore, be made between the necessary photon flux and the sensor-measured amplitude of the aberrations: When compared to conventional SHWS design typically used in metrology, the numerical aperture of the microlenses was slightly increased (~25%) in order to boost photon collection efficiency, while, as a consequence, spatial sampling was slightly decreased. Based on previous MCTS experiments, we evaluated that a 3 μm peak-to-valley dynamic range is

necessary on the third-order spherical aberration (Z_4^0) for a 555 nm wavelength. Using these criteria, a 14×14 microlens array is able to provide optimized wavefront reconstruction. Figure 3 presents an evaluation of the sensor dynamic range.

Table 1. Technical characteristics of our Shack-Hartmann Wavefront Sensor.

Aperture Dimension (mm ²)	7.73 × 7.73
Number of microlenses (μm)	14 × 14
Microlens step (μm)	0.552
Focus dynamic range (mm)	24.1
Wavefront dynamic on Z_0^4	5.4 λ
Photon number for optimal accuracy	200,000
Wavefront measurement accuracy	λ/70
Working wavelength range (nm)	400–800
Readout speed (MHz)	5
Electron-Multiplying gain	1–300

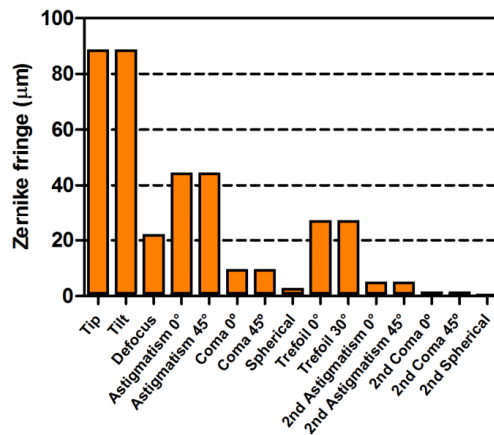


Figure 3. Simulated dynamic range of wavefront reconstruction.

3.2. System Performance

We first measured the performance of our system by evaluating its correction capabilities using fluorescent beads in a transparent environment. We directly measured RMS aberrations and calculated the Strehl ratio using the Maréchal approximation. To evaluate the amount of light reaching the sensor, the number of photons was estimated from the physical properties of the sensor as follows:

$$N_{photons} = \frac{I_{signal} \cdot CG}{EMG \cdot QE}$$

where $N_{photons}$ is the number of signal photons over the pupil, I_{signal} is the sum of the pixel value over the image after removing background, CG is the conversion gain of the sensor, EMG is the electromagnetic gain applied, and QE is the quantum efficiency of the sensor.

Green fluorescent beads were suspended in agarose inside a glass capillary. The latter acted as a source of aberration, whose main component was astigmatism and to a lesser extent trefoil and first order coma. The bead image appears significantly distorted in lateral and axial directions (Figure 4).

The image was correctly restored after AOs. RMS error was reduced from $0.238 \pm 0.014 \mu\text{m}$ to $0.011 \pm 0.001 \mu\text{m}$, and the Strehl ratio improved from 0.007 ± 0.021 to 0.983 ± 0.005 after correction.

Contrast was improved by an average $80\% \pm 29\%$ (peak signal to background). Full width at half maximum (FWHM) values before and after correction are shown in Table 2. Note that FWHM_z depends on the thickness and optimal placement of the light-sheet and thus does not improve.

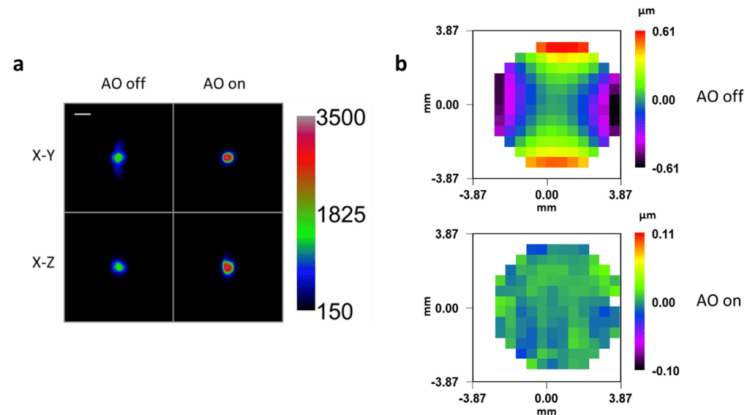


Figure 4. (a) Maximum intensity projection of green fluorescent beads embedded in 1% agarose and imaged through a capillary glass at a depth of $100\ \mu\text{m}$, both before and after Adaptive Optics (AO) correction. Scale bar: $5\ \mu\text{m}$. Beads were illuminated with constant intensity at $491\ \text{nm}$. (b) Measured wavefronts before and after correction, offset by the reference wavefront corresponding to an aberration-free system.

Table 2. Mean Full width at half maximum (FWHM), root mean square aberration (RMS), and Strehl ratio (SR) values for beads before and after correction.

	AOs off	AOs on
$\text{FWHM}_x\ (\mu\text{m})$	3.376	2.607
$\text{FWHM}_y\ (\mu\text{m})$	4.679	2.426
$\text{FWHM}_z\ (\mu\text{m})$	3.486	3.781
RMS (μm)	0.238	0.011
SR	0.007	0.983

In order to determine the lowest limit in light intensity necessary to perform correction, fluorescent beads were placed inside glass capillaries and imaged at $100\ \mu\text{m}$ in a similar manner as described above, with decreasing illumination intensity. During experiments, emission intensity was measured as a fraction of the saturation value of the SHWS, defined as the maximum readable intensity for each pixel. The number of captured photons was later calculated from the acquired SHWS images. Corrected images typically nearly reached the diffraction limit ($SR > 0.8$) (Figure 5). Good corrections were obtained with as few as 12×10^3 signal photons over the pupil, with correction performance increasing with intensity. For intensities below 12×10^3 photons (6.6% of SHWS saturation value), our software failed to measure wavefront aberrations, making it impossible to correct the image. Beyond that limit, corrections typically allowed for imaging near the diffraction limit. Four closed loop iterations were necessary for good correction in low intensity conditions (8% of SHWS saturation value, 14.5×10^3 to 16.5×10^3 signal photons), while three were enough under high intensity conditions (90% of SHWS saturation value, 290×10^3 to 305×10^3 signal photons) (Table 3, Figure 5).

Table 3. Mean correction results for different emission intensities.

	AOs on			
	7% ¹	8%	9%	10%
FWHM _X (μm)	2.672 ± 0.019	2.695 ± 0.016	2.686 ± 0.018	2.682 ± 0.018
FWHM _Y (μm)	2.343 ± 0.030	2.230 ± 0.045	2.277 ± 0.030	2.281 ± 0.025
FWHM _Z (μm)	3.491 ± 0.073	3.483 ± 0.065	3.495 ± 0.070	3.540 ± 0.063
RMS (μm)	0.025 ± 0.002	0.016 ± 0.001	0.014 ± 0.001	0.013 ± 0.001
SR	0.909 ± 0.011	0.961 ± 0.003	0.969 ± 0.003	0.973 ± 0.002

¹ Intensity was measured as a fraction of the saturation intensity of the sensor. Wavefront information was acquired at 100 ms exposure time and EM gain of 300. Fifteen iterations were used to perform the corrections. Illumination intensity was adjusted on a case-by-case basis to achieve the desired emission intensity.

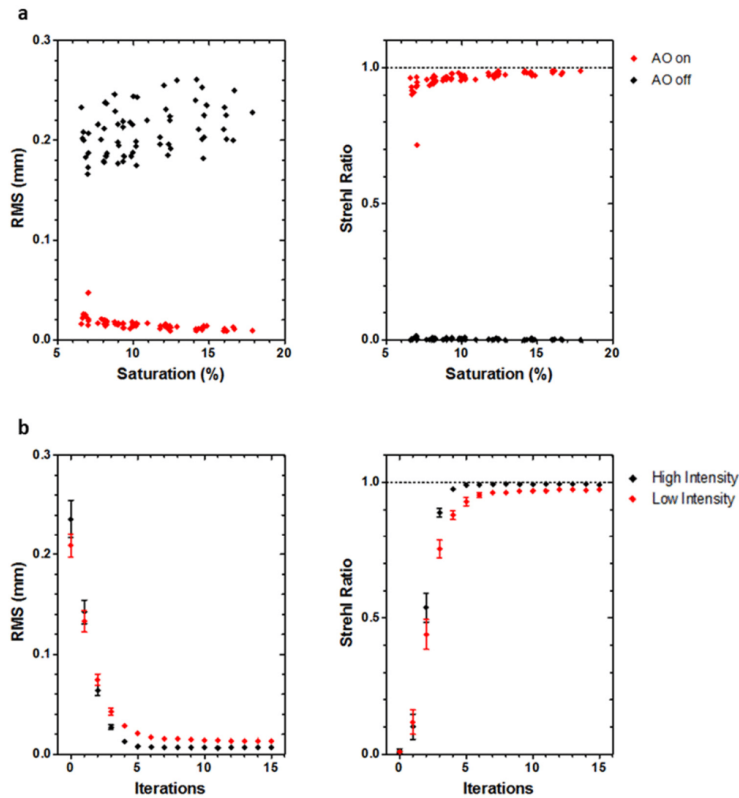


Figure 5. (a) RMS and Strehl ratio values of wavefronts before (AOs off) and after (AOs on) correction for a range of light conditions. Each pair of points (off and on) corresponds to a different fluorescent bead. (b) SR and RMS values after correction as a function of the number of iterations used in the closed loop, for both low (8% saturation) and high (90% saturation) emission intensity.

3.3. MCTS Imaging

To evaluate the ability of $W_{AO}SPIM$ to correct aberration within MCTS, we used MCTS prepared from the HCT116 cell line expressing H2B-GFP and ArrestRed (H2B-tKR, Evrogen, Moscow, Russia) histones, and fixed at approximately 300 μm size. The ArrestRed fluorophore was used for imaging purposes, while GFP was used for NGS generation. Image quality improvements were quantitatively

assessed in terms of spatial frequency using a frequency metric presented in Masson and coworkers [10]. Frequencies were evaluated by integrating concentric rings into the Fourier space, thereby obtaining a radial frequency distribution. This process was carried out for before and after correction images in order to assess improvements in frequencies corresponding to features of cellular and subcellular size.

Although fluorescent beads are effective tools in characterizing the correction capability of our microscope, their usefulness is severely limited in living samples due to random spatial placement and intrusiveness. To overcome this limitation, an NGS was generated by excitation of the H2B-GFP nuclear protein by a 780 nm femtosecond laser.

Firstly, we characterized the properties of the NGS. In order to decouple NGS shape from the fluorophore spatial distribution, we used non-labeled MCTS immersed in a fluorescein solution. The latter is a fluorophore that can be used for two-photon excitation with peak emission around 520 nm, and is; thus, suitable for NGS generation. Fluorescein quickly permeates MCTS, making it possible to generate an NGS within. The NGS was observed at different depths (Figure 6). Table 4 presents the observed size and peak intensity of the NGS. The incapacity of our system to move the guide star in the z direction prevented us from assessing the axial FWHM. The observed quality of the guide star decreases with depth, with fast deterioration occurring typically around the 70 μm mark. Note that this decrease in observed quality is due to aberration and scattering in both the illumination and detection paths.

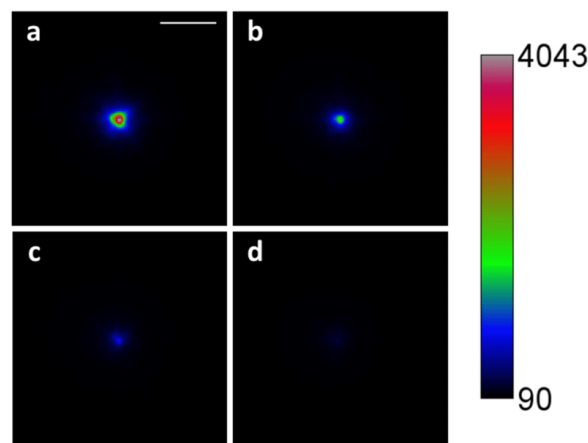


Figure 6. Widefield image of the guide star at different depths inside a multi-cellular tumor spheroid (MCTS). The MCTS was immersed in a fluorescein solution and the guide star imaged after 1 h. (a) Guide star outside spheroid. (b) Depth: 25 μm . (c) Depth: 50 μm . (d) Depth: 75 μm . Scale bar: 10 μm .

Table 4. FWHM of the non-linear guide star at different depths inside the MCTS.

Depth (μm)	FWHM _x (μm)	FWHM _y (μm)
0	2.23	2.18
25	2.44	2.14
50	2.38	2.27
75	4.74	4.89
100	8.65	7.90

MCTS were mounted inside agarose cylinders and observed before and after AOs correction (Figure 7). Corrections were performed at different depths, and MCTS were imaged each time up to a depth of 120 μm . In order to evaluate image quality at different depths, the 3D image was divided

into three Z sections ($Z_{1-40\mu\text{m}}$, $Z_{41-80\mu\text{m}}$, $Z_{81-120\mu\text{m}}$), after which a maximum intensity projection was performed in each one. Typically, a maximum of five to ten closed loop iterations could be performed due to the fast bleaching of the fluorophore and the long exposure times required for wavefront measurement (usually 0.3 to 1 s).

The AOs-corrected images show improvements in contrast and resolution when compared to uncorrected ones. Subcellular sized structures that were not well resolved in the “AOs off” position could be resolved after correction (Figure 7a–c).

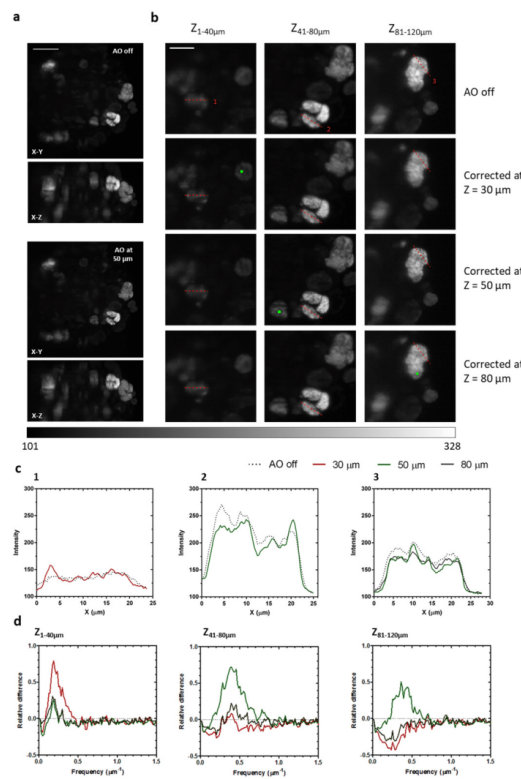


Figure 7. Image quality improvement in depth. (a) Maximum intensity projection of MCTS expressing the fluorescent protein H2B-ArrestRed, before AOs correction and after correction at 50 μm . Scale bar: 50 μm . (b) Maximum intensity projections of three regions of interest before AOs correction and after correction at 30, 50, and 80 μm . NGS were placed at the green dot in the respective corrections. All images were acquired using the same excitation intensity and 100 ms exposure. Corrections were performed using 1 s exposures. Scale bar: 25 μm . (c) Intensity profiles along paths 1, 2, and 3. (d) Relative differences of spatial frequencies between each of the corrections and the uncorrected case for each region of interest.

Spatial frequencies were evaluated by means of integrating the radial frequencies along concentric rings centered at the zero frequency (Figure 7d). Compared to the uncorrected case, there is a substantial increase (up to 79%) of frequencies in the range 0.1 to 0.8 μm^{-1} , corresponding to features of cellular and subcellular size (1.25 to 10 μm). Frequencies outside this range showed a slight decrease. At the $Z_{1-40\mu\text{m}}$ section, the most efficient correction was realized at 30 μm , while at the $Z_{41-80\mu\text{m}}$ section the most efficient was realized at 50 μm . At $Z_{81-120\mu\text{m}}$ imaging depth, correction becomes unreliable and

those performed at 30 and 80 μm showed a general worsening of image quality, although the one performed at 50 μm showed a slight improvement. Peak improvement in image quality, then, is greater for corrections realized at lower depths.

4. Discussion and Conclusions

Biological tissue can be difficult to image in depth due to absorption, scattering, and aberrations originating from both the sample and the optical system. SPIM is a popular in-depth imaging tool that has been coupled with adaptive optics to improve imaging by correcting system and sample-induced aberrations, most common in transparent tissue. However, scattering poses a challenge for AOs correction, compounded by the difficulty of adequate guide star generation within optically-thick samples.

We opted for a non-linear guide star approach, using fluorescent labeled proteins to create a point-like source of light through two-photon excitation. This approach is compatible with live samples and requires little sample preparation. However, the low intensity of the non-linear guide star requires the use of custom-built sensors. We; thus, developed and described an EMCCD-based SHWS to correct transparent inert samples using only 12,000 photons. Nonetheless, in order to measure the wavefront from inside non-transparent live samples such as MCTS, second-long exposure times are often required. When coupled with fast bleaching; however, this severely limits the number of correction steps possible (although four usually suffice). It is our belief that limiting the correction to the main modes of aberration induced by the sample could lessen the number of iterations required and increase correction reliability, while still providing significant image quality improvement.

We have shown improvements in image quality of optically-thick fixed samples, as per resolution and high-frequency detail. Corrections are especially effective in shallow depths (less than 50 μm), although image quality can be improved as deep as 120 μm . This represents an improvement over previously reported AOs implementations in light-sheet systems when imaging scattering samples. Indeed, correction depth is mainly limited by scattering: Signal-to-noise ratio becomes increasingly worse with depth due to the loss of ballistic light and the increment of noise due to scattered light, hindering centroid calculation of the Shack–Hartmann spots, and causing loss of wavefront measurement accuracy. Therefore, the use of longer wavelength NGS, less sensitive to scattering, could increase useful correction depth. Since aberrations are spatially dependent, a single correction usually does not improve the whole image. A scanning algorithm has been proposed in order to perform an averaged correction and reduce scattering artifacts when measuring the wavefront [7]. While it could be implemented in our system (we expect it to have a limited effect in our case), it does; however, slightly increase system complexity. Another possible improvement could be implementing a tiling algorithm in order to correct different regions of interest that could then be processed to obtain a single reliably-corrected image. This tiling approach; however, would require increasing correction time by at least one order of magnitude, thereby limiting temporal resolution. In SPIM, scattered illumination light gives way to a decrease in the penetration depth of the light-sheet, and results in ghost image artifacts. Scanned Bessel beams have shown increased penetration depth [17] and reduction of ghost artifacts thanks to the self-healing nature of the beam [18]. The use of an alternative illumination strategy, such as a scanned Bessel beam, could further improve detection of features deep into the sample [6].

In conclusion, w_{AO} SPIM is a powerful tool for in-depth imaging in thick non-transparent TMs, and we are confident that future development will resolve remaining shortcomings.

Author Contributions: J.M.B. and C.L. conceived of and designed the experiments. J.M.B. performed the experiments. X.L., G.D. and G.C. designed and developed the SHWS. J.M.B. and C.L. maintained the cell lines and produced the different MCTS. J.M.B. analyzed the data. J.M.B. and C.L. wrote the manuscript with support from all authors. C.L. supervised the project.

Funding: This research was funded by the CNRS, l'Université Paul Sabatier, la Région Midi-Pyrénées (PhD funded by a COMUE—Région Midi-Pyrénées grant APR 2016 OPTO-MECA-SPIM, ref 6823), l'Agence Nationale de la Recherche (ANR12-BSV5-0008-01, ANR-18-CE06-0027-03).

Acknowledgments: We gratefully acknowledge the scientific and technical support of our team members. We also thank Fabrice Harms and Cynthia Veilly for their helpful comments on the manuscript. We wish to thank G. Taillefer for manuscript proofreading and suggestions.

Conflicts of Interest: The authors declare no conflicts of interest.

References

1. Andilla, J.; Jorand, R.; Olarte, O.E.; Dufour, A.C.; Cazales, M.; Montagner, Y.L.; Ceolato, R.; Riviere, N.; Olivo-Marin, J.C.; Loza-Alvarez, P.; et al. Imaging tissue-mimic with light sheet microscopy: A comparative guideline. *Sci. Rep.* **2017**, *7*, 44939. [[CrossRef](#)] [[PubMed](#)]
2. Schwertner, M.; Booth, M.J.; Neil, M.A.; Wilson, T. Measurement of specimen-induced aberrations of biological samples using phase stepping interferometry. *J. Microsc.* **2004**, *213*, 11–19. [[CrossRef](#)] [[PubMed](#)]
3. Jorand, R.; Le Corre, G.; Andilla, J.; Maandhui, A.; Frongia, C.; Lobjois, V.; Ducommun, B.; Lorenzo, C. Deep and clear optical imaging of thick inhomogeneous samples. *PLoS ONE* **2012**, *7*, e35795. [[CrossRef](#)] [[PubMed](#)]
4. Tao, X.; Fernandez, B.; Azucena, O.; Fu, M.; Garcia, D.; Zuo, Y.; Chen, D.C.; Kubby, J. Adaptive optics confocal microscopy using direct wavefront sensing. *Opt. Lett.* **2011**, *36*, 1062–1064. [[CrossRef](#)] [[PubMed](#)]
5. Aviles-Espinosa, R.; Andilla, J.; Porcar-Guezenc, R.; Olarte, O.E.; Nieto, M.; Levecq, X.; Artigas, D.; Loza-Alvarez, P. Measurement and correction of in vivo sample aberrations employing a nonlinear guide-star in two-photon excited fluorescence microscopy. *Biomed. Opt. Express* **2011**, *2*, 3135–3149. [[CrossRef](#)] [[PubMed](#)]
6. Thomas, B.; Wolstenholme, A.; Chaudhari, S.N.; Kipreos, E.T.; Kner, P. Enhanced resolution through thick tissue with structured illumination and adaptive optics. *J. Biomed. Opt.* **2015**, *20*, 26006. [[CrossRef](#)] [[PubMed](#)]
7. Liu, T.L.; Upadhyayula, S.; Milkie, D.E.; Singh, V.; Wang, K.; Swinburne, I.A.; Mosaliganti, K.R.; Collins, Z.M.; Hiscock, T.W.; Shea, J.; et al. Observing the cell in its native state: Imaging subcellular dynamics in multicellular organisms. *Science* **2018**, *360*, eaaq1392. [[CrossRef](#)] [[PubMed](#)]
8. Debarre, D.; Booth, M.J.; Wilson, T. Image based adaptive optics through optimisation of low spatial frequencies. *Opt. Express* **2007**, *15*, 8176–8190. [[CrossRef](#)] [[PubMed](#)]
9. Jesacher, A.; Thayil, A.; Grieve, K.; Debarre, D.; Watanabe, T.; Wilson, T.; Srinivas, S.; Booth, M. Adaptive harmonic generation microscopy of mammalian embryos. *Opt. Lett.* **2009**, *34*, 3154–3156. [[CrossRef](#)] [[PubMed](#)]
10. Masson, A.; Escande, P.; Frongia, C.; Clouvel, G.; Ducommun, B.; Lorenzo, C. High-resolution in-depth imaging of optically cleared thick samples using an adaptive SPIM. *Sci. Rep.* **2015**, *5*, 16898. [[CrossRef](#)] [[PubMed](#)]
11. Sutherland, R.M. Cell and environment interactions in tumor microregions: The multicell spheroid model. *Science* **1988**, *240*, 177–184. [[CrossRef](#)] [[PubMed](#)]
12. Lorenzo, C.; Frongia, C.; Jorand, R.; Fehrenbach, J.; Weiss, P.; Maandhui, A.; Gay, G.; Ducommun, B.; Lobjois, V. Live cell division dynamics monitoring in 3D large spheroid tumor models using light sheet microscopy. *Cell Div.* **2011**, *6*, 22. [[CrossRef](#)] [[PubMed](#)]
13. Azucena, O.; Crest, J.; Kotadia, S.; Sullivan, W.; Tao, X.; Reinig, M.; Gavel, D.; Olivier, S.; Kubby, J. Adaptive optics wide-field microscopy using direct wavefront sensing. *Opt. Lett.* **2011**, *36*, 825–827. [[CrossRef](#)] [[PubMed](#)]
14. Wang, K.; Milkie, D.E.; Saxena, A.; Engerer, P.; Misgeld, T.; Bronner, M.E.; Mumm, J.; Betzig, E. Rapid adaptive optical recovery of optimal resolution over large volumes. *Nat. Methods* **2014**, *11*, 625–628. [[CrossRef](#)] [[PubMed](#)]
15. Wang, K.; Sun, W.; Richie, C.T.; Harvey, B.K.; Betzig, E.; Ji, N. Direct wavefront sensing for high-resolution in vivo imaging in scattering tissue. *Nat. Commun.* **2015**, *6*, 7276. [[CrossRef](#)] [[PubMed](#)]
16. Iyer, R.R.; Liu, Y.Z.; Boppart, S.A. Automated sensorless single-shot closed-loop adaptive optics microscopy with feedback from computational adaptive optics. *Opt. Express* **2019**, *27*, 12998–13014. [[CrossRef](#)] [[PubMed](#)]

17. Fahrbach, F.O.; Gurchenkov, V.; Alessandri, K.; Nassoy, P.; Rohrbach, A. Light-sheet microscopy in thick media using scanned Bessel beams and two-photon fluorescence excitation. *Opt. Express* **2013**, *21*, 13824–13839. [[CrossRef](#)] [[PubMed](#)]
18. Fahrbach, F.O.; Simon, P.; Rohrbach, A. Microscopy with self-reconstructing beams. *Nat. Photonics* **2010**, *4*, 780–785. [[CrossRef](#)]



© 2019 by the authors. Licensee MDPI, Basel, Switzerland. This article is an open access article distributed under the terms and conditions of the Creative Commons Attribution (CC BY) license (<http://creativecommons.org/licenses/by/4.0/>).